

POLITECNICO DI TORINO

Corso di Laurea Magistrale in

Ingegneria Meccanica

Tesi di Laurea Magistrale

EXPERIMENTAL CHARACTERISATION OF AN
ELASTOHYDRODYNAMIC CONTACT AND OF A THIN
HARD COATING BY MEANS OF A PIN-ON-DISK
TRIBOMETER



Relatori:

Prof. Luigi Mazza

Ing. Andrea Mura

Candidato:

Edoardo Goti

Anno Accademico 2018/2019

*“ The method of science is rational, and the best we have.
Therefore, it is rational to accept its results.
But not in the sense of trusting them blindly,
we never know beforehand where else we might be left in the lurch. ”*

*“ If we are uncritical we shall always find what we want:
we shall look for, and find, confirmations, and we shall look away from,
and not see, whatever might be dangerous to our pet theories. ”*

Karl Popper

TABLE OF CONTENTS

Table of Contents.....	4
1 Forewords	6
2 Introduction.....	7
3 Equipment and methods for the experimental investigation.....	10
3.1 Tribometers	10
3.2 Profilometers	12
3.3 Calotester	13
3.4 Microscopes	14
3.5 Microhardness tester	14
4 The EHL contact theory.....	17
4.1 Lubricants classification	17
4.2 Properties and rheology of lubricants	18
4.2.1 Viscosity.....	18
4.2.2 Temperature and pressure dependence.....	20
4.2.3 Rheology models	23
4.3 The EHL classical theory for for Point Contact	27
4.4 Lubrication regimes	37
4.4.1 Boundary lubrication	37
4.4.2 Fluid film lubrication	38
4.4.3 Mixed lubrication	39
4.4.4 Limits of Lambda factor.....	40
4.5 Traction in EHL contacts	41
5 Setup and materials.....	45
6 Experimental results.....	49
6.1 Preliminary results	49
6.2 Results of the investigation	50
7 Discussion of the results	59
7.1 Statistical analysis of the results	59
7.2 EHL contact condition analysis.....	59
8 Tribology of thin hard coatings	64
8.1 Overview of the mechanisms of dry friction and wear	64
8.1.1 Friction	64
8.1.2 Wear.....	67
8.2 Classification and properties of Hard Coatings	71
8.3 Deposition methods	72
8.3.1 Physical Vapor Deposition	73

8.3.2	Chemical Vapor deposition	74
8.3.3	Ion implantation	75
8.4	Tribology of thin films.....	75
8.4.1	Macroscopic behaviour	75
8.4.2	Microscopic behaviour	77
9	Setup and Materials	80
10	Experimental results	83
10.1	Preliminary tests	83
10.2	Repetitions with optimum parameters.....	88
11	Discussion of the results.....	95
11.1	Conventional identification method of friction curves.....	97
11.2	Some remarks to the method	101
11.3	Analysis of the tribological results.....	102
11.3.1	Friction results.....	102
11.3.2	Wear.....	105
12	Conclusion.....	110
Appendix.....		112
A.1	EHL – Test in high humidity conditions.....	112
A.1	TiN – Table of Filter curves	114
13	Bibliography.....	119

1 FOREWORDS

This thesis project is the outcome of an extended experimental investigation on tribology within the framework of an 8 months joint research project between Politecnico di Torino (Italy) and Anton Paar TriTec SA (Peseux, Switzerland).

As part of the ongoing effort to remain leader in tribological test instrumentation, Anton Paar participates in and contributes to several international standards committees and it is part of the American Society for Testing Materials (ASTM) and International Standards Organisation (ISO). The present cooperation with Politecnico di Torino arises from the will to start a revision process of the ASTM G99 standard.

The aim of the present joint research project was to extend the scope of the ASTM G99 standard by developing:

- a reference procedure for the diagnostics of pin-on-disk tribometers;
- a new procedure for the tribological characterisation of hard coatings.

These two separate topics within the subject of tribology will be dealt with in two distinct sections of this paper.

In Part I the experimental results from several tests carried out with a special elastohydrodynamic lubricated contact are presented and discussed. The attention is more focused on the tribometer and the pin-on-disk method itself, rather than on the significance of the specific tribological application. This condition is successfully exploited to formulate a reference procedure for diagnostics, by reproducing a repeatable no-wear condition with a very stable coefficient of friction.

Part II focuses, on the contrary, on a specific tribological application as an end, providing the tribological characterization of a TiN PVD coating. The results obtained with various configurations, material pairs and parameters are presented as an evidence that it is possible to obtain stable and sufficiently repeatable friction curves under specific testing conditions. A standard procedure to extrapolate a potential characteristic value of the coefficient of friction is then put forward on the basis of the geometrical analysis of friction curves.

2 INTRODUCTION

It is commonly known that the coefficient of friction (herein referred to as CoF) is far from being a characteristic property of the materials involved in the contact [1] since it also depends on many other parameters: speed, load, temperature, humidity, wear, size/scale...to name a few [2]. This is the reason why in the field of tribology results are usually scattered and it is not at all obvious to find consistent results under the same testing conditions. Too many papers in the scientific literature claim make this on the basis of mean values and tolerance ranges of the CoF, without however disclosing actual friction curves.

In other words, tribological tests cannot take into account in any circumstance all the parameters and phenomena involved in a real application. It is clear, then, why the DIN 50322 standard puts forward a classification of the methods in tribology according to which pin-on-disk tests fall into the category of model test. In this pecking order, “model tests” (i.e. simplified laboratory tests) are the polar opposite of “field tests” (i.e. actual systems tested in actual operating conditions) and it is accepted that friction and wear results may be rather different from one another. Going from model tests to field tests, indeed, tests grow in representativity including many more variables, but lose in generality which is the main asset of “model tests” [3]. By echoing what the ASTM G99 standard states:

“Since the pin-on-disk test method does not attempt to duplicate all the conditions that may be experienced in service (for example; lubrication, load, pressure, contact geometry, removal of wear debris, presence of corrosive environment), there is no insurance that the test will predict the wear rate of a given material under conditions differing from those in the test.”

ASTM G99-17, ASTM International, West Conshohocken, PA

“In my opinion, the sphere-on-plane contact geometry is useful primarily as a research tool... It would be dangerous, however, to predict load capacities and wear lives in other contact geometries from the results in a sphere-on-plane apparatus. In the final analysis, the real utility of a lubricant must still be established in the actual application.”

H. Sliney

Comment cited in: P. J. Blau., *The use and misuse of the pin-on-disk wear test*, STLE Annual Meeting, May 21, 2014

What is more, the test rig itself, where needed, is likewise expected to affect the estimation of the tribological quantities, as a result of its mechanical layout, its own dynamic characteristic and the specific experimental setup. This issue is reiterated by Holmberg et al. [4] who state:

“A measured friction coefficient is the result of both physical and chemical interaction in a discrete system, which is quite difficult to repeat from one laboratory to another because of the large number of influencing parameters. In the case of pin-on-disc testing it has been observed that even the vibrational characteristics of the test machine can have a marked influence on friction and wear behaviour.”

K. Holmberg, A. Matthew

Coating tribology, Elsevier, Amsterdam, 1994

Therefore, no experimental value for a given material pair should be ever stated as “correct” or “representative” in absolute terms. In such a scenario, it is hard to be confident of the estimate of the coefficient of friction and even to understand whether its fluctuations are attributable to the inevitable whims of the physics at the interface or veritable erroneous measurements.

This issue represents the starting point of the first part of the present thesis project: a reference conditions procedure is needed to check, at least, that tribometers are giving the correct friction coefficient.

Should one be able to find out a combination of testing set-up, materials and testing parameters that is proven to produce friction results which are:

- systematic;
- repeatable in the same testing conditions;
- stable over time;
- consistent across different tribo-testing machines of the same kind;

such a condition may be considered a reference, or at least a *relative reference*. By extension, a criterium to assess if a particular tribometer is potentially affected by technical problems can be derived if its results are different from those expected.

The actual release of the G99 standard already includes widely verified experimental results. It provides indeed the outcome of an Interlaboratory Study (ILS) in which 3 bulk material pairs were tested with several repetitions by 20 different laboratories around the world and under the same. However, data from the original ILS are not appropriate to give rise to a reliable reference value. They are potentially affected by too many variables, first and foremost wear and humidity, and suffer excessive uncertainty. Wear is an erratic phenomenon leading to hardly repeatable degradation of the tribological interface. The best trade-off to achieve the challenging goal that has been set is thus eliminating wear.

The aim is therefore to develop two reference testing procedures for pin-on-disk tribometers in which the coefficient of friction is stable, repeatable and solely determined by tribo-testing parameters set out by users. One procedure is intended for one-way rotating tests and the other for linear reciprocating tests.

In order to achieve this challenging result, the peculiar friction performances of the elastohydrodynamic lubricated contact condition (herein referred to as EHD or EHL) were exploited. A multitude of papers have been released so far in which the coefficient of friction was investigated, mainly to plot a Stribeck curve. For example, friction values were reported in the works of Zhang et al. [38], [39] and Fu et al. [40] which investigated similar conditions in the regime of full-film lubrication. Also, Nishikawa et al. [41] investigated the CoF in reciprocating and unidirectional ball-on-flat test. These researchers all however always used a dedicated test-rig to measure the elastohydrodynamic film thickness. The author did find any which used a standard pin-on-disc tribometer to measure the CoF in the wear-free fully-flooded EHL regime with a liquid lubricant.

In the next sections the reliability of the chosen test setup to verify the good performance of tribometers is wisely demonstrated. The methodology outlined is then recommended as a monitoring tool for the “follow-up” of test rigs; in other words, as a check-up to make an assessment on either software / hardware issues or issues in terms of calibration.

For the purpose of robust reliable statistics, results from several pin-on-disk tribometers located in different laboratories around the world and in different environmental conditions were compared. The same testing methodology was tried out in two separate operating conditions (in terms of friction force and load) such that the assessment on the performance of the machines could encompass a larger share of their working range.

The author wishes to underline that no in-depth examination of the contact mechanics or numerical simulations are provided here as it goes beyond the scope of this paper. Yet, suitable applications of the available theory are provided in the next sections. This is to analyse and better understand some anomalous phenomena and to avoid a “overly empirical” approach as suggested by Stachowiak and Batchelor [5].

This study is intended as the first step of a more comprehensive investigation which would potentially include many more pin-on-disk tribometers of a number of manufacturers. If further observations disclose the same stable and repeatable behaviour, the outlined procedures will be proposed to become part of the ASTM G99 and G133 international tribological standard.

ASTM G99 is the most commonly used general standard for pin-on-disk tribometers. It is more a “procedural guideline” than a standard test method [6] as it provides a very general approach by designating the correct “modus operandi” to carry out tests and calculations [7]. In addition, it currently focuses on wear testing of bulk materials only.

Many modern industrial users of this tribological technique are evaluating, though, the behaviour of thin hard coatings, being therefore interested in both wear and friction characterisation with lower loads and faster speeds than for bulk materials. However, too few standards for tribological testing of the coatings are available at present and it contributes to make the study of this subject, as underlined by Holmberg.

“Although enormous amounts of tribological coating evaluation and testing work is carried out, it often contributes very little to our general understanding, due to the lack of standardization. It is seldom possible for one worker to take full advantage of tests carried out and published by others as reference data, because there will usually be some differences in the sliding conditions, such as speed, load, specimen geometry or surface roughness. There are strong scientific and economic arguments for further standardization of the characterization of coatings, measurements of coating properties and tribological test methods and devices.”

K. Holmberg, A. Matthew

Coating tribology, Elsevier, Amsterdam, 1994

As the state-of-the-art stands at present, ISO 18535:2016 is the sole standard dealing with friction and wear characterisation of thin ceramic coatings. It was introduced for diamond-like carbon films (DLC) but at present it extends to any kind of hard coating of the same family [8]. Its main limitation is that it focuses on the superficial layer only. The guidelines of the standard forbid that the sphere reaches through the film touching the substrate: that occurrence invalidates the measurements unless tests are immediately stopped. Practice suggests that this requirement is difficult to please if materials softer than DLC are tested.

As a matter of fact, the presence of a coating is influential in terms of friction and wear even if the substrate is not secured by a continuous protective film. Whether its influence is beneficial or detrimental depends on the nature of both the protective layer and the underneath supporting material. In practice, this standard successfully characterises superficial films but fails when the characterisation of the tribological system as a whole is required.

Such a scenario represents the starting point of the second part of the present research project. The purpose was to assess whether it is feasible to get stable and sufficiently repeatable friction curves thanks to which extrapolate a standard method to characteristic coatings.

A basically empirical approach was followed, but suitable applications of the available theory and comparisons to other authors’ works will be still proposed in the next sections. This is to analyse and better understand phenomena and to avoid a “too empirical” approach as suggested by Stachowiak [5]

“The art of tribological experimentation is to devise an experiment which is not too empirical so that its data is compromised by non-causal factors such as e.g. weather fluctuations, but at the same time maintains relevance to real problems.”

G.W. Stachowiak, A.W. Batchelor,

Experimental Methods in Tribology, Elsevier, Amsterdam, 2004

3 EQUIPMENT AND METHODS FOR THE EXPERIMENTAL INVESTIGATION

This research project was made possible thanks to the collaboration of the Department for Mechanical and Aerospace Engineering Laboratory at Politecnico di Torino and the Anton Paar TriTec Internal Application Laboratory. Facilities and equipment of both laboratories were used to carry out the experimental campaign.

The same equipment basically served for both investigation topics which this paper deals with. Therefore, the choice has been made to describe the equipment at once before going into details about theory and experimental results of each topic.

3.1 TRIBOMETERS

A total of three different Anton Paar pin-on-disk tribometers were used: two tribometers model TRB and one model TRB³ of next generation. The three machines are displayed in Figure 3.1.

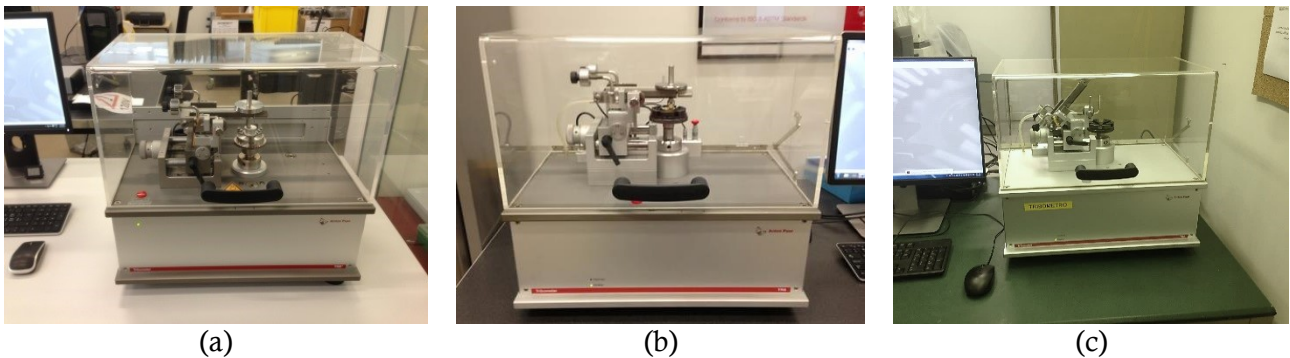


Figure 3.1 The three tribometers used in this study: a) TRB³ at Anton Paar TriTec, laboratory; b) TRB at Anton Paar TriTec, laboratory; c) TRB at Politecnico di Torino laboratory

In pin-on-disk tribometers the friction coefficient is calculated following the classical Amotons' definition, where it is implicit that μ is the dynamic friction coefficient.

$$\mu = \frac{F_T}{F_N} \quad (1)$$

in which the measured quantity is the tangential friction force F_T acting at the contact area and N is the known normal force. In this kind of tribometers the load (F_N) is applied using dead-weights placed on the measuring arm.

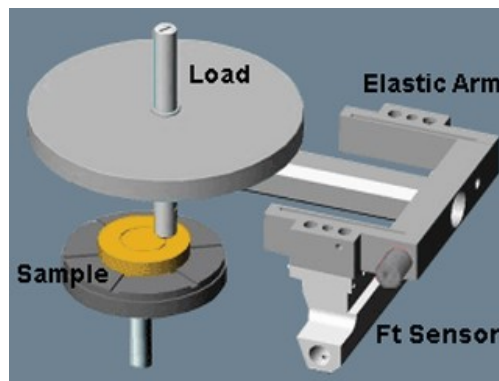


Figure 3.2. Schematic of a pin-on-disk tribometer

The tribometer User Manual states that the position of the counterweights is appropriate if a little hit on the machine frame is enough to switch back the arm to the upright position. This method is usually acceptable in tribological testing. The effect of an actual load slightly different from the nominal one is normally of less importance compared to the own variability of the phenomenon at the contact region. This applies, for example, in all those situations in which either the local scattering of the coefficient of friction values or the variations of its mean value have the same order of magnitude of the mean value itself.

For the sake of this experimental investigation, and above all the study of a repeatable reference condition, the grade of accuracy was too poor. In the event of sensitive measurements, like the ones presented in the first part of this dissertation, even minimal variations of applied load make the curve drift upwards or downwards. After all, it is enough that the “checking hit” introduces a somewhat different quantity of energy into the system that an inconsistency arises.

A new refined procedure was then implemented. A precision weight of nominal mass equal to 2g (Figure 3.3a) made it possible to assess the proper balancing of the arm with augmented accuracy and repeatability. After placing the little weight on the arm at rest, the arm was gently moved to the horizontal position (Figure 3.3b) and, first, it was quickly verified that the arm stayed still (Figure 3.3c). The weight was immediately removed, and the judgment issued: if the arm went up on its own (Figure 3.3d) the position of the counterweights was eligible. If, in addition, such a position was the rightmost allowing the same reaction of the arm, it was eventually accepted.

Furthermore, some verifications with a compression load cell mounted on the mandrel (Figure 3.4a) proved that this innovative method lets the actual load on the sample be closer to the nominal value.

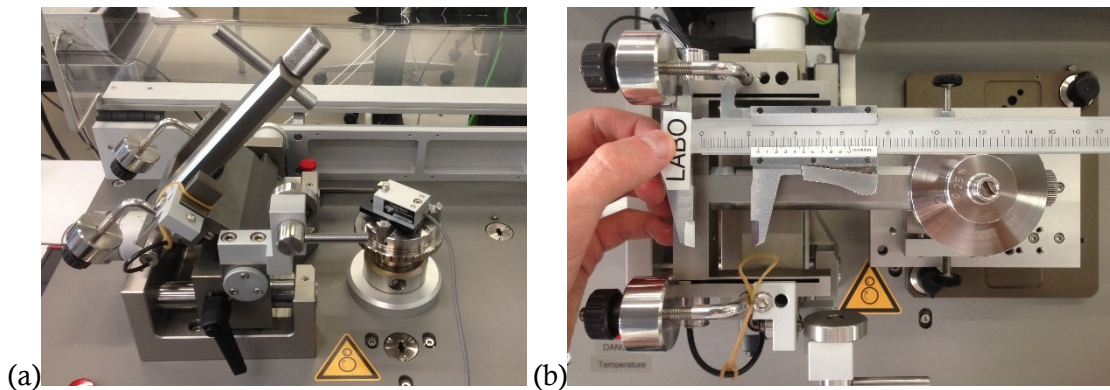


Figure 3.4 (a) Compression load cell mounted on the mandrel; (b) measurements of the counterweights position

The quantification of the counterweights position was performed with a standard analogic Vernier calliper (0,05mm of resolution), paying attention to reproduce the same position of the instruments as depicted in Figure 3.4b.

3.2 PROFILOMETERS

A Taylor-Hobson stylus profilometer (in compliance with ISO 4287:1998) standard was used to detect the profile of samples surfaces before and after wear tests.



Table 3.1 The Taylor-Hobson profilometer at Anton Paar TriTec laboratory

The dedicated TalyProfile Gold 7.2.7478 software allowed to prepare the profiles rough data before measuring the roughness of the samples. Surface waviness and possible tilt angle were eliminated as belonging to the macroscale in which they should not enter the roughness measurement. Moreover, an integrated analysis tool was exploited to automatically integrate the area of wear tracks.

3.3 CALOTESTER

An Anton Paar CAT²c was used to perform the measurement in order to have an experimental value of the coating layer thickness. Figure 3.5a and b show the actual machine and its operating principle respectively. Ball crater test is a semi-destructive test: a sphere is pressed against the surface of the sample and put into rotation by a drive shaft. The relative motion between the sphere and the sample produces abrasive wear, and the abrasive effect is maximized by adding a little quantity of micrometric diamond slurry between the sphere and the sample surface. The normal load at the contact is provided by the weight of the sphere itself.

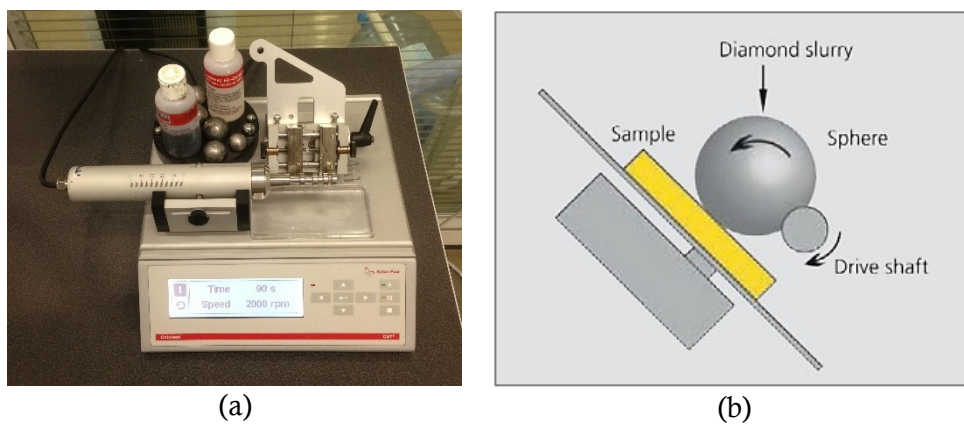


Figure 3.5. (a) CAT²c Calotester at Anton Paar TriTec laboratory; (b) Operating sketch of the ball crater method

The evaluation of the surface layer thickness is performed by means of an optical technique. The worn spherical cap is observed under the microscope to measure the diameters of “d” and “D” (see Figure 3.6). Since the radius of the spherical dome is known (it is approximatively the same as the sphere), you can calculate the coating thickness resorting to the following geometrical formula:

$$h = \frac{x \cdot y}{2R} = \frac{(D - d) \cdot d}{2R} \quad (2)$$

In the present study, the optical microscope described in the following subsection was used for the optical analysis. The measurement of the worn cap and the calculation of the thickness were performed through the dedicated Anton Paar Video software which include a specific analysis tool for the calculation of the coating thickness.

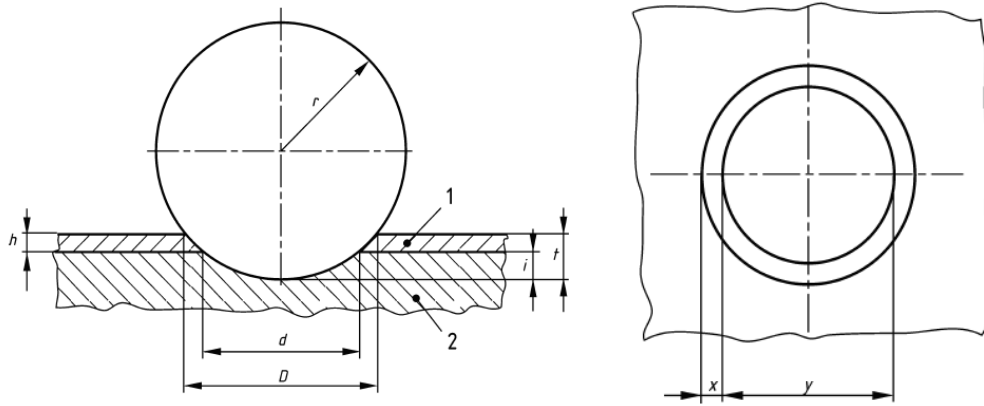


Figure 3.6 Calculation of the coating thickness in accordance to DIN EN 1071:2002.

3.4 MICROSCOPES

The analysis of surfaces before and after wear tests was performed resorting to optical microscopy. A GT Vision Ltd. microscope fitted with a Nikon digital camera was used.

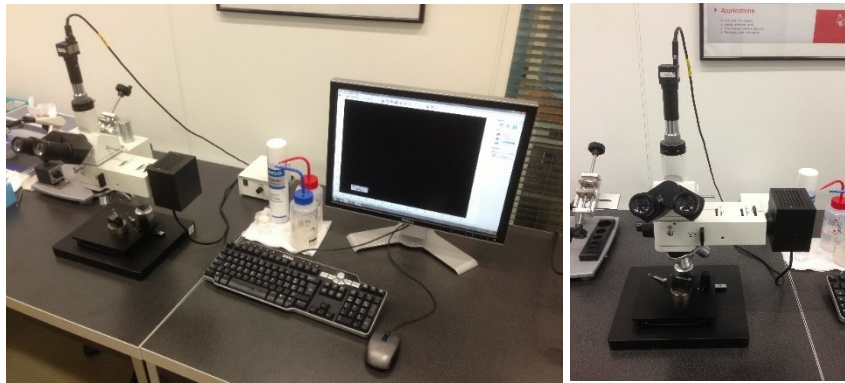


Table 3.2. Gt Vision Ltd. optical microscope at Anton Paar TriTec laboratory

3.5 MICROHARDNESS TESTER

An Innovatest[®] microhardness tester by Rupac s.r.l. was used to experimentally evaluate Vicker microhardness of sample surfaces. Figure 3.7a shows an overview of the testing machine and Figure 3.7b provides a detailed view on the indentation head with optical videomicroscope mounted on board.

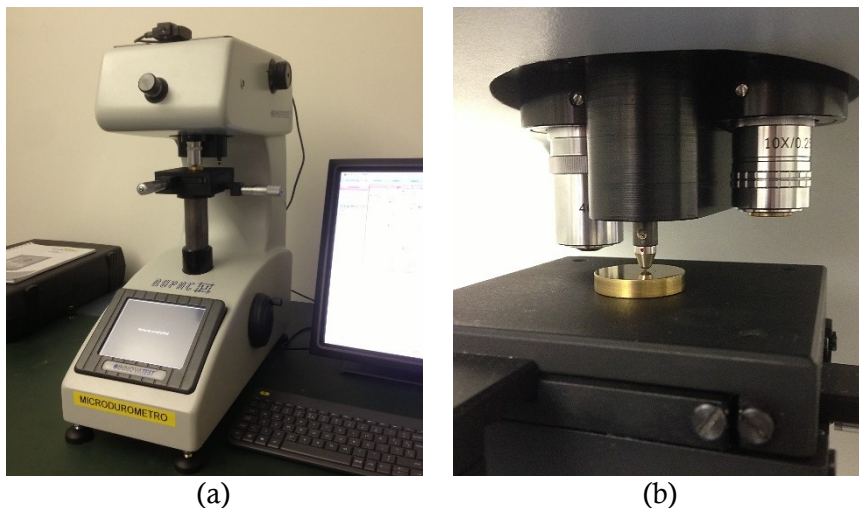


Figure 3.7. (a) Innovatest by Rupac S.r.l.; (b) detail of the indenter head.

The microhardness measurement consists in pressing a sharp pyramidal diamond indenter (a square pyramid in the case of Vicker hardness) against the surface of the sample until plastic deformation is produced and then releasing the contact. The surface hardness is evaluated with an optical method, by measuring the area of the footprint under the optical microscope.

PART I

4 THE EHL CONTACT THEORY

4.1 LUBRICANTS CLASSIFICATION

The primary function of whichever lubricant is to control and reduce friction and wear. This mission is fulfilled because the presence of a lubricant between two mating solid surfaces prevents solid-solid contact to take place. Friction phenomena typical of solid interfaces are replaced with the solely viscous friction of the liquid, that is usually much lower. Lubricants for engineering applications can be solid, gaseous or liquid and their action depends on the lubrication regime they establish.

Solid lubrication is resorted in engineering applications when liquid lubricants cannot be used due to high operating temperatures. Ultimate solid lubricants are lamellar solids like graphite or MoS₂, polymers like PTFE and soft metals like lead (Pb) and copper (Cu) showing little tribological compatibility with steel. The main disadvantages are related to the limited ability to conduct heat and the easiness of removal from surfaces. Liquid lubrication is far more expedient in solving the aforementioned problems. Different kind of liquid lubricants are available, among the others: mineral oils, synthetic lubricants, greases and emulsions are the most used ones at present.

Mineral oils are natural hydrocarbon compounds from petroleum and may be classified in four classes according to the chemical structure of their main base stock. An example of a typical compound belonging to each class is drafted in Figure 4.1.

- Paraffinic oils (Figure 4.1a: Paraffin)
- Naphthenic oils (Figure 4.1b: Naphthene)
- Olefinic oils (Figure 4.1c: Olefin)
- Aromatic oils (Figure 4.1d: Polycyclic hydrocarbon)

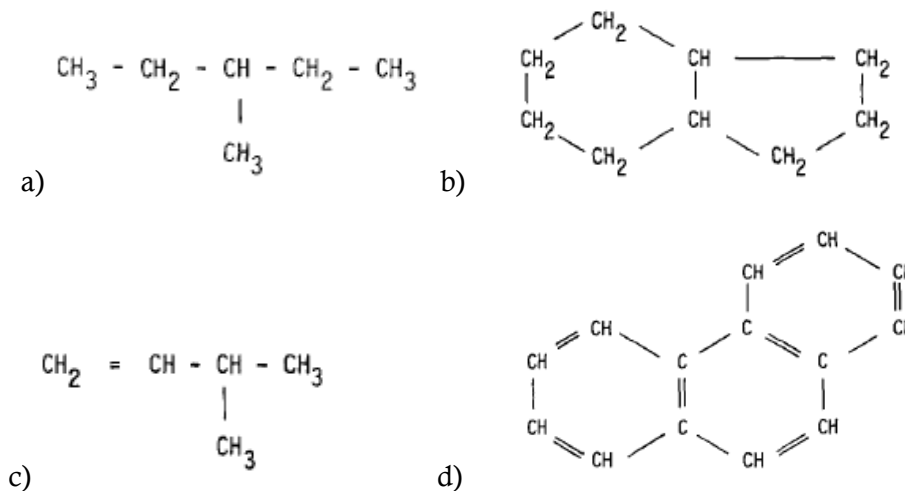


Figure 4.1 Different types of chemical structure for mineral base stocks

H. Czichos, "Tribology", Tribology Series Vol.1, Elsevier, 1978

As to *synthetic lubricants*, there is a variety of heterogeneous substances falling into this category which is highly specific for the diverse applications. An attempt to subdivide synthetic lubricants into comprehensive classes is made by Bushan [9]. According to his classification the following chemical classes are identified:

- Synthetic hydrocarbons (above all Polyalphaolefins)
- Esters
- Phosphate esters
- Silicate esters
- Silicones
- Silahydrocarbons

- Polyphenylether
- Perfluorinated fluids
- Chlorotrifluoroethylene polymers

The matter of synthetic lubricants is complex, so no further details will be given about their chemical characteristic as it is beyond the scope of this paper. The reader can refer to specialized textbooks as the ones by Pirro and Wessol [10] and Pawlak [11] for more information about the different kinds of liquid lubricants and their applications.

4.2 PROPERTIES AND RHEOLOGY OF LUBRICANTS

4.2.1 Viscosity

The most used lubricants in mechanical applications are liquid lubricants also known as “oils” which can be classified according to their provenance: “mineral oils” for those of petroleum origin, “fatty oils” for those of animal or vegetable origin and “synthetic oils”.

The main property of a lubricant is the viscosity. The absolute viscosity is defined by the following relationship found by Newton in 1687:

$$\eta = \rho \cdot \nu = \frac{\tau}{\dot{\gamma}} \quad (3)$$

Where:

- τ is the shear stress [N/m²];
- $\dot{\gamma} = (du/dz)$ is the shear strain rate (z is the direction perpendicular to motion) [s⁻¹];
- η is the absolute or dynamic viscosity [Pa·s];
- ρ is the specific gravity [kg/m³];
- ν is the kinematic viscosity [m²/s].

This equation has a general validity as it takes into account local properties and no further hypotheses are set out about how τ and η vary with respect to $\dot{\gamma}$ along space and time. By reversing this equation, the general local viscous force can be expressed as:

$$F_v = \eta \cdot A \cdot \frac{du}{dz} \quad (4)$$

Newton did not just introduce Equation (3) but he came up with the so-called Newton’s Postulate [12] which sets the basis of what we know today as the “Newtonian behaviour” of fluids. The Newton’s postulate can be easily displayed by reference to a Couette flow, as sketched in Figure 4.2. The bottommost layer, clung to the static surface, will not move at all whereas the uppermost layer will move along with the upper plane; each layer in between will move with a velocity directly proportional to the distance between the two planes.

$$s = \text{shear strain rate} = \frac{u}{h} = \frac{u_1}{h_1} = \frac{u_2}{h_2} = \dots$$

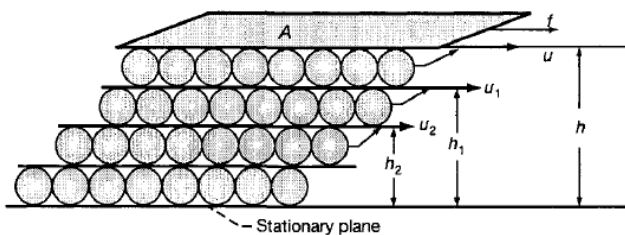


Figure 4.2: Physical illustration of the Newton's Postulate

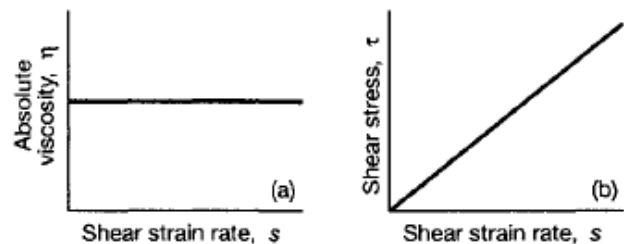


Figure 4.3. Typical rheology of a Newtonian fluid

B.J.Hamrock, S.R.Schmid, B.O.Jacobson, *Fundamental of Fluid Film Lubrication*, II Ed., Marcel Dekker, 2004

If the lubricant behaves in a Newtonian fashion shear stress increases linearly with shear rate and hence the model is called a *linear model*. The absolute viscosity is a constant (it does not change as $\dot{\gamma}$ changes) and the incremental ratio du/dz equals the global ratio u/h . In this condition, equation (3) changes as follows:

$$\eta = \frac{\tau}{\dot{\gamma}} = \text{const} \quad ; \quad \forall \dot{\gamma} \quad (5)$$

Basically, for no kind of fluid, wherever the value of shear rate is minimum, the Newtonian approximation is satisfactory and only one value of viscosity is enough. A few real fluids, however, disclose a behaviour that is linear up to high strain rates; mention is made to water, blood plasma, benzene and light oils which have a loose molecular structure. In case of mineral oils and greases, the molecular structure is complex, and molecules are prone to give rise to bonds interfering with the shear action. The behaviour becomes non-Newtonian as soon as shear rate reaches above $10^5 \div 10^6$ [s⁻¹] and the proportionality between shear stress and shear strain rate is lost.

Many different Non-Newtonian behaviours are there. Depending on how viscosity (or shear stress) changes with shear strain rate, one may classify:

- *Pseudoplastic fluids*: shear thinning behaviour in which viscosity falls if shear rate rises (typical of multigrade oils);
- *Dilatant fluids*: shear thickening behaviour in which viscosity grows if shear rate rises (typical of suspension with high solid content).
- *Bingham fluids*: Newtonian or pseudoplastic behaviour but flow is possible only above a critical (yield) shear stress.

Recalling equation (3), it is possible to model these non-linear behaviours resorting to simple power laws, where index n is treated as a constant of the given fluid.

Non-Newtonian behaviour	Model	Equation	
Pseudoplastic fluids	Ostwald model	$\tau = \eta \cdot \dot{\gamma}^n$	$n < 1$
Dilatant fluids		$\tau = \eta \cdot \dot{\gamma}^n$	$n > 1$
Linear Bingham fluids	Bingham model	$\tau = \tau_s + \eta \cdot \dot{\gamma}$	
Pseudoplastic Bingham fluids	Herschel-Bulkley model	$\tau = \tau_s + \eta \cdot \dot{\gamma}^n$	$n < 1$

Another possible classification is based on how viscosity (or shear stress) changes in time under constant shear rate:

- *Thixotropic fluids*: apparent viscosity falls to the persistence of the shear action;
- *Rheopectic fluids*: apparent viscosity increases to the persistence of the shear action;
- *Viscoelastic fluids*: the original shape is restored as soon as the deforming force is released.

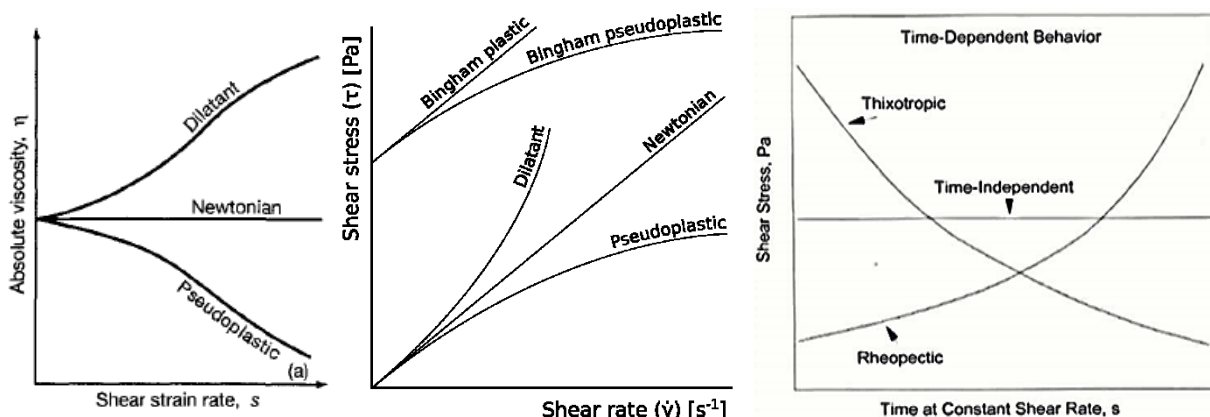


Figure 4.4. Non-Newtonian behaviours

Many complex models have been proposed to describe the behaviour of these fluids. You can refer to specialized textbooks and papers in the scientific literature.

The two types of non-Newtonian behaviour which are important from the engineering point of view are the *thixotropic* behaviour and, above all, the *pseudoplastic* behaviour. In this latter case, the shear rate increases more rapidly than the shear stress, as noticeable in Figure 4.4. Pseudoplastic, dilatant, rheopectic and viscoelastic behaviours are usually reversible unless other degradation processes do not come into play. Thixotropic behaviour may be irreversible in the sense that permanent viscosity loss is also possible if molecular structure degradation happens.

4.2.2 Temperature and pressure dependence

Viscosity is a parameter that is deeply influenced by operating temperature and pressure, but in two opposite ways. Viscosity falls if temperature increases and sometimes the decline is large under slight changes of the thermal level. This is usually the prevailing effect in hydrodynamic lubrication (of conformal contact). On the contrary, increasing pressure has a stiffening effect on the fluid and the viscosity grows dramatically. This is the case of the elastohydrodynamic lubrication (of non-conformal contact) where the maximum contact pressure may reach several GPa and the fluid behaves like a pasty solid as the increase in pressure clearly prevails on the increase of temperature.

Many equations to describe the temperature-viscosity and the pressure-viscosity dependence have been put forward by many authors. Some of them are empirical, i.e. derived from regression of experimental data, others come from theoretical models. However, all the equations describe a “way to behave” and are indeed provided with a number of constants whose values must be identified with an equal number of direct measurements. An overview on the most notorious relationships is displayed in Table 4.1 and Table 4.2.

Table 4.1. Viscosity-temperature formulas

Reynolds	$\eta = \eta_0 e^{-\beta(T-T_0)}$	Early equation; accurate only for a very limited temperature range.
Andrade-Eyring	$\eta = \eta_0 e^{\frac{a}{T}}$	Lesser used
Slotte	$\eta = \frac{s}{(a+T)^m}$	Reasonably precise; useful in numerical analysis
Walther	$(\nu + a) = b d^{1/T^c}$	Forms the basis of the ASTM viscosity-temperature chart (ASTM D341 standard); a = 0.6–0.75, b = 1, d = 10.
Vogel	$\eta = \eta_0 e^{b/(T+\theta)}$	Most accurate; very useful in engineering calculations
Roelands	$\log \eta + 1.2 = G_0 \times 10^{-S_0 \log(1+t_m/135)}$	Less used

Adapted from: G.W. Stachowiak, A.W. Batchelor, *Engineering tribology*, Butterworth-Heinemann, 2000

Where:

- T (or t_m) is the value of the operating absolute temperature [K];
- η_0 the viscosity under the reference temperature T_0 ;
- a, b, s, d, S_0, G_0 are characteristic constants of the given lubricant;
- m is a whole positive exponent equal or greater than 1;
- η is the value of the dynamic viscosity at temperature T (or t_m);
- ν is the value of the kinematic viscosity [mm^2/s] at temperature T (or t_m);

θ is the temperature of “infinite viscosity”, usually assumed equal to 368K.

Table 4.2 Pressure-viscosity equations

Barus	$\eta = \eta_0 e^{\alpha p}$	Very simple equation but good only at pressure below 0.5GPa and ambient pressure
Cameron	$\eta = \eta_0(1 + cp)^{16}$	Suitable for higher pressure than Barus equation
Chu et al.	$\eta_p = \eta_0(1 + C \times p)^n$	Evolution of the Cameron equation where n is a generalized characteristic lubricant exponent
Roelands	$\eta = \eta_0 \exp\left\{(\ln \eta_0 + 9.67)[-1 + (1 + p/p_0)^z]\right\}$	Fits experimental date much better than Barus equation

Where:

p is the operating pressure [Pa];

α is the pressure-viscosity coefficient [Pa^{-1}];

η_0 is the dynamic viscosity at ambient pressure;

η (or η_p) is the value of the dynamic viscosity at pressure p ;

c is an experimentally determined constant;

C is a temperature parameter (function ambient viscosity) obtained from diagram [13];

p_0 is a reference arbitrary pressure level, equal to $5.1 \cdot 10^{-9}$ Pa;

z is dimensionless constant equal to 0.68;

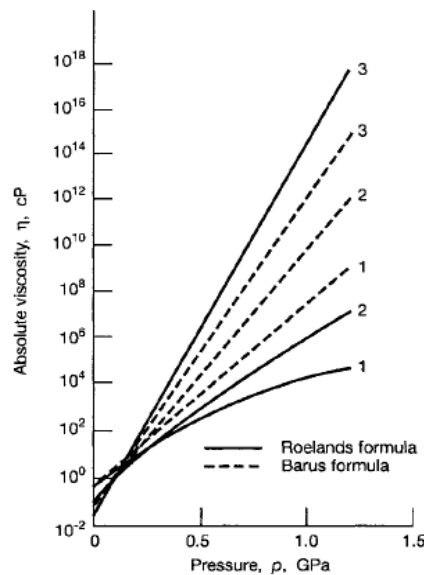


Figure 4.5 Comparison between Barus' and Roelands' equations at ambient temperature

B.J.Hamrock, S.R.Schmid, B.O.Jacobson, *Fundamental of Fluid Film Lubrication*, II Ed., Marcel Dekker, 2004

Pursuant its extreme simplicity, Barus equation is considered very expedient in computational methods for the EHL and extensively used since it is the earliest stage of this subject. Anyway, care must be taken because of pressure levels from 0.5 to 1.5 GPa (which are indeed common under a non-conformal lubricated contact) such a simple model fails and could lead to serious errors, as suggested by Figure 4.5.

The pressure-viscosity coefficient introduced by Barus is the slope of the plot of natural logarithm of dynamic viscosity against pressure. The higher α is, the larger the increase in viscosity with the same pressure rise is and, consequently, in an EHD contact the more the fluid is able to resist flowing out sideways. It describes thus the aptitude of a lubricant to form a continuous and thick lubricant layer able to separate solid surfaces and support the normal load at the contact. The pressure-viscosity coefficient is a function of the molecular structure of the lubricant and its physical characteristics such as molecular interlocking, molecular packing and rigidity. It follows that the viscosity may vary differently with pressure from lubricant to lubricant, even if the value of α is usually in the range $15 \div 35 \cdot 10^9 \text{ Pa}^{-1}$. The best way to evaluate the pressure-viscosity is by means of viscometric measurements but there are various empirical formulae to calculate this coefficient. Among these, it is worth to cite the one by Wooster:

$$\alpha = (0.6 + 0.965 \log_{10} \eta_0) \times 10^{-8} \quad (6)$$

Where: η_0 is the dynamic viscosity at ambient pressure in [cP], i.e. $10^{-3}[\text{Pa}\cdot\text{s}]$ ¹

All the equations presented hitherto have however no applicability in many practical problems since they take into account the influence of only one parameter at a time. In practice, viscosity changes in response to simultaneous modifications of the mechanical and thermodynamic quantities. To give just one example, the pressure-viscosity coefficient itself is strongly dependent on temperature and strain rate apart from pressure. One of the problems associated with the Wooster formula is that it predicts a value that is the same no matter what the condition at the contact interface is. Therefore, it allows accurate calculations only at low (at constant) temperature and shear rates.

Some attempts were made to focus on the influence of both pressure and temperature altogether. So and Klaus developed and improved the empirical expression for the pressure-viscosity coefficient of the Barus type applying a combination of linear and non-linear regression analyses with atmospheric viscosity, density and the viscosity temperature property.

$$\alpha = 1.216 + 4.143 \times (\log_{10} \nu_0)^{3.0627} + 2.848 \times 10^{-4} \times b^{5.1903} (\log_{10} \nu_0)^{1.5976} - 3.999 \times (\log_{10} \nu_0)^{3.0975} \rho^{0.1162} \quad (7)$$

Where: ρ is the atmospheric density at the temperature of interest in [g/cm^3];
 b is the so-called *ASTM slope* (non-dimensional) divided by 0.2;
 ν_0 is the kinematic viscosity at ambient temperature [cSt];
 α is the pressure-viscosity coefficient in $10^{-8}[\text{Pa}^{-1}]$.

As to the *ASTM slope*, ASTM D341 standard prescribes that the viscosity-temperature characteristic of each lubricant has to be provided as a line in a $\ln \ln(\nu + a) - \ln(T)$ diagram (see Figure 4.6). The ASTM refers to a modified *Walter formula* that allows plotting the curve in a double logarithmic coordinates and single logarithmic abscissa:

$$\ln \ln(\nu + a) = A - B \ln T \quad (8)$$

Where: A is a constant and represents the intersection with the coordinates axis;
B is the tangent of the viscosity angle, i.e. B is exactly the “ASTM slope”.

¹ A great deal of attention must be paid to units of measurement while using empirical equations: as such, they might work uniquely with units different from the SI.

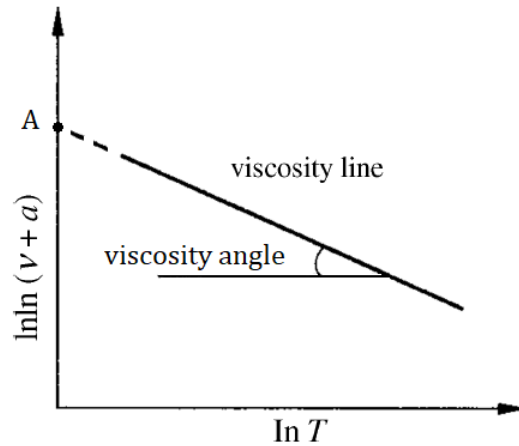


Figure 4.6. Viscosity-temperature characteristic by ASTM D341 (Walter formula)
 Modified from: S.Z. Wen, P. Huang, *Principles of Tribology*, John Wiley & Sons, 2012

When working conditions are such that considering the influences of both temperature and pressure on viscosity is imperative, more complex models are needed. Table 4.3 lists a few examples of viscosity-temperature–pressure equations.

Table 4.3 Viscosity-pressure-temperature equations

Barus and Reynolds	$\eta = \eta_0 \exp[\alpha p - \beta(T - T_0)]$	Simpler and easier in calculation but with a limited validity
Roelands	$\eta = \eta_0 \exp\left\{(\ln \eta_0 + 9.67) \left[(1 + 5.1 \times 10^{-9} p)^{0.68} \times \left(\frac{T - 138}{T_0 - 138} \right)^{-1.1} - 1 \right] \right\}$	More accurate; merger of his previously developed formulae

Roelands formula is one of the most accurate formulæ available and it is widely used at present in numerical analysis. This relationship states that, at a constant pressure, viscosity increases more or less exponentially with the reciprocal of absolute temperature. Similarly, at a constant temperature, viscosity increases more or less exponentially with pressure.

Roelands recognised that such an exponential model remains a rough approximation and may be resorted only in too moderate pressure-temperature ranges compared to the typical values of the applications. Anyway, his model was resumed and further developed by Houpert who introduced a mathematical form very similar to the Barus equation (and thus very suitable for computational applications) using a pressure-viscosity coefficient α^* of the “Roelands type” [13].

$$\eta_R = \eta_0 e^{\alpha^* p} \quad (9)$$

4.2.3 Rheology models

It is important to point out that an implicit hypothesis lays behind the formulas presented in Sec. 4.2.2: Newtonian behaviour is assumed. The missing parameter is still the shear rate as these formulas are found accurate merely at low shear rates.

Lubricants often present significantly non-Newtonian properties coming from their chemical nature and properties; and the influence of these properties is even stronger due to the severity of the EHL conditions. Elastohydrodynamically lubricated conjunctions experience rapid and extremely large pressure variations, a rapid transit time, possibly large temperature changes, high shear rates in case of heavily loaded lubricated sliding contacts. The correct evaluation of the lubricant film thickness would be possible provided that an accurate analytical model describing in an aggregated manner the pressure-

temperature-shear rate-viscosity dependence could be developed [13]. For example, a relationship $\alpha = \alpha(\dot{\gamma}, p, T)$ would allow to successfully apply a simple Barus-like equation in any condition. Unfortunately, neither physical models nor empirical equation of this kind have ever been put forward up to now. The only way is through an accurate viscometric characterisation at thermo-mechanical conditions similar to those of the specific application. A limited attempt was made by Johnston [14] which proposed an allowing of the calculation of the value of a α -coefficient from ambient pressure viscosity and density measurements at two or more temperatures.

$$\alpha_P = -\frac{\beta E_v}{\alpha_T 2CRT^2} \quad (10)$$

Where: β is the coefficient of compressibility;
 α_T is the coefficient of thermal expansivity;
 E_v is the activation energy required for viscous flow;
 T is the temperature;
 R is the universal gas constant;
 C is a constant to be identified.

On the other hand, a non-linear behaviour is usually accounted for solving an additional constitutive equation which does not take into account the effects of temperature and pressure. The simple models for non-linear behaviour laid out in Sec. 4.2.1 are however inadequate to fulfil the role of constitutive equations as they are not able to predict many of the aforementioned non-Newtonian features. For example, they do not contemplate the presence of a shear strength, that is one of the most important non-Newtonian features.

The interaction among molecules is the determinant of the shear strength expressed in terms of a limiting shear stress.

Real fluids cannot withstand the increase in shear stress indefinitely: there is a critical shear stress at which the lubricant will flow plastically. This limit is called *shear strength* of the lubricant and is the function of the operating pressure and temperature in its turn. No further increase in shear stress will occur if shear strain rate is still heightened because above that limit the molecular layer is able to slip on its neighbours. This phenomenon is related to the reordering of the lubricant structure at the molecular scale: long and randomly orientated molecules suspended into the “suspension medium” tend to align along the shearing direction to minimize the deformation energy. Under increasing pressure, the mean distance among molecules is reduced and stiffness rises as result of the packing of these ordered structures. Under increasing temperature levels, instead, the molecular shaking intensifies, and the molecular mean free path increases. It follows that higher shear strength is then driven by pressure and fought by temperature.

Non-Newtonian rheological models shall be classified in the following categories according to how limiting shear stress is dealt with:

- Monotone models;
- Viscoplastic models;
- Asymptotic limiting-shear-stress viscous models.

In *monotone models* the mathematical function increases without any upper limit and is defined even above the limiting shear stress. The non-linear viscous model by Eyring is the foremost example of monotone model. Linear and non-linear *viscoelastic models* fall within this category too. Maxwell model is the most commonly used viscoelastic model: it can be represented as the series of a linear spring (elastic share) and a Newtonian damper (viscous share).

Viscoplastic models include the occurrence of a limiting shear stress by resorting to a sharp transition into a perfectly-plastic behaviour. The simple case of viscoplastic behaviour is the linear viscoplastic model that combines the Newtonian viscous response up to the shear limit and a perfectly plastic

response for higher strain rate. This kind of description of reality accepts that a certain amount of slippage should occur either within the oil film or at the solid-liquid interface once shear stress approaches the clipping value (the hypothesis is that the lubricant starts behaving like an *inviscid liquid*). Some modified monotone models fall within this group. Since the monotone behaviour is physically inconsistent for most lubricants, the upper bound of shear stress has to be “forced” with a sudden plastic transition, i.e. a horizontal cut of the function. For example, a viscoplastic variant of the Eyring model has been attempted by some authors [12].

Asymptotic limiting-shear-stress viscous models are non-linear viscous models whose mathematical function exhibits a horizontal upper asymptote coinciding with the shear strength. None of the values of shear stress exceeding this limit can ever be reached.

Table 4.4. Synoptic presentation of different viscosity models

Model category	Fluid model	Shear strain rate	Year
Linear viscous	Newtonian (linearly plastic)	$\dot{\gamma} = \frac{\tau}{\eta}$	1886
Plastic	Rigid-perfectly plastic	$\tau = \tau_L \quad \forall \dot{\gamma}$	
	Ree-Eyring (non-linear viscous)	$\dot{\gamma} = \frac{\tau_E}{\eta} \sinh \frac{\tau}{\tau_E}$	1936
Monotone	Maxwell (linear viscoelastic)	$\dot{\gamma} = \frac{\tau}{\eta} + \frac{1}{G} \frac{d\tau}{dt}$	
	Johnson-Tevaarwerk (non-linear viscoelastic)	$\dot{\gamma} = \frac{\tau_E}{\eta} \sinh \frac{\tau}{\tau_E} + \frac{1}{G} \frac{d\tau}{dt}$	
Viscoplastic	Linear viscoplastic	$\dot{\gamma} = \frac{\tau}{\eta} \quad \eta \dot{\gamma} \leq \tau_L$ $\tau = \tau_L \quad \eta \dot{\gamma} > \tau_L$	
	Modified Ree-Eyring (non-linear viscoplastic)	$\dot{\gamma} = \frac{\tau_E}{\eta} \sinh \frac{\tau}{\tau_E} \quad \eta \dot{\gamma} \leq \tau_L$ $\tau = \tau_L \quad \eta \dot{\gamma} > \tau_L$	
	Bair-Winer (logarithmic model)	$\dot{\gamma} = \frac{\tau_L}{\eta} \ln \left(1 - \frac{\tau}{\tau_L} \right)^{-1}$	1979
	Gecim -Winer (\tanh^{-1} model)	$\dot{\gamma} = \frac{\tau_L}{\eta} \tanh^{-1} \tau$	1980
Asymptotic limiting-shear- stress viscous	Ivonen-Hamrock (straight-line model)	$\dot{\gamma} = \frac{\tau_L}{\eta} \left(\left(1 - \frac{\tau}{\tau_L} \right)^{-1} - 1 \right)$	1989
	Elsharkawy-Hamrock (exponential model)	$\dot{\gamma} = \frac{\tau}{\eta} \left(1 - \left(\frac{\tau}{\tau_L} \right)^n \right)^{-1/n}$	1991
	Lee-Hamrock (circular model)	$\dot{\gamma} = \frac{\tau}{\eta} \left(\sqrt{1 - \left(\frac{\tau}{\tau_L} \right)^2} \right)^{-1}$	1990

Where: τ is the applied shear stresses;
 τ_L is the (limiting) shear strength;
 τ_E is shear stress at which the fluid first starts to behave nonlinearly;
 η represents here a constant to be identified.

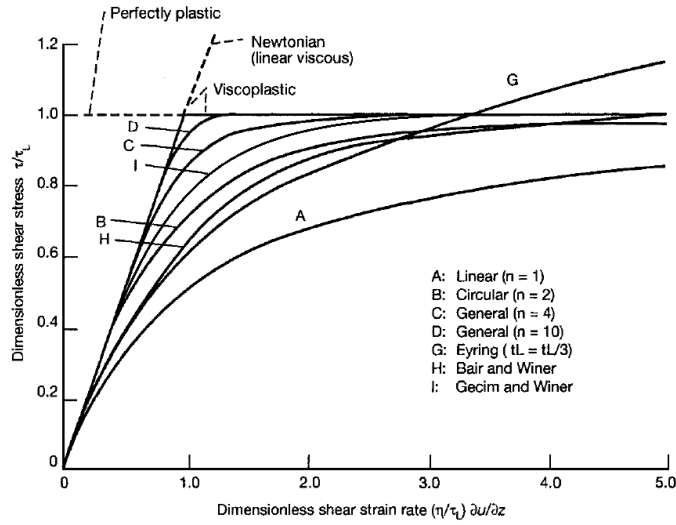


Figure 4.7. Dimensionless diagram of Non-Newtonian rheological models (MODIFFFFFFF)

Modified from: B.J.Hamrock, S.R.Schmid, B.O.Jacobson, *Fundamental of Fluid Film Lubrication*, II Ed., Marcel Dekker, 2004

Table 4.4 lists a variety of rheology models available in the scientific literature and successfully applied in elastohydrodynamic contacts under different working conditions by different authors. These models are compared with the two reference borderline models: the linear Newtonian models and the rigid-perfectly plastic model.

The main rheological viscous model are listed in Table 4.4 and the corresponding trend is displayed in Figure 4.7 by means of dimensionless quantities. In the case of Eyring model, the quantity τ_E is normally linked to τ_L by means of a relationship of this kind: $\tau_E = (3 \div 5)\tau_L$. For the sake of the comparison, τ_E is assumed equal to 3 in Figure 4.7.

As said above, all these models do not take into account that viscosity is a function of pressure and temperature. An attempt to merge chemical thermal and mechanical properties in one constitutive model is ascribed to Huang et al. [15] who proposed the following formula:

$$\tau = \frac{\eta_0 \dot{\gamma}}{\alpha \dot{\gamma}^2 + 1} \quad (11)$$

Where: $\alpha = 2\beta x \eta_0 / \rho c u$;
 β is the Reynolds viscosity-temperature exponent;
 x is the distance away from the inlet;
 c is the specific heat capacity of the lubricant;
 η_0 is a constant;
 u is the entrance velocity of the lubricant.

Last but not least, heavily loaded elasto-hydrodynamic contacts suffer huge pressure, so high that liquid lubricants are no longer considered an incompressible medium. Dowson and Higginson [16] proposed the following law to consider the dependence of density on pressure:

$$\rho_p = \rho_0 \left(1 + \frac{0.6p}{1 + 1.7p} \right) \quad (12)$$

This simple formula makes it possible to correctly predict changes in lubricant density only for mineral oils (i.e. with simple rheology) under low pressure. Figure 4.8 clearly shows that a conspicuous deviation from the experimental data appears above 2GPa in case of a mineral naphthenic distillate.

A more refined model was proposed by Hamrock et al. [12]. They considered the change of relative volume with change of pressure dV_r/dp as a fundamental parameter. As long as pressures is less than the solidification pressure p_s , a small change in pressure results in a large change in relative volume. In these conditions, the distance between the molecules becomes smaller and smaller. For pressures above p_s , there is, on the contrary, little change in relative volume because the molecules are no longer free to move: any further compression will result in deformation of the molecules themselves. Since the rate of pressure increase is extremely high, the lubricant will have no time to crystallize but will be compressed to an amorphous pasty solid.

Hamrock model for density provides very good agreement with experimental values; evidence of this are the dashed lines in Figure 4.8. No further information about this model will be given in the following model: the reader can find more details in the textbook by Hamrock et al. [12].

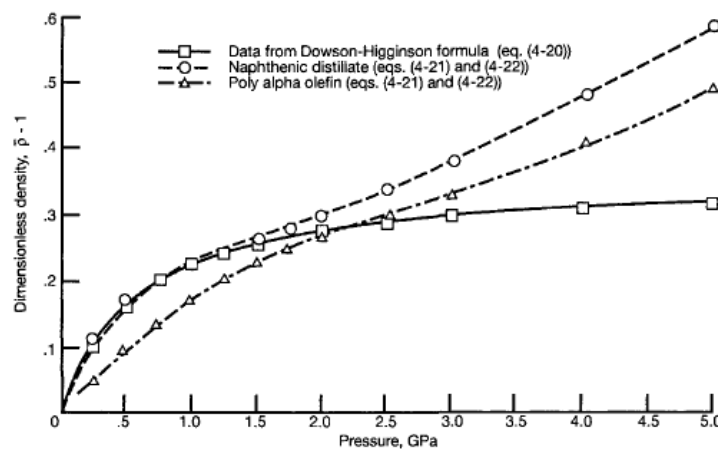


Figure 4.8. Effect of pressure on density for a mineral base stock and a synthetic lubricant
B.J.Hamrock, S.R.Schmid, B.O.Jacobson, *Fundamental of Fluid Film Lubrication*, II Ed., Marcel Dekker, 2004

4.3 THE EHL CLASSICAL THEORY FOR POINT CONTACT

The elastohydrodynamic lubrication (herein referred to as either EHL or EHD) is a very particular and extreme form of lubrication common to many industrial applications in which the following effects play a central role:

- Hydrodynamic film formation;
- Elastic deformation of solid surfaces;
- Rheological behaviour of the lubricant (and its dependents to pressure and temperature);
- Compressibility of the liquid lubricant under high pressure;
- Thermal effect due to contact heating.

These main aspects of EHL will be analysed throughout this section, whereas in Sec. 4.4.2 it will be examined how their relative importance promotes evolution towards different forms of lubricated contacts.

Table 4.5 is a synoptic presentation of the different types of lubricated contacts, the physical effects involved and the background equations to be dealt with.

The EHL is a regime of lubrication which characterises any kind of non-conformal contact, both nominal line (e.g. cylinder-on-flat) and nominal point contacts (e.g. ball-on-flat). The discussion of these two cases is similar but at the same time requires an own theory: a 1D approach is enough for line

contacts whereas a more complex 2D approach is unavoidable for point contacts. Hereinafter, reference is made to this latter case since it is the one of interest for the present experimental investigation.

Table 4.5. Different types of lubricated contacts with their fundamental equations

Type of lubricated contact		Effect	Physical Principle	Equation	
TEHL	HL	Hydrodynamic film formation	Conservation of Momentum	Reynolds equation (Navier-Stockes)	
			Conservation of mass		
	EHL		Elastic deformation of solid surfaces	Elasticity	Hertzian contact (Boussineque)
			Compressibility of liquid lubricant	Liquid compressibility	$\rho = \rho(\beta, p)$
			Piezo-viscous behaviour of lubricant	Lubricant rheology	$\eta = \eta(p, T);$
			Non-linear behaviour of lubricant		Rheological model
			Heat transfer	Conservation of Total Energy	First law of Thermodynamics
			Contact heating	Mechanical energy balance	$L_w = L_w(\mu, \bar{u})$
			Thermal expansion of liquid lubricant	Thermal expansion	$\rho = \rho(\alpha_T, T)$

Thermal effects will be in the first instance overlooked as they play a crucial role in highly stressed lubricated contact only, called termo-elasto-hydrodynamic contacts (TEHL).

Let us start analysing the *hydrodynamic effect* introducing the *Reynolds equation*. Reynolds put forward the equation named after him in a celebrated analytical paper dating back to 1886 setting up the foundation of the hydrodynamic lubrication theory [17]. This second-order partial differential equation comes from the flow continuity equation and a reduced form of the Navier-Stockes equation. It successfully reveals, under a number of hypothesis, the fundamental mechanism of hydrodynamic lubrication: a flowing fluid generates dynamic pressure into the narrow converging gap between bearing surfaces.

Reynolds equation (equation (13)) can be derived from the Navier-Stockes equation and can be thought as one of its particular forms. It describes the flow condition known as “slow viscous motion”, where inertial and mass forces terms are neglected. However, it can be proved that Reynolds equation can be equally derived through the balance of forces acting on an infinitesimal body [12].

This paper does not go beyond the final outcome of this derivation process in local form (further information is available in specific textbooks, see [9] , [18], [13]).

$$\frac{\partial}{\partial x} \left(\frac{\rho h^3}{12\eta} \frac{\partial p}{\partial x} \right) + \frac{\partial}{\partial y} \left(\frac{\rho h^3}{12\eta} \frac{\partial p}{\partial y} \right) = \frac{\partial}{\partial x} \left(\frac{U\rho h}{2} \right) + \frac{\partial}{\partial y} \left(\frac{V\rho h}{2} \right) + \rho(w_a - w_b) - \rho u_a \frac{\partial h}{\partial x} - \rho v_a \frac{\partial h}{\partial y} + h \frac{\partial \rho}{\partial t} \quad (13)$$

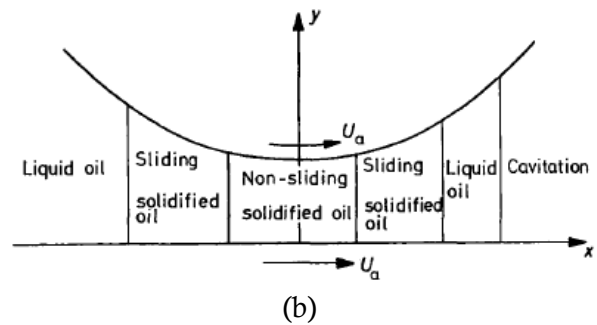
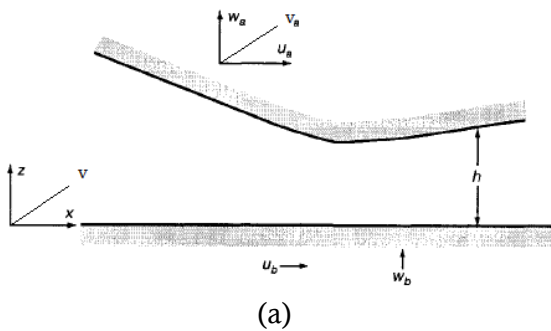
Where: h is the local film thickness
 $U = u_a + u_b$ is the relative sliding velocity between body ‘a’ and ‘b’ in x-direction;
 $V = v_a + v_b$ is the relative sliding velocity between body ‘a’ and ‘b’ in y-direction.

The basic assumptions for this equation are listed in Table 4.6.

Table 4.6. Reynolds equation hypothesis

From: S.Wen, P.Huang, *Principles of Tribology*, John Wiley & Sons, 2012

1. Ignore the body forces such as gravity force, magnetic force, and so on.
2. There is nonslip on the interface between solid and liquid. That is, the molecules of liquid are firmly affixed to the solid surface moving with the same velocity.
3. Across the film thickness, ignore the variations of pressure. Although this assumption is not accurate, however, as the film thickness is only a few micro-meters or less, pressure cannot significantly vary.
4. The film thickness compared to the radius of the bearing surface can be ignored. Therefore, to neglect the influence of film curvature, linear velocity is used to calculate the rotational speed instead.
5. Lubricants are Newtonian. This assumption is reasonable for most mineral oils in general working conditions.
6. The flow is laminar and it is not a boundary layer or turbulence. Only for high velocity and large-scale bearings may it be a turbulence.
7. Compared with the viscous force, the inertia force can be ignored, including the acceleration force and centrifugal force. However, the effects of the inertial force should be considered for high velocity and large-scale bearings.
8. Across the lubricant film thickness, viscosity remains unchanged. This assumption is just for mathematical convenience.



B.J.Hamrock, S.R.Schmid, B.O.Jacobson, *Fundamental of Fluid Film Lubrication*, II Ed., Marcel Dekker, 2004

B.O. Jacobson, *Rheology and Elastohydrodynamic Lubrication*, Elsevier, Amsterdam, 1991

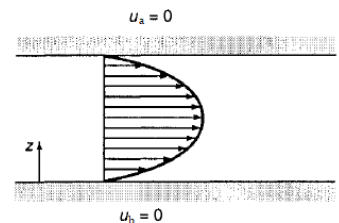
Figure 4.9. (a) Components and coordinates for hydrodynamic problem; (b) state of the lubricant inside the contact

Figure 4.9a illustrates the velocity components and the coordinates used in Reynolds equation in the z - x plane. Equation (13) is a general form in which the variability of density is possibly taken into account. Reynold equation applied to HD condition, being ρ constant, it is simply eliminated from each derivative. By expanding the derivatives of quantities $U\rho h$, $V\rho h$ and ρh , it is possible to recognise a different physical effect on pressure from each term.

1. Poiseuille terms

Net flow rate within the lubricated area due to the variation of pressure along the contact.

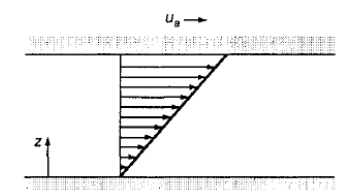
$$\frac{\partial}{\partial \dots} \left(\frac{\rho h^3}{6\eta} \frac{\partial p}{\partial \dots} \right)$$



2. Couette terms

Net entraining flow rate due to the drag effect of surfaces in relative motion.

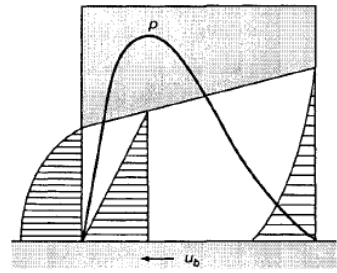
$$\frac{\partial}{\partial x} \left(\frac{U\rho h}{2} \right); \frac{\partial}{\partial y} \left(\frac{V\rho h}{2} \right)$$



3. Wedge Effect term

The fluid flows along a clearance getting narrower leads to a positive pressure peak. A Poiseuille flow is superimposed with reduction of the flow at the inlet and increase at the outlet, for continuity of mass.

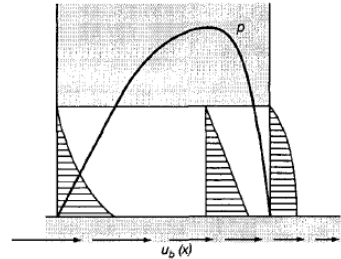
$$U\rho \frac{\partial h}{\partial x} ; V\rho \frac{\partial h}{\partial y}$$



4. Surface stretch effect term

If the surface changes in length due to an elastic reaction, a relative speed distribution is generated along the contact. If the stretch is forward with decreasing velocities in sliding direction, a positive peak of pressure arises.

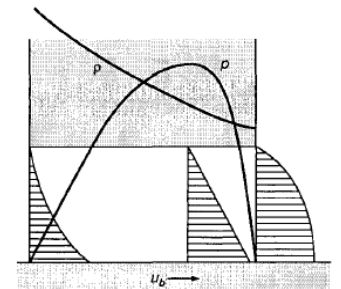
$$\rho h \frac{\partial U}{\partial x} ; \rho h \frac{\partial V}{\partial y}$$



5. Density wedge effect term

If a gradual decrease in density occurs (frictional heating effect may cause it) Couette mass flow rate increases for continuity of mass. A balancing Poiseuille flow is generated.

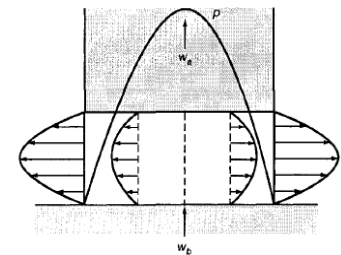
$$Uh \frac{\partial \rho}{\partial x} ; Vh \frac{\partial \rho}{\partial y}$$



6. Normal squeeze effect term

Pressure is generated because the two surfaces come closer one another under a normal force. This effect is however there in non-static conditions only.

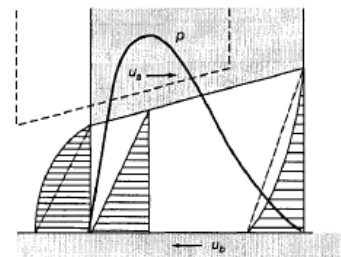
$$\rho(w_a - w_b)$$



7. Translation squeeze effect terms

Pressure is generated since two inclined surfaces come locally closer to each other due to a relative motion.

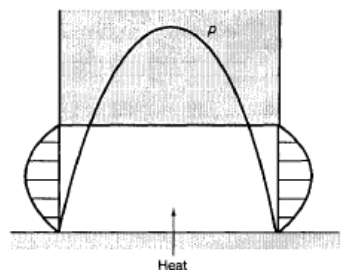
$$-\rho u_a \frac{\partial h}{\partial x} ; -\rho v_a \frac{\partial h}{\partial y}$$



8. Local expansion term

The pressure generating mechanism is linked to thermal expansion due to heat supplied to the lubricant.

$$h \frac{\partial \rho}{\partial t}$$



Images from: S B.J.Hamrock, S.R.Schmid, B.O.Jacobson, *Fundamental of Fluid Film Lubrication*, II Ed., Marcel Dekker, 2004

The main effect is always the hydrodynamic one, with the squeezing effect having a significant role if dynamic loads are applied to the contact. Equation (13) can be further reduced to a form far easier to handle in computational application without losing of generality:

$$\frac{\partial}{\partial x} \left(\frac{\rho h^3}{12\eta} \frac{\partial p}{\partial x} \right) + \frac{\partial}{\partial y} \left(\frac{\rho h^3}{12\eta} \frac{\partial p}{\partial y} \right) = \frac{\partial}{\partial x} \left(\frac{U\rho h}{2} \right) + \frac{\partial}{\partial y} \left(\frac{V\rho h}{2} \right) + \frac{\partial \rho h}{\partial t} \quad (14)$$

Equation (14) is exactly Equation (13) under the hypothesis that:

$$\rho(w_a - w_b) - \rho u_a \frac{\partial h}{\partial x} - \rho v_a \frac{\partial h}{\partial y} + h \frac{\partial \rho}{\partial t} = \frac{\partial(\rho h)}{\partial t} \quad (15)$$

It is possible to demonstrate the latter identity is always valid simply by developing the total derivative of the thickness $h = h(x, y, t)$ in terms of partial derivatives and arguing that $Dh/Dt = (w_a - w_b)$ [12]. Equation (14) is very effective for the study of EHD nominal point contact. Furthermore, in many common applications to mechanical components, velocity components are not function of the coordinates x and y and steady-state conditions holds (that is however not true for some relevant mechanical applications, e.g. cam-follower coupling, gear-teeth couplings...). Reynolds equation becomes:

$$\frac{\partial}{\partial x} \left(\frac{\rho h^3}{\eta} \frac{\partial p}{\partial x} \right) + \frac{\partial}{\partial y} \left(\frac{\rho h^3}{\eta} \frac{\partial p}{\partial y} \right) = 12u \cdot \frac{\partial(\rho h)}{\partial x} + 12v \cdot \frac{\partial(\rho h)}{\partial y} \quad (16)$$

Where: h is the local film thickness
 $u = (u_a + u_b)/2$ is the entrance velocity in x-direction;
 $v = (v_a + v_b)/2$ is the entrance velocity in y-direction.

Moreover, the hypothesis of unidirectional flow and side leakages are usually added even in nominal point contact and the terms containing v and $\partial/\partial y$ become null. These hypotheses are justified with two argumentations: first the oil experiences a rapid transit time through the contact and it has no time to flow sideways; second, it is compressed up to a nearly solid state (see Figure 4.9b).

Every differential equation needs boundary conditions. In literature different boundary conditions in terms of $p(x, y)$ are known for Reynolds equation:

- Sommerfeld condition: $p = 0$ at $x \rightarrow \infty ; y \rightarrow \infty$
- Half- Sommerfeld condition: $p = 0$ at $x \geq 0 ; y \geq 0$
- Reynolds condition: $p = 0$ at $\partial p / \partial x = 0 ; y \partial p / \partial y = 0$

In case unidirectional flow is assumed, taken x as the direction of flow, the boundaries conditions should be defined with respect to x only.

Integration of equation (16) provides the pressure distribution into an elasto-hydrodynamic contact. Clearly, the film thickness $h = h(x, y)$ at the contact area must be known. Elastic deformation of surfaces plays an important role in the formation of a supporting film thickness, but the actual distance between the solid surfaces is not merely related to it. The film thickness profile is calculated taking into account the various contributions depicted in Figure 4.10. The case of a sphere contacting a plane will be analysed in the following as it the type of contact reproduced in the experimental investigation outlined in Sec. 6.

If bodies were rigid, the profile would follow the geometrical separation of the contacting bodies, i.e. it would adapt to their silhouette (dashed lines in Figure 4.10). In the surroundings of the minimum of the gap, the sphere of radius R can be approximated with an elliptic paraboloid whose projection on x - z plane is the grey solid line. The function for h would then take the form:

$$h(x, y) = h_f + \frac{x^2}{2R_x} + \frac{y^2}{2R_y} + r(x, y) \quad (17)$$

Where: h_f is the minimum of the gap; its value is related to the hydrodynamic effect of the converging solid edge;
 R_x is the composite curvature in x - z plane;

R_y is the composite curvature in the y-z plane;
 $r(x, y)$ is a (statistical) function that takes into account the surface rugosity [19].

Surface rugosity is usually neglected in numerical analysis in order to simplify calculations. Surfaces are considered technically smooth and the effect of roughness is indirectly introduced by means of the Λ ratio. Surface rugosity may have large influences on the hydrodynamic effect at the contact. The flatter the geometries, the thicker the film formed while high surface ridges promote the braking of the fluid film continuity as well as its supporting effect [20].

The presence of elastic deformation is accounted for through the theory of elastostatics [21]. As seen in Sec. 4.2.3, if a certain amount of lubricant is interposed between two bodies into a non-conformal contact the extreme high pressure causes the behaviour and the physical state of a liquid lubricant to be much more akin to a pasty solid. The deformations should not differ so much from those of a dry Hertzian contact and then, to a first approximation, the Hertzian theory might apply [22]. Since a linear elastic model is resorted to, superimposition of effects is possible and equation (17) modifies by the sum of an additional term:

$$h(x, y) = h_f + \frac{x^2}{2R_x} + \frac{y^2}{2R_y} + r(x, y) + \delta(x, y) \quad (18)$$

Where: $\delta(x, y) = h_{eA} + h_{eB}$ is the combined elastic deformation of the solids.

Figure 4.10 depicts the deformation of a sphere contacting a plane in the x-y plane (the same would appear in the z-y plane for spherical symmetry). The deformation of the lubricated surfaces is calculated resorting to the theory of elasticity [23] by means of the following equation:

$$\delta(x, y) = \frac{2}{\pi E^*} \iint_{\Omega} \frac{p(f, g)}{\sqrt{(x-f)^2 + (y-g)^2}} df dg \quad (19)$$

Where: E^* is the *composite elastic modulus* of the mating surfaces, defined in equation (20);
The denominator represents the radius of the contact region in Cartesian coordinates;
 Ω is the given dominion of integration.

$$E^* = \frac{2}{\frac{1 - \nu_1^2}{E_1} + \frac{1 - \nu_2^2}{E_2}} \quad (20)$$

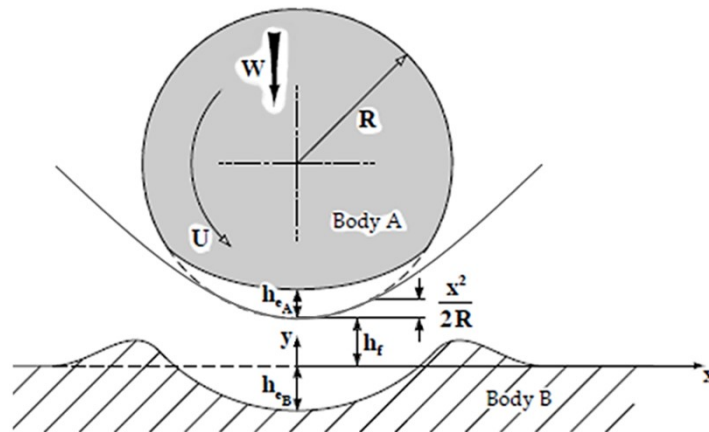


Figure 4.10. Lubricant film profile in the x-z plane for a ball-on-flat contact configuration.
G.W. Stachowiak, A.W. Batchelor, *Engineering Tribology*, Butterworth-Heinemann, 2005

Substituting (19) into the Reynolds equation, the pressure distribution can finally be obtained. The exact analysis of elastohydrodynamic lubrication involves the simultaneous iterative numerical solution of equations (16) and (19), plus three equations: one for the piezoviscous response, the second for the

Figure 4.12. (a) Thickness map for an EHL point contact; (b) corresponding 3D representation

Figure 4.12 a illustrates the typical 2D map of the thickness distribution in an EHL point contact. The opposing surfaces are almost parallel in the centre of the contact where their distance is described by the so-called *central film thickness* h_c . The end constriction has to be curved in order to fit into the contact boundary; this effect is known as the *horse-shoe constriction*. The *minimum film thickness* h_{min} is found at both ends of the ‘horse-shoe’ and is experimentally estimated about 60% of the central value. The minimum film thickness is usually the most remarkable parameter since it “controls” the likelihood of asperity interaction between the two surfaces.

Be aware of h_c and h_{min} is crucial for engineers involved in the design process of any mechanical component working under lubricated conditions. However, the numerical solution of the elastohydrodynamic problem is not an easy way and is impracticable above all in the early stages of the design process.

It would be much more expedient to dispose of analytical formulæ for the calculation of the central and minimum film thickness in other to have a quick and simple (although rather accurate) estimate. The most famous formulae are those derived by Hamrock and Dowson [22] which apply to any contact, such as point, linear or elliptical under the hypothesis of *pure rolling*. They can be used with confidence for many material combinations even up to maximum pressures of 3÷4GPa.

$$\frac{h_c}{R'} = \left(\frac{U\eta_0}{E^*R'} \right)^{0.67} \cdot (\alpha E')^{0.53} \cdot \left(\frac{W}{E^*R'^2} \right)^{-0.067} \cdot (1 - 0.61e^{-0.73k}) \quad (21)$$

$$\frac{h_{min}}{R'} = \left(\frac{U\eta_0}{E^*R'} \right)^{0.68} \cdot (\alpha E')^{0.49} \cdot \left(\frac{W}{E^*R'^2} \right)^{-0.073} \cdot (1 - e^{-0.68k}) \quad (22)$$

Where: U is the entraining velocity: $U = (U_A + U_B)/2$ [m/s];
 η_0 the viscosity at atmospheric pressure of the lubricant [Pa s];
 E^* is the reduced Young's modulus [Pa];
 R' is the reduced radius of curvature [m];
 α is the Barus pressure-viscosity coefficient [m²/N];
 W is the normal load [N];
 k is the ellipticity parameter: $k = a/b$ where ‘a’ is the semiaxis of the contact ellipse in the transverse direction [m] and ‘b’ is the semiaxis in the direction of motion [m].

These formulae can be conveniently written using the non-dimensional parameters introduced by Hamrock and Dowson:

$$H_{min}^* = 3.63 \frac{G^{*0.49} U^{*0.68}}{W^{*0.073}} (1 - e^{-0.68k}) \quad (23)$$

$$H_c^* = 2.69 \frac{G^{*0.53} U^{*0.67}}{W^{*0.067}} (1 - 0.61e^{-0.73k}) \quad (24)$$

Where:	$H^* = \frac{h}{R'}$	$U^* = \frac{U\eta_0}{E^*R'}$	$G^* = \alpha E'$	$W^* = \frac{W}{E^*R'^2}$
	Film parameter	Speed parameter	Materials parameter	Load parameter

A further generalisation was done by Chittenden et al. [26] that extended these formulae to the general case of an entrainment velocity oriented in any direction with respect to the semiaxis of the contact ellipse.

It is important to underline that the non-dimensional parameters in above have a strong influence pressure and film thickness. The influence of each parameter is analysed in the following by comparing the pressure profile at the median plane and the thickness profile at a plane passing through one of the two horse-shoe edges.

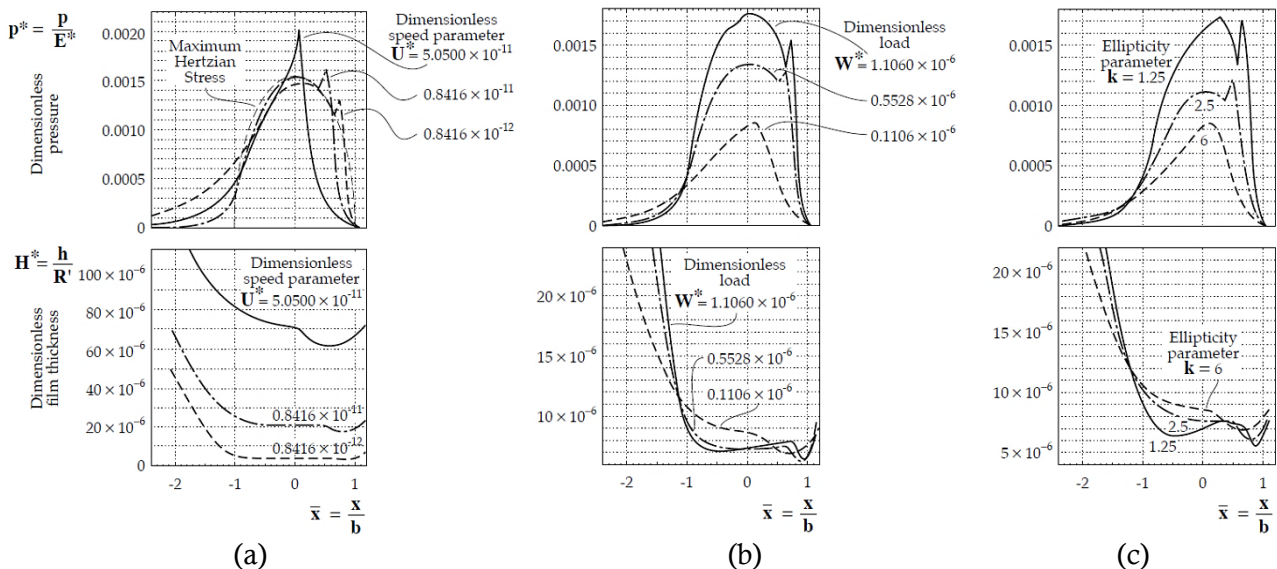


Figure 4.13. Synoptic view of the effects on pressure and thickness profile attributable to parameters U^* , W^* and k
G.W. Stachowiak, A.W. Batchelor, *Engineering Tribology*, Butterworth-Heinemann, 2005

High values of the speed parameter cause a radical distortion of the pressure profile from the Hertzian ellipsoidal and a profile with a sharply pointed peak appears. This peak tends to grow and migrate towards the inlet region as the value of U^* increases. The film thickness profile is also affected, three main effects are noticeable in figure a:

- The film thickness increases;
- the proportion of contact area where the two surfaces are virtually parallel reduces;
- the proportion of contact area covered by the exit constriction increases.

Load has the effect of reducing both the central film thickness and the minimum film thickness at the exit constriction. Despite this, a re-entrant profile could appear between the inlet and the exit constriction and it is attributed to lubricant compressibility. The interesting effect on hydrodynamic pressure is that increasing the load, the pressure becomes almost completely confined inside the Hertzian circle so that at the inlet it actually declines. As to the ellipticity parameter, the film thickness increases in proportion to k because the relative widening of the contact promotes the generation of hydrodynamic pressure by limiting side leakage. The pressure spike is also concerned, and it can disappear for high values of k . The material parameter influences the pressure and thickness profiles, but it is not always the same. The quantities defining G , such as the reduced Young's modulus, are also included in other non-dimensional parameters; therefore, it is difficult to quantify its own effect on EHL.

Experimental tests make it clear that the most influencing parameter is speed. This is perfectly consistent as the dimensional velocity is the main responsible of the hydrodynamic supporting effect. Load on the contrary is a minor parameter and even though it pushes down the minimum film thickness, its effect is marginal.

All the results presented up to now are valid under the implicit assumption that the contact is:

- isothermal (no appreciable change in temperature due to frictional heating);
- fully flooded;
- characterized by pure rolling.

A *fully flooded* contact is achieved if the oil quantity is enough to ensure a total filling of the inlet region. The precondition is that the lubricant film outside the contact is equal or greater than the gap between the solid surfaces. There are conditions in which *starvation* occurs and actual film thickness are much smaller than those predicted as not enough lubricant is dragged into the contact. Other situations are characterised by pronounced thermal effects and the energy conservation equation has to be included in the numerical solution to account for variation in viscosity due to the temperature. The reader can refer to specific scientific papers dealing with these two important issues.

The presence of sliding can deeply change the behaviour of the contact, as an extra stress is borne by the lubricant. Sliding motion in EHL contacts is usually described by means of *slide-to-roll ration* which is conventionally defined as²:

$$SRR = \frac{2 \cdot (u_a - u_b)}{(u_a + u_b)} \quad (25)$$

Where: u_a, u_b are the linear speed at the surfaces of the mating body

SRR is equal to zero when pure rolling occurs, it is equal to 2 when pure sliding occurs, and it can also take values above 2 if the mating surfaces have reversed direction.

The presence of shear stress causes heating at the contact. Smeeth and Spikes [14] observed the diminution in film thickness and eventual failure due to sliding and attributed it to the fall of α because of heating effects at the inlet.

Though, sliding is responsible for the change in the profile of the lubricant film too. One of the best-known and investigated phenomena is the so-called *dimple* that leads to anomalous film shape and may affect the coefficient of friction. Chiu and Sibley [27] observed first a dimple in the central region of an EHL contact instead of the conventional plateau. Kaneta [28], Kaneta and Yang [29], Guo and Wong [30], Yang [31], Fu et al. [32] and other authors explained experimentally and numerically the occurrence of dimples with *the temperature-viscosity wedge effect*. Some pointed out that materials with different thermal properties are particularly prone to give rise to the “dimple effect”. These works all referred to conditions particularly prone to temperature rise, as coexistence of high values of the non-dimensional speed U^* and high slide to roll ration was there.

Ehret et al. [33] proposed the *isothermal (wall) slippage* as an alternative explanation and later Fu et al. [32] reinforced this claim by finding a drastic reduction in friction coefficient in the full-film regime due to the presence of a dimple in isothermal contact condition. The isothermal slippage is the lubricant failure by quasi-solid shear. It can take place either within the oil film or the interface between a liquid and a solid surface (in apparent contradiction with some basic principles of fluid mechanics). In either case, a discontinuity in the velocity profile is detected. This concept is illustrated schematically in the following image.

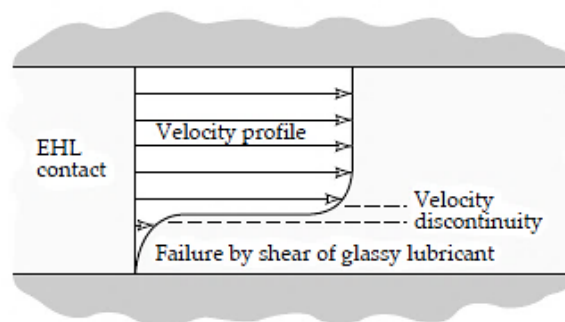


Figure 4.14. Lubricant slip in a sliding EHL contact

G.W. Stachowiak, A.W. Batchelor, *Engineering Tribology*, Butterworth-Heinemann, 2005

² It must be noted that this conventional formula for SRR is not universally accepted, many authors use custom equations.

Lubricant slip is claimed to correlate with the *glass transition* which is in turn responsible for the shear strength of the lubricant mentioned above. It is still not clear, however, whether a direct relationship does exist [13]. The glass transition is function of the pressure for common lubricants: at an atmospheric pressure closer to 0°C, whereas at pressures of about 1GPa, the transition takes place at about 100°C or higher. It means that the resultant change from the liquid state to a pasty or glassy state under the conditions of extreme pressure is achieved even though thermal effects are relatively strong.

Recently, Carli at al. [34] numerically predicted a huge temperature rise localized around the centre of the dimple for extreme values of the SRR but suspected that thermal effects (and thermal properties) and should coexist with wall slippage effects.

4.4 LUBRICATION REGIMES

Liquid lubrication regimes are classified according to the so-called Λ factor, defined as follows:

$$\Lambda = \frac{h_{min}}{\sqrt{R_{q1}^2 + R_{q2}^2}} \quad (26)$$

Where: h_{min} is the shear stress [mm];
 $\sqrt{R_{q1}^2 + R_{q2}^2}$ is the composite roughness;
 R_{q1}, R_{q2} are the root-mean-square roughness values of the two bodies.

The value of the coefficient Λ opens up the possibility to define three important lubrication regimes:

1. Boundary lubrication $\Lambda < 1$
2. Mixed (or partial) lubrication $1 < \Lambda < 3$
3. Fluid film lubrication $\Lambda > 3$

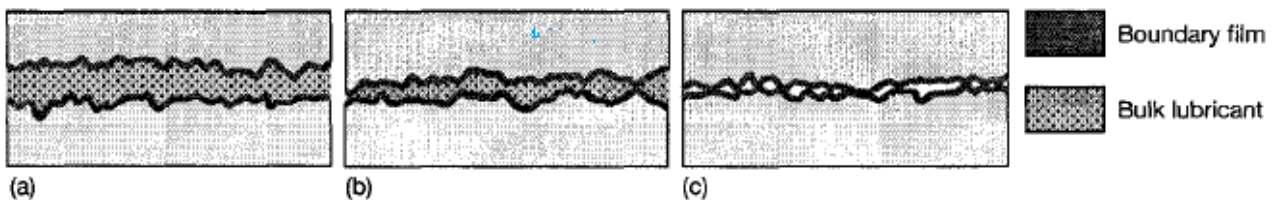


Figure 4.15. Lubrication regimes: (a) Fluid film, (b) mixed and (c) boundary.

B.J. Hamrock, S.R. Schmid, B.O. Jacobson, “*Fundamental of Fluid Film Lubrication*”, II Ed., Marcel Dekker, 2004

4.4.1 Boundary lubrication

In boundary lubrication film thickness is very small, less than the composite surface roughness and the surface asperities come considerably into contact. The sole role of the lubricant is to avoid direct solid-solid interaction, thereby mitigating the adhesive mechanism, but its viscosity is of minor importance and the friction coefficient is essentially independent from the lubricant properties. In the same way, the formation of a thin lubricating film of molecular proportion is independent from the physical properties of lubricants. Among all the lubrication regimes, this one is the toughest to deal with.

Few strongly empirical models exist merely serving as qualitative guides to designers, such as the one by Rowe for the rate of adhesive wear of a boundary lubricated system (let the reader turn to [21] and [9] for further information). The lubricating film settles thanks to mechanisms of physical adsorption or chemical adsorption and it is favoured by the presence of specific additives into the lubricant (see [12] for more details). Physical adsorption occurs when the molecules are held to the surface by reversible Van der Waals forces (i.e. low-energy dipole-dipole interactions). Polar regions of molecules adhere on the surface with preferred vertical orientation of the hydrocarbon molecules and these latter pack in as closely as possible through lateral cohesive forces. Chemical absorption takes place when molecules form high-energy chemical bonding with the solid material. An example is the formation of “metal

soap compounds”. Chemisorbed layers are stronger than physisorbed ones and can resist moderate loads, temperature and sliding velocities, but are not completely reversible.

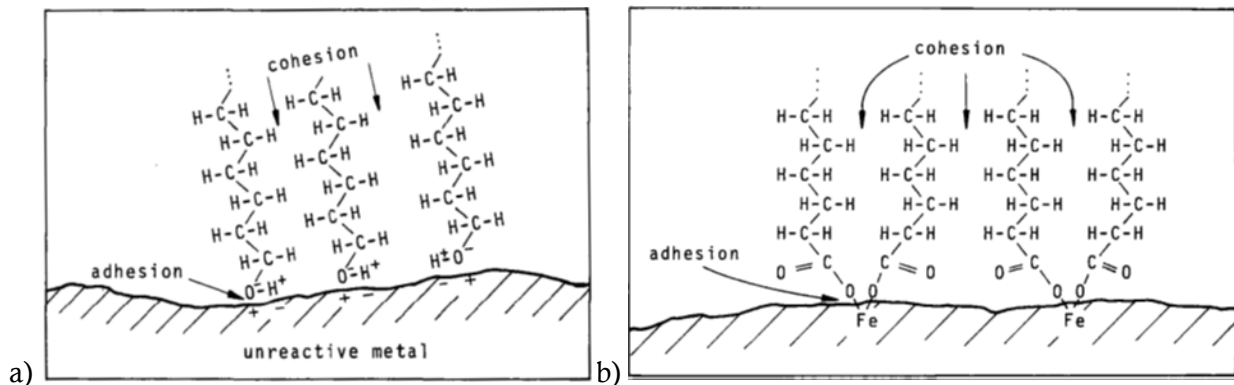


Figure 4.16.a) Physisorption mechanism, b) example of Chemisorption phenomenon

H. Czichos, *Tribology*, Tribology Series Vol.1, Elsevier, 1978

4.4.2 Fluid film lubrication

Fluid film lubrication allows lubricating films thick enough to totally prevent asperities from entering into collision. It is the “ideal” lubrication regime since it provides low friction and practically no wear, even if surface fatigue, cavitation wear and fluid erosion still remain [21]. Fluid film lubrication originates from fluid-dynamic effects in case a relative motion between bodies is there. It is of the fluid-static type in case an external source ensures the lubricant supply at the contact region. Fluid film lubrication is further subdivided into four subsets:

- Hydrodynamic lubrication (or isoviscous-rigid)
- Piezoviscous-rigid lubrication
- Soft Elastohydrodynamic lubrication (or isoviscous-elastic)
- Hard Elastohydrodynamic lubrication (or piezoviscous-elastic)

The main characteristic of a *hydrodynamic lubrication* (HL) is the presence of very thick lubricating films (minimum thickness normally exceeds 1 μm) combined with no elastic deformation of surfaces. The bearing capacity as well as the film thickness is governed by the external load, the relative velocity and the bulk physical properties of the lubricant, with “bulk” meaning the stable properties of the fluid somewhere far from the contact area. This regime is normally associated with *conformal contacts* in which under even very high loads the magnitude of the pressure developed is not large enough to bring about both deformations and important piezo-viscous effects. It is however possible also for concentrated contacts at values $\Lambda > 10$.

Elastohydrodynamic lubrication has been extensively discussed in sec. 4.3. This regime is possible nowhere but in non-conformal contacts where the contact region is limited to some μm^2 , with the typical value of: $3 < \Lambda < 10$.

It is here recalled that elastic deformations of the surfaces and piezo-viscous effect are instrumental. The load-bearing capacity and the film thickness are functions of the relative velocity and the bulk physical properties of the lubricant with the addition of the *composite elastic modulus* and the pressure-viscosity properties. The effective elastic modulus is the combination of the elastic properties of the two mating surfaces and is of such crucial importance that in line with its value the contact may be deemed a *Hard EHL* or a *Soft EHL*. Load is a minor parameter, much less important than in hydrodynamic lubrication.

Hard EHL relates to materials with high composite elastic modulus. It features equally important elastic deformations and piezo-viscous effects, by the fact that under moderate load the maximum pressure soars to 0,5÷3 GPa. Elastic deformation is minimal in absolute terms, but non-negligible since it turns out to become several orders of magnitude larger than the minimum film thickness (about 100

nm). Bulk viscosity is an important baseline value though insufficient to describe the behaviour of the lubricant for its viscosity varies by as much as 10 orders of magnitude within the conjunction.

Soft EHL relates to materials with low elastic modulus (e.g. rubber) which undergo large reversible deformation under light loads. The maximum pressure is about 1 MPa and very thick film are there (about 1 μ m). This kind of regime is closer to the hydrodynamic lubrication as regards key parameters, with the addition of effective elastic modulus of course.

Piezoviscous-rigid lubrication is an intermediate case between HL and EHL. It occurs when the pressure at the conjunction rises up to a level that it is essential to consider the pressure-viscosity characteristics of the lubricant. Rigid body hypothesis still holds because the deformation of the surfaces remains insignificantly tinier than fluid film thickness.

Although the EHL film thickness equations (21) and (22) apply to most cases of fluid film lubrication (see Sec. 4.4) , more precise formulæ can be used for these specific regimes. Table 4.7 is a collection of these formulæ proposed by different authors for diverse EHL conditions. These time equations will be written using the set of 3 fundamental non-dimensional parameters according Johnson: g_V, g_E, \hat{H}, k that are combinations of the Hamrock and Dowson non-dimensional parameters.

Table 4.7. Experimentally fitted equation for different practical EHL conditions

Author	Condition	Experimentally fitted equation
Brewe et al.	Isoviscous-rigid	$(\hat{H}_{\min})_{\text{IR}} = (\hat{H}_c)_{\text{IR}} = 128\alpha_r \left[0.131 \tan^{-1} \left(\frac{\alpha_r}{2} \right) + 1.683 \right]^2 \varphi^2$
Jeng et al.	Isoviscous-elastic	$(\hat{H}_{\min})_{\text{VR}} = (\hat{H}_c)_{\text{VR}} = 141g_V^{0.375} (1 - e^{-0.0387\alpha_r})$
Hamrock and Dowson	Viscous-rigid	$(\hat{H}_c)_{\text{IE}} = 11.15g_E^{0.67} (1 - 0.72e^{-0.28k})$
Hamrock and Dowson	Viscous-elastic	$(\hat{H}_{\min})_{\text{VE}} = 3.42g_V^{0.49} g_E^{0.17} (1 - e^{-0.68k})$

Where:

$g_V = \frac{G^* \cdot W^{*3}}{U^{*2}}$ <p>Viscosity parameter</p>	$g_E = \frac{W^{*8/3}}{U^{*2}}$ <p>Elasticity parameter</p>	$\hat{H} = H^* \cdot \left(\frac{W^*}{U^*} \right)^2$ <p>Film parameter</p>
--	---	--

4.4.3 Mixed lubrication

Mixed lubrication is referred to an intermediate case. In mixed lubrication, the quantity of lubricant is moderate and collision among asperities often exists as the highest peaks are able to reach through the film. The load is carried partly by the contacting asperities and partly by the fluid film that is not enough to support the entire load by itself. Friction resistance is due to both the shearing of the lubricant the asperity interaction and, in principle, all wear mechanisms (see Sec. 678.1.2) may take place. It is important to recognize that the transition between the two opposite conditions is gradual: as the severity of the interaction is increased, a decreasing proportion of the load is carried by the fluid that fills the space between the opposing solids.

Furthermore, it should be noticed that for conformal contacts, the mode of lubrication directly goes from hydrodynamic to partial as the lubricant film thins. For non-conformal ones, the contact comes across the elastohydrodynamic first.

4.4.4 Limits of Lambda factor

Lambda factor introduced at the beginning of this section is largely used to evaluate the “goodness” or “safety” of an EHL condition. $\Lambda_{lim} = 3$ is the conventional and widely accepted safe reference value (proposed for the first time by Sibley in 1971) above which solid contact among asperities disappears and wear suppressed.

The mistake should never be made to believe Λ like a “static” parameter. Of course, the roughness factor evolves in all those systems in which the contact regions undergoes wear, i.e. those working in boundary and mixed lubrication. The *wear-in* phase allows mating surfaces to adjust to each other: modifications of the shape of the asperities are brought about and the peaks which partially support the load become flattened. Low initial Λ values have the tendency to increase by following the modification of the local roughness pattern and this provides for a smooth running.

Certain no-wear lubricated contacts experience evolving value of Λ as well, and this is the most problematic issue related to the use of this parameter. Equation (26) makes use of experimental estimates of surface roughness (R_{q1}, R_{q2}) which are obtained throughout measurements carried out on free, unloaded, dry surfaces. Into an elastohydrodynamic contacts surface ridges encounter large elastic deformation due to high pressure, just as much as bodies do in their entirety. Therefore, the roughness structure conforms within the contact as high pressure manages to flatten the surface ridges, especially those of moderate height [35]. The effect on the lubricant film profile of a ridge passing through a rolling-sliding contact is shown in Figure 4.17. It can be seen that under very high pressures, the shape of the bump and the pressure profile change. A large pressure spike is formed on the bump traversing the contact.

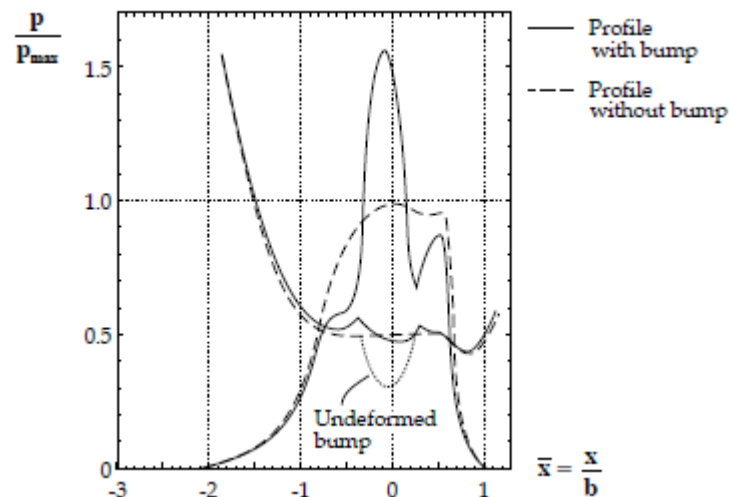


Figure 4.17. Pressure distribution and film thickness when single asperity passes through the EHL contact
G.W. Stachowiak, A.W. Batchelor, *Engineering Tribology*, Butterworth-Heinemann, 2005

The effective Λ value is thus higher than calculated. Furthermore, limiting values of the roughness factor seem to be themselves functions of the measured roughness, so the smoother the surfaces are, the smaller Λ values are required. It is almost as if the shorter the ridges (and less the amount of sliding at the interface) are, more successful the drag effect in conveying lubricant into the contact is.

This is true in pure rolling, but the lubricant action on the asperities changes if sliding speed is introduced into the system. The central (flattened) contact zone is dominated by non-Newtonian behaviour since, as stated above, the lubricant tends to a pasty state. For rolling conditions, the central load carrying zone suffers little strain rate and the lubricant still has enough strength to support the load

and make surfaces totally conformal. Solid materials are able to carry finite shear stress unlike liquids which have, theoretically speaking, infinite shear strength [13]. Under sliding motion, all the lubricant shear strength is likely “saturated” by the strain rate, no strength is left to prevent the oil from flowing out sideways from the asperity tops. The so-called “shear tinning” effect arises. This increases the risk that the asperity tops reach through the oil film above all in nominal condition close to mixed lubrication. Consequently, as soon as sliding motion is superimposed to rolling, classical distinction between the lubrication regimes according to the values of Λ may be invalid.

Precisely for the above reasons some authors believe that judgments based upon conventional values of Λ may be too simplistic and unreliable (see for example Cann et al. [35]).

4.5 TRACTION IN EHL CONTACTS

A distinction between the terms “friction” and “traction” should be made. *Friction* usually refers to detrimental effects causing the mechanical system to loss energy; in this regard it has a negative connotation. The term *traction* is referred to when frictional forces allow the transmission of mechanical energy rather than its dissipation. Two basic examples of traction are a wheel rolling on the road without skidding (dry condition) and the carryover effect between the impeller and the turbine of a hydraulic torque converter.

Traction usually appears in EHL contact. For example, recalling the operating principle of a pin-on-disk tribo-tester described in sec. 3.1, the friction force measured by the load cell is nothing but a traction force in the case of a lubricated tests. The presence of a relative motion between the static partner (i.e. the pin) and the rotating disk causes a drag effect which pushes the pin to move; this traction effect is eventually degraded to a friction effect as the pin is constrained by the measuring arm.

It is however common practice in the field of elastohydrodynamics to speak of traction instead of friction, whichever is the fate of mechanical energy. By reversing equation (3), the general traction force due to viscous shearing can be expressed as:

$$F_v = \int_{\Omega} \tau dA \quad (27)$$

From equation (37) it follows that the local value of the shear stress at each point within the contact should be known. The traction analysis in an EHL is thus very complicated. A suitable model for τ has to be invoked: usually it is taken from the number of non-Newtonian equation discussed in sec. 4.2.3 and should include temperature and pressure influence.

Let us consider a nominal point contact between a static ball and a moving plane. A way to simplify the integration is to consider the total force acting onto a plane into the lubricant film. A flat bidimensional dominion in the cartesian coordinates x and y can be thus considered for the integration. For example, Conry et a. [36] proposed a method in which the shear stress τ_m is calculated at the level of the midplane of the lubricant film resorting of a Ree-Eyring formula.

$$F_v = \int_{-\infty}^{+\infty} \int_{-\infty}^{+\infty} \tau_m dx dy \quad (28)$$

Being:

$$\sinh\left(\frac{\tau_m}{\tau_L}\right) = \frac{\eta(u_a - u_b)}{\tau_L h(x, y)} \frac{\left(\frac{h(x, y)}{2\tau_L} \frac{dp}{dx}\right)}{\sinh\left(\frac{h(x, y)}{2\tau_L} \frac{dp}{dx}\right)}$$

A coefficient of traction (CoT) can be defined according to the classical definition of friction coefficient of equation (33).

$$\mu_T = \frac{F_v}{F_N} \quad (29)$$

Stribeck curve is the plot of the steady-state value of the coefficient of traction against the Hersey non-dimensional number (however, the reader can find in the scientific literature Stribeck curves plotted against entrainment speed or hydrodynamic velocity parameter U or even the Λ ratio itself).

$$He = \frac{\eta\omega}{p} \quad (30)$$

Where: ω is the rotational speed [rps];
 p is a reference value of pressure [Pa] (e.g. the maximum Hertzian pressure);
 η is the absolute or dynamic viscosity (at atmospheric conditions) [Pa·s];

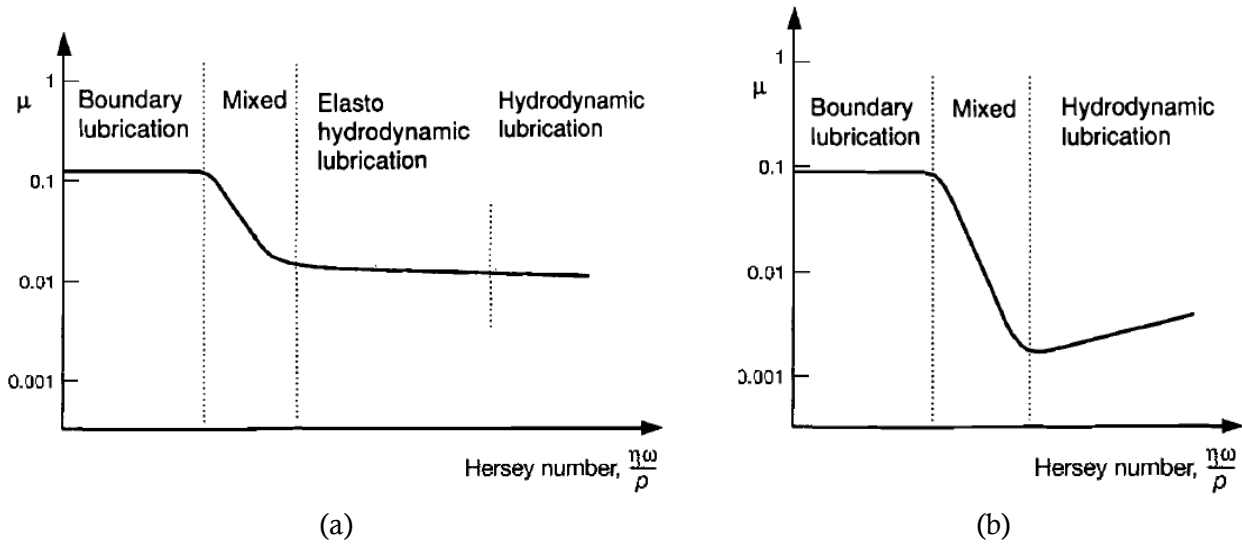


Figure 4.18. Typical shapes of the Stribeck curve for a non-conformal (left side) and conformal contact (right side).

Modified from:

S. Gonsel et al, *The Elastohydrodynamic Friction and Film Forming Properties of Lubricant Base Oils* [37]

Stribeck curve is a useful tool to display how friction changes in the different regimes presented in Sec. 4.4 and better understand the characteristic of each regime. Figure 4.18 shows two typical Stribeck curves with different trends in the region of high values of the Hersey number. It is a common occurrence that both in case of conformal contacts and of concentrated contacts, the lubricant adapts with a slight increase in viscosity and friction grows (Figure 4.18b). Sometimes, in non-conformal contact friction it remains broadly constant and eventually falls (not in the figure) at very high Hersey number due to frictional heating [37].

The experimental investigations report that the value of the CoT in a lubricated contact is influenced by the type of motion occurring at the interface. Figure 4.19 shows a schematic representation of CoF the trend plotted against the slide-to-roll ration.

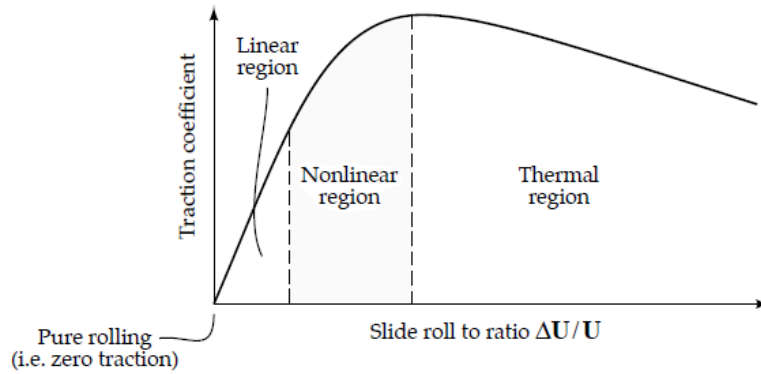


Figure 4.19. Typical traction curve of a lubricated contact

G.W. Stachowiak, A.W. Batchelor, *Engineering Tribology*, Butterworth-Heinemann, 2005

From Figure 4.19 it is clear that the traction characteristic is usually divided into three regions:

- the linear region;
- the nonlinear region;
- the thermal region.

The relationship between traction coefficient and slide-to-roll ratio is initially linear. This is the case of lightly stressed rolling contact. The linear relationship is soon lost, and the curve reaches a maximum value beyond which there is a gradual decline in the traction coefficient. The peak traction coefficient occurs in general at about 0.1 or 10% of slide to roll ratio. In the thermal region, viscous heating of the lubricant by intense shearing is the most significant influence ratio and CoF drop owing to the loss of viscosity.

Traction is influenced by glass transition as well as by film thickness. In terms of traction, the glass transition and the shear strength imply that the traction coefficient may reach a maximum value. It is possible that under increasing SRR the trend of the CoT is distorted by a horizontal cut of the curve, if an internal inviscid slip effect arises.

In classical elastohydrodynamic theory, film formation and friction are almost entirely decoupled in terms of key parameters [10]. The film thickness depends on the rheology of the lubricant at the inlet region where it behaves in a Newtonian fashion as shear stress is always sufficiently low. Atmospheric pressure viscosity, pressure-viscosity coefficient (α) and entrainment speed shape the rheological behaviour at the inlet region and control the quantity of oil entrained. By contrast, friction is almost independent from these parameters and it mainly involves the molecular structure of the lubricant, taking a lubricant-characteristic value between 0.02 and 0.1 for most oils [38]. In the central part of the contact, as it has already been said, the lubricant is a plastic solid and shear behaviour prevails (non-Newtonian behaviour cannot be overlooked). The limiting shear stress τ_L , which is the key parameter for friction, rises approximately proportionally with pressure and since $\mu = \tau_L/p$ the coefficient of friction has a limiting value (almost load independent) as well [37]. There are suggestions in literature that high α correlates with high limiting CoF: from this point of view an indirect correlation between thickness and friction does exist.

Moreover, as long as full-film lubrication is attained, friction is independent from speed in that τ_L is independent from speed. On the contrary, τ does depend on speed: whichever the behaviour of the lubricant (Newtonian or non-linear) is, τ is approximately proportional to $1/h$ [39] where h increases with speed. Keeping the speed parameter U^* constant, friction may also increase with increasing sliding speed (i.e. SRR) up to a given limit (as shown in Figure 4.19). In addition, if decreasing U^* causes collision among surface asperities, the lubrication regime changes and friction cannot have but an

upwards transition. However, EHL friction coefficient usually refers to full-film lubrication if not otherwise specified.

5 SETUP AND MATERIALS

The material pair for the tests in EHL conditions consisted of a 6mm ruby ball sliding over ultrathin microscope round cover slip made of D263M[®] by Schott AG, with a nominal thickness of 0.1 ± 0.02 mm. The main properties are shown in Table 5.1.

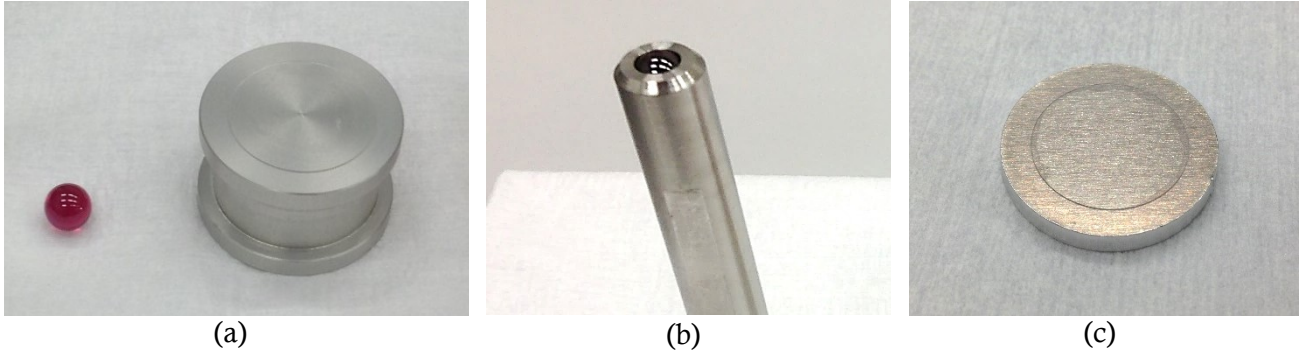


Figure 5.1. (a) Sample pair for tests; (b) Ruby ball fitted into the pin-shaped ball-holder; (c) Sample of the thin type

In a pin-on-disk tribometer the ball represents the static partner, which is mounted into a pin-shaped ball-holder (Figure 5.1b) where it is held in place by a screw clamping device. Being the sphere unable to roll, a pure sliding lubricated contact was there during the interaction. Tests run with a slide-to-roll ration (SRR) always equal to two:

$$SRR = 2 \cdot \frac{u_d - u_b}{u_d + u_b} = 2 \quad (31)$$

Where: u_d is the disk linear speed;
 u_b is the sphere linear speed (equal to zero for pin-on-disc set-up).

The disk is the moving element, the one driven by the spindle. In the present case, such a thin glass slip cannot be installed directly into the spindle clamping device as it is too fragile. To overcome this critical issue, the cover slip was glued on the top of a cylindrical aluminium sample-holder, (Figure 5.1a) fit for being secured on the spindle. The gluing process was handcrafted using a cyanoacrylate fast-setting glue.

Table 5.1. Properties of mating materials

	Material	Density [g/cm ³]	Young modulus [GPa]	R _q Roughness [μm]	Diameter [mm]
Ball	Synthetic ruby	3.98	390	0.013	6
Microscope slip	D263M [®] glass (Schott AG)	2.51	73	0.005	18

The same testing methodology has been tried out in two separate operating conditions (in terms of F_T and N at the contact) so that the assessment on the performance of the machines could encompass a larger share of their working range. Two types of commercial liquid lubricants were employed³: a middle-viscosity and a high viscosity oil (herein referred to as MVo and HVo) whose main properties at the testing temperature are listed in Table 5.2. The former was used for application with little tangential force due to its limited traction and load supporting capability, the latter for higher tangential forces. Both oils are thermally stable and characterised by a relatively high *viscosity index* (VI).

³ The commercial names of these lubricating oils are considered as a business confidential information.

Table 5.2. Properties of the liquid lubricants.

	Base stocks	Specific gravity [kg/dm ³]	Viscosity [cSt] @ 30°C	Pressure-viscosity coefficient ⁴ [GPa ⁻¹]	VI ⁽⁵⁾
Middle Viscosity oil (MVo)	<i>Confidential</i>	0.861	122.2	30.5	101
High Viscosity oil (HVo)	Poly(1-decene), Polybutene	0.839	740.3	34.8	123

Table 5.3 provides an overview on the testing conditions investigated in this study and related parameters. Even if ASTM G99 standards only apply for one-way rotating tests, the investigation comprises some sets of linear reciprocating tests too. The same experimental set-up served for both test configurations. Figure 5.2 displays two models of sample-holders: the ticker one was preferably used for single-way rotating test, the thinner one for linear reciprocating tests. Anyway, it was merely a choice of experimental convenience and comparative tests ensured that both layouts gave consistent friction results.

Differently from the most widely used experimental techniques for EHL, no lubricant bath was there. A very little amount of lubricant was added on the top of the sample before starting each test, in order to completely cover the zone where the interaction between solid surfaces took place (Figure 5.2). Figure 5.2 is a zoomed view of the lubricated contact just before running a one-way rotating test.

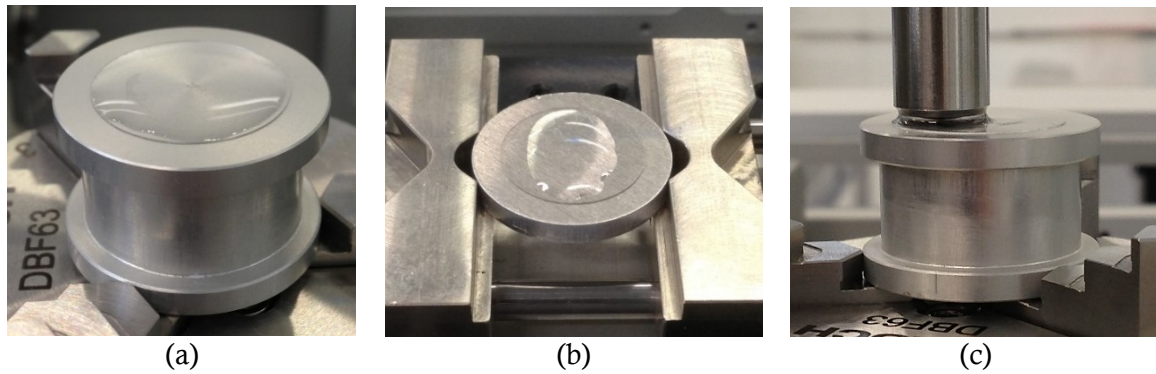


Figure 5.2. Amount oil on the glass surface before each (a) rotating tests and (b) linear reciprocating tests; (c) zoomed view of the lubricated contact

Tests were performed with the 3 different Anton Paar tribometers described in Sec.3, alternately equipped with either a rotating module (conforming to ASTM G99-05 standard) or a linear module (conforming to ASTM G133 standard). The load and spindle speed were kept constant at 2N - 100rpm during tests with the MVo and 30N - 150rpm with the HVo. Minor changes in the entrainment speed were accepted and several track radii were sequentially set in the range from 4 to 7mm with the MVo and from 5 to 6mm with the HVo. Every condition was validated with many repetitions.

Table 5.3. Testing conditions parameters

	Load [N]	Spindle Speed [rpm]	Duration [cycles]	Track radius [mm]	Stroke Amplitude [mm]	Average Temperature [°C]	Humidity [%]	Lubricant quantity [μL]
MVo (rotating)	2	100	1000	4 to 7	-	29	30 to 95	50
MVo (linear)	2	60 (1Hz)	500	-	6	29	30 to 95	30
HVo (rotating)	30	150	1000	5 to 6	-	28-29	20 to 30	80

⁴ Pressure-viscosity characteristics are calculated with So and Klaus' analytical model.

⁵ Reference is made to the ASTM D2270 standard.

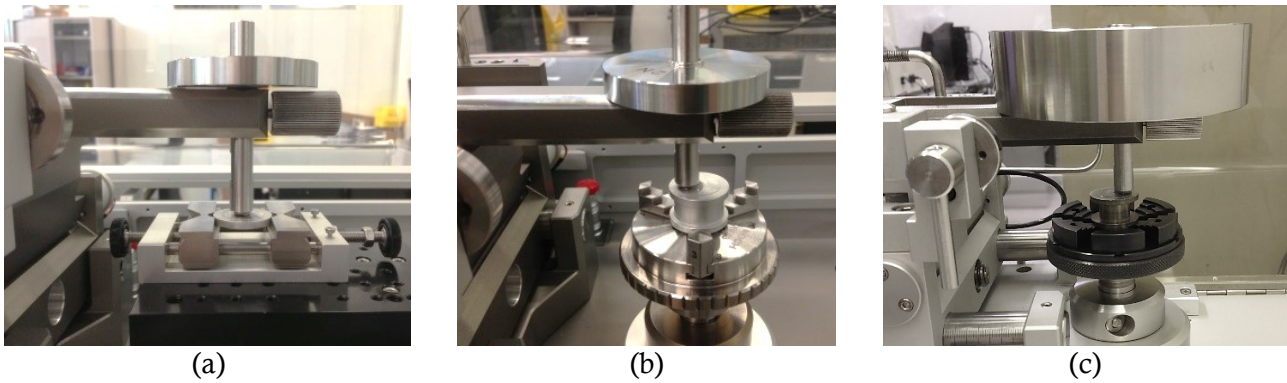


Figure 5.3. Test setup for different conditions (a) 2N load - linear test; (b) 2N load – rotating test; (c) 30N load – rotating tests

A temperature and humidity sensor were fitted inside the testing chamber to follow the evolution of the environmental parameters, as displayed in Figure 5.4. The control of the test rig and the experimental data acquisition were both performed with the dedicated Anton Paar InstrumX® Software.

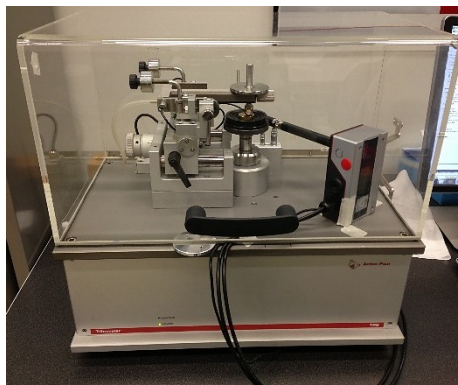


Figure 5.4. Temperature and humidity sensor installed into the measuring chamber

A great deal of attention was paid to avoid any kind of chemical and physical contamination of the lubricants and the samples surfaces which could alter friction results. Latex gloves were worn before handling samples and every other tool. The entire equipment was constantly cleaned and degreased with chemical pure Acetone and Isopropyl alcohol (IPA) and wiped with lint-free tissues only. Optical microscopy allowed to check the integrity of the glass surface, the absence of wear on the ball and the effective removal of any trace of used lubricant before the following repetition was run (see Figure 5.5c).

A specific cleaning procedure of testing materials was developed to enhance the repeatability of the surface condition before each test:

1. Absorb the excess of oil on the sample and the ball / ball holder with the help of a paper napkin.
2. Wash the ruby ball, the ball holder and the sample surface with acetone in order to remove any trace of oil and fat. If necessary, soak and rinse several times these parts with a flask filled with acetone to completely remove oil and fat traces. Dry in a fresh zone of a napkin or tissue.
3. Rinse the surfaces with isopropanol just before starting the test to wash away dust and fibres coming from tissues and the air.
4. Wipe the surfaces with a fresh lint-free tissue wet with isopropanol. Wipe the sample surface in a single direction, from one side of the glass to the other, in order to trap the particles in the tissue. Wipe the groove between the ruby ball and the ball holder opening by performing a circular continuous motion.

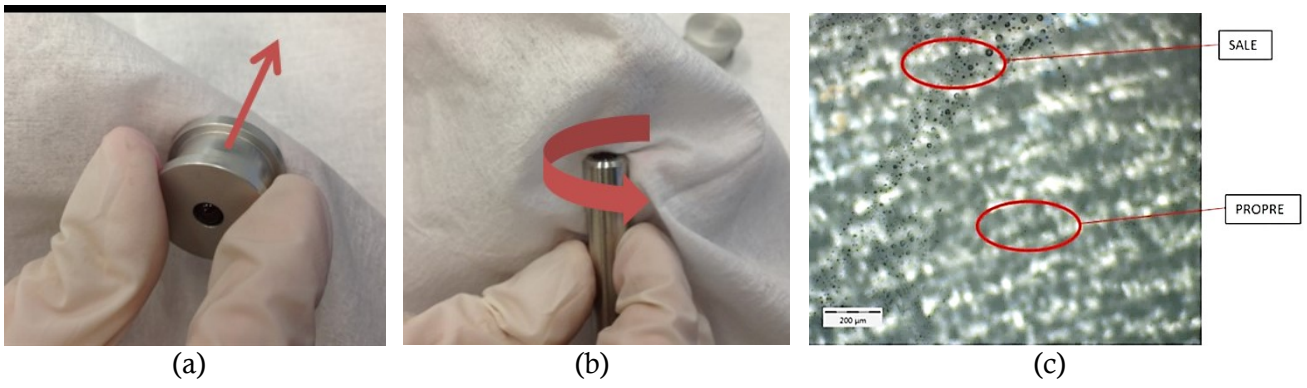


Figure 5.5. (a) and (b) thorough wiping the sample pair surfaces; (c) microscopic observation of the glass surface where clean and dirty zone are clearly visible

5. Verify under the microscope the condition of the surfaces: neither oil drops and fibres, nor scratches/damages should be visible.

6 EXPERIMENTAL RESULTS

6.1 PRELIMINARY RESULTS

First, preliminary tests have been carried out to identify the most favourable testing parameters. With regard to rotating tests, loads of 1N and 2N have been tried out at 100rpm with the MVo and loads of 30, 40 and 50N coupled with speeds from 100rpm to 200rpm have been tested with the HVo.

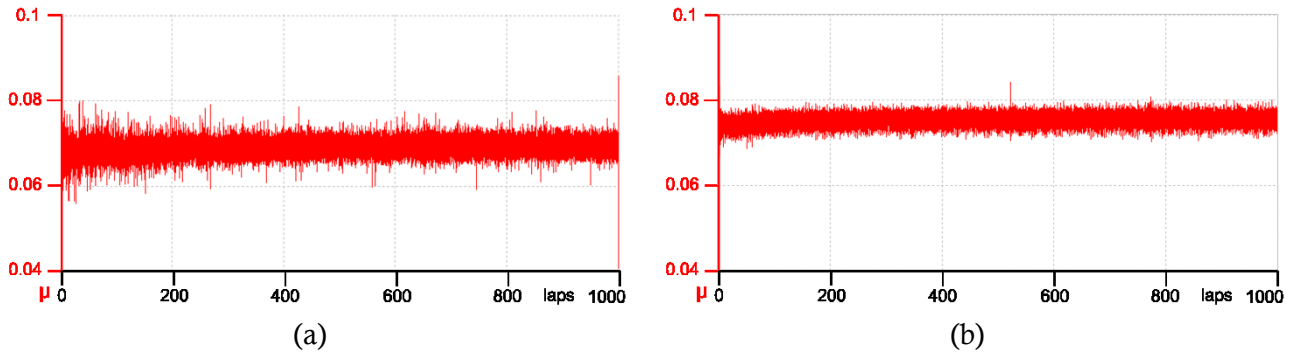


Figure 6.1. Coefficient of friction with 1N load (on the left) and 2N load (on the right) performed with the MVo.

The preliminary results with MVo showed that 1N and 2N tests yield similar friction results in terms of mean value, but with a more regular curve in the case of 2N load (see Figure 6.1). This behaviour was not furthermore investigated; however, it could be linked to microscopic fluctuations in the oil thickness due to the very low applied load.

As to HVo, the authors' original intention was to use this oil quality to apply a load as close as possible to the maximum normal load allowed by the machine specifications. Despite the initial wish, neither 50N nor 40N granted a complete separation between solid surfaces and the system systematically ran into failure with the glass disk breakup. On the contrary, 30N tests yielded the necessary repeatability of stable results to provide a reference condition.

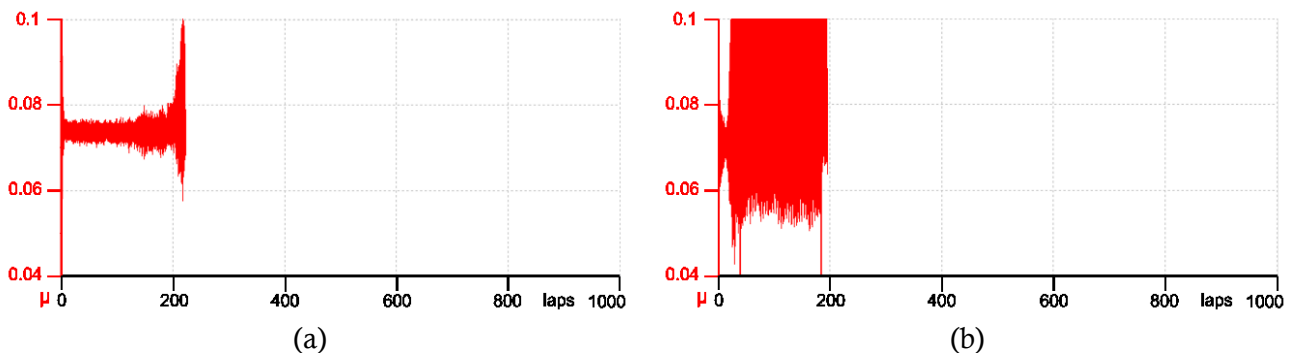


Figure 6.2: Typical friction curve with the HVo and 40N load (early stop of the test) performed on a TRB

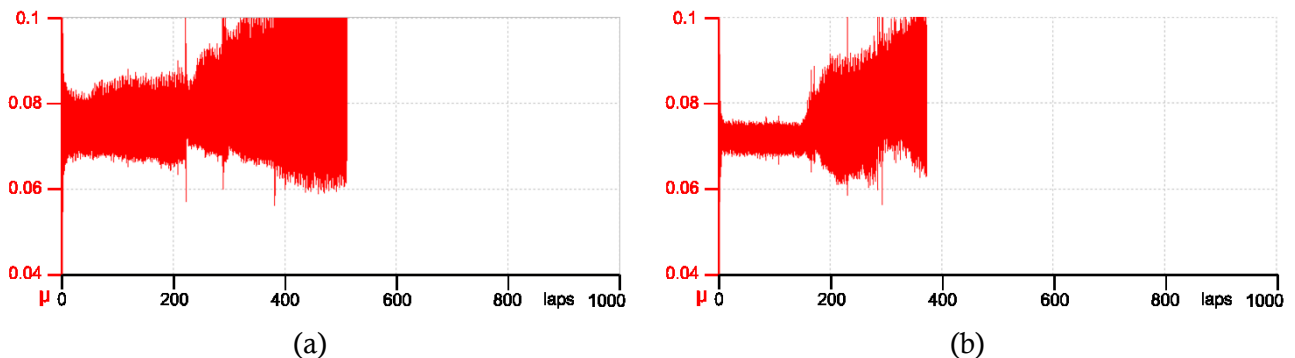


Figure 6.3: An example of friction curve with a) 40N load, b) 50 N load, each one disclosing an early stop of the test. Tests were performed with the HVo on a TRB.

For linear reciprocating tests with the MVo, the load was kept at the same value of 2N identified during the corresponding rotating tests, whereas the linear oscillation frequency of the sliding table was varied in the preliminary phase. Frequency of 3Hz, 2Hz and 1Hz were tested. Figure 6.4 shows the comparison among the extreme values: 1Hz (Figure 6.4b) is the one that gives rise to the best cycle shape (at equal sampling rate, always fixed at 80Hz). To allow for comparison with rotating test results, data from linear tests were analysed real time thanks to a cycle-resolved averaging technique in which only the points of measure placed within the central portion of each cycle were taken into account. The area framed by a blue square in the left side of Figure 6.4 marks out those points participating in the average, about 3/5 of a cycle. In the central part of the stroke the hydrodynamic effect is indeed maximum, and the variations of speed is minimum around its upper value. In the right side of Figure 6.4 the rough friction curve is displayed as it is measured during the test (the dashed square marks the cycle which us represented in the left side of the same figure).

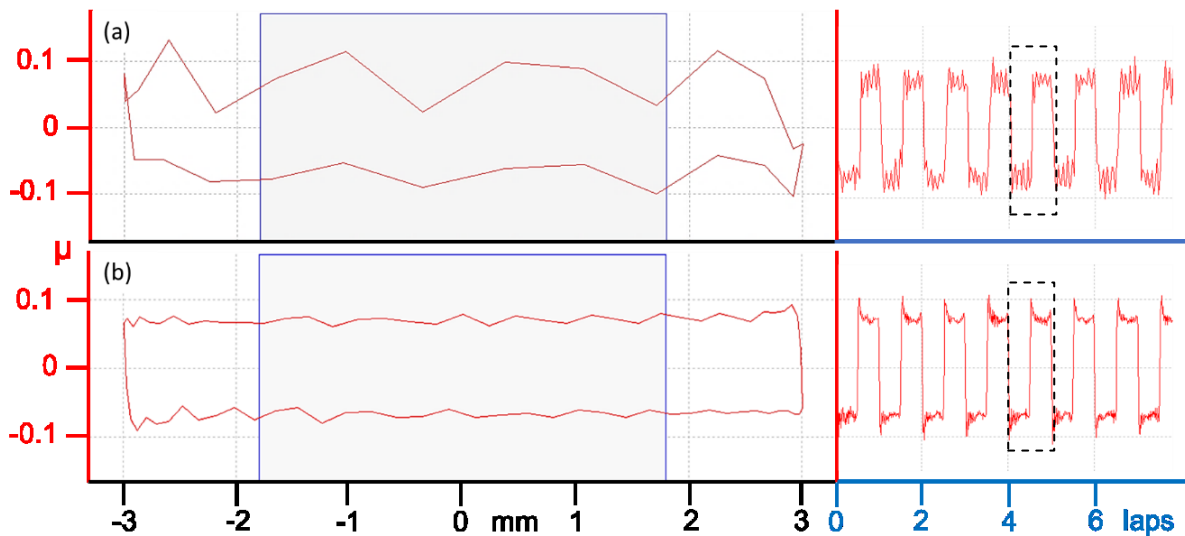


Figure 6.4. On the left: typical cycle shape with a) 3Hz, b) 1Hz reciprocating motion. On the right: rough friction curve.

6.2 RESULTS OF THE INVESTIGATION

Several repetitions of the two testing conditions have been carried out: each set covers at least 27 repetitions, and many more in most of the cases. Two average tangential force levels were obtained: 0.145N for tests with the MVo and 2.139N for tests with the HVo. Each test has been accounted for two statistical parameters automatically calculated by InstrumX[®] software: the test average and the standard deviation of the measured coefficient of friction. The overall statistics has been compiled by collecting these summary data from each test to calculate three main quantities:

- The mean of the average values (referred to as *MAV*);
- The standard deviation of the average values (referred to as *St.DAV*);
- The mean of the standard deviation values (referred to as *MSt.DV*).

Table 6.1 gives an overview of the results corresponding to the conditions listed in Table 5.3. Section “Discussion” will return to these statistic quantities to reveal the tribometer-to-tribometer variability and test-to-test variability.

Figure 6.5 to Figure 6.15 are a collection of show a typical friction curves. Each figure represents the friction curve corresponding to one of the tests (which is taken as an example) from each set of repetitions listed in Table 6.1. It is here recalled that data coming from linear reciprocating tests were previously analysed through a cycle-resolved averaging technique. The curves in and are very different from the others because do not represent rough data.

Table 6.1 Summary of the results for the two reference testing conditions

Machine	Oil type	Number of samples	Total number of repetitions	Valid tests	MAV	St.DAV	MSt.DV	Laboratory
TRB ³	MVo (rotating)	3	64	46	0.0757	0.0014	0.0017	Anton Paar TriTec, Peseux (SW)
	MVo (linear)	1	40	32	0.0702	0.0016	0.0003	
TRB	MVo (rotating)	2	50	40	0.0743	0.0015	0.0138	Anton Paar TriTec, Peseux (SW)
	MVo (linear)	1	27	24	0.0711	0.0008	0.0005	
TRB	MVo (rotating)	1	42	38	0.0731	0.0022	0.0035	Politecnico di Torino, Torino (IT)
	HVo (rotating)	3	42	42	0.0713	0.0011	0.0027	

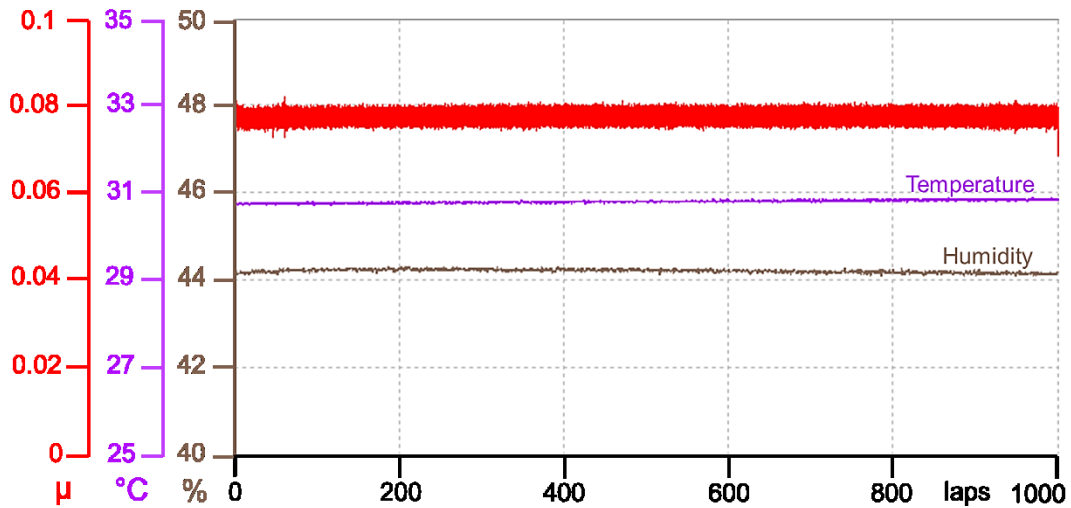


Figure 6.5. TRB³, MVo, 2N load, 100rpm, rotating tests. Typical friction curve

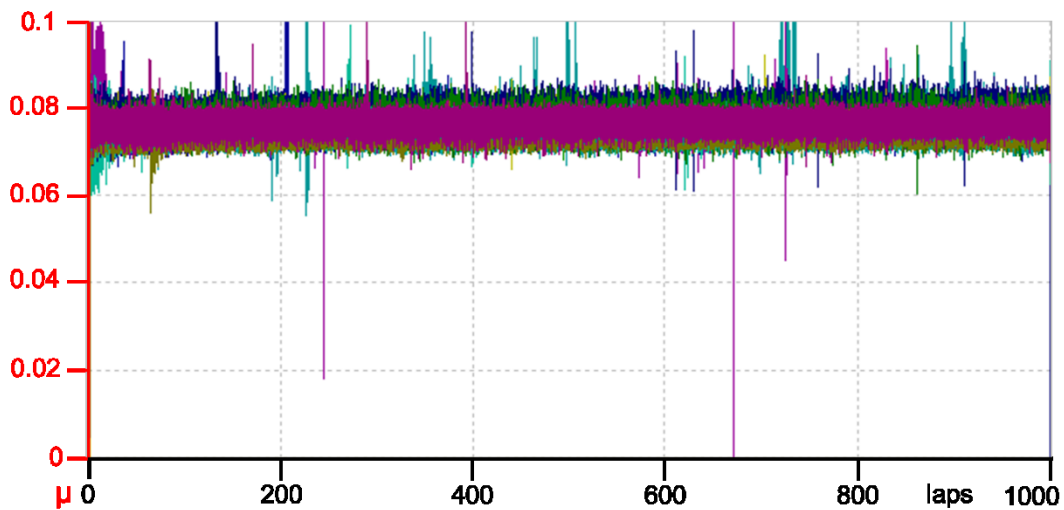


Figure 6.6: TRB³, MVo, 2N load, 100rpm, rotating test. Typical friction curve and overview of all the results

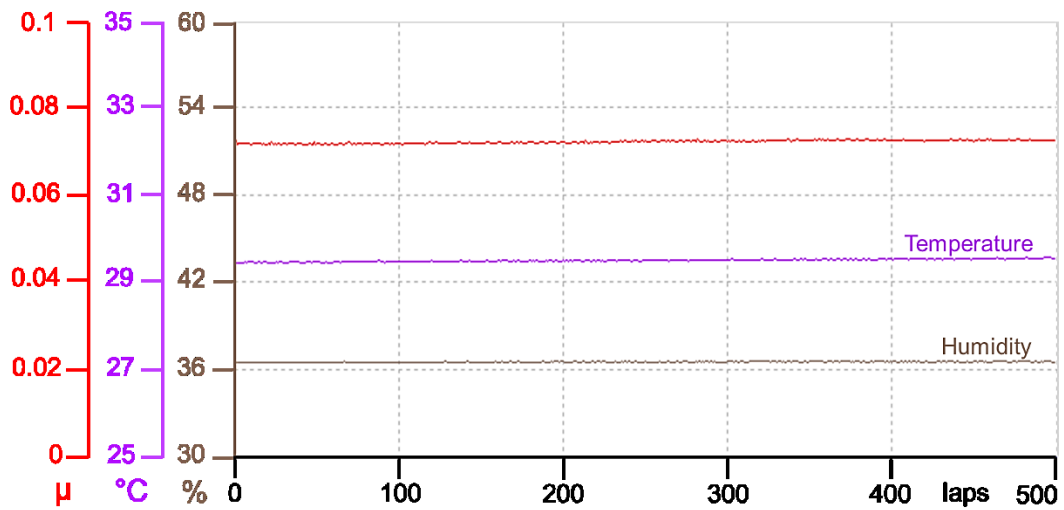


Figure 6.7. TRB³, MVo, 2N load, 100rpm, linear reciprocating. Typical friction curve

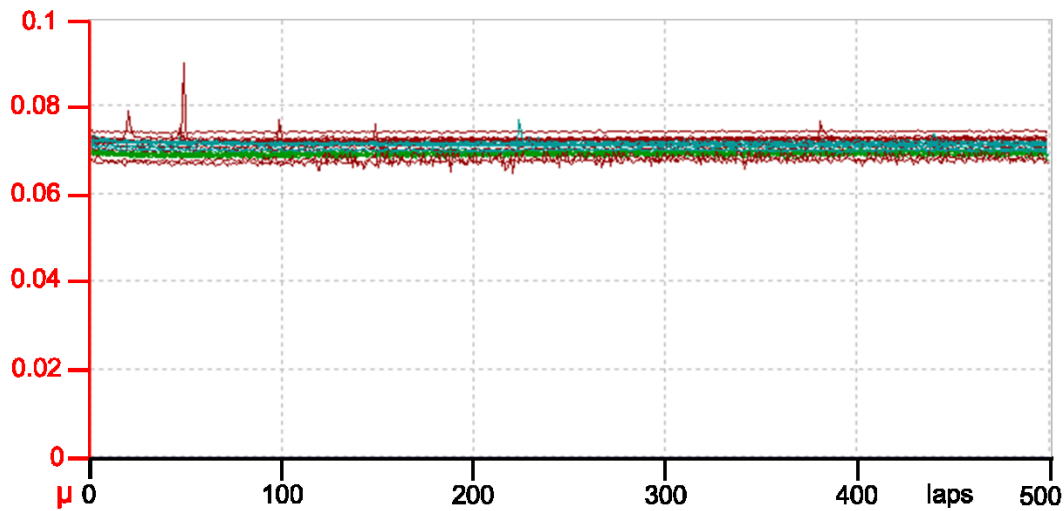


Figure 6.8 TRB³, MVo, 2N load, 100rpm, linear reciprocating. Typical friction curve and overview of all the results

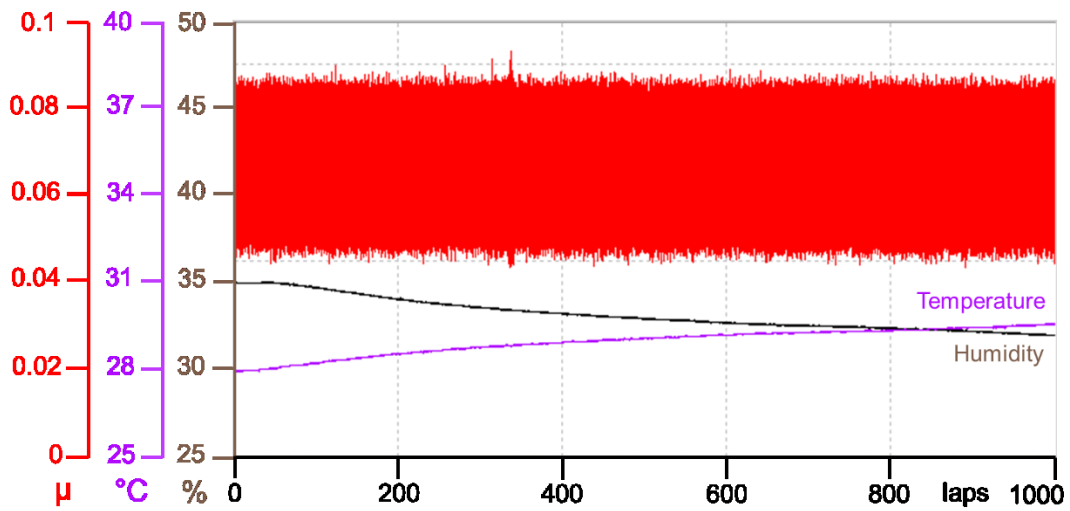


Figure 6.9. TRB, MVo, 2N load, 100rpm, rotating test. Typical friction curve

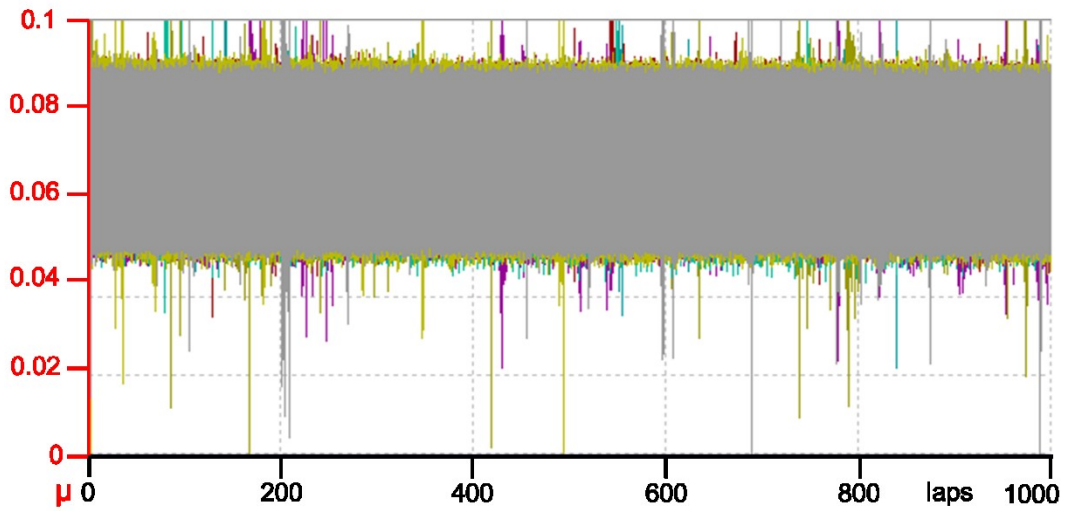


Figure 6.10 TRB, MVo, 2N load, 100rpm, rotating test. Typical friction curve and overview of all the results

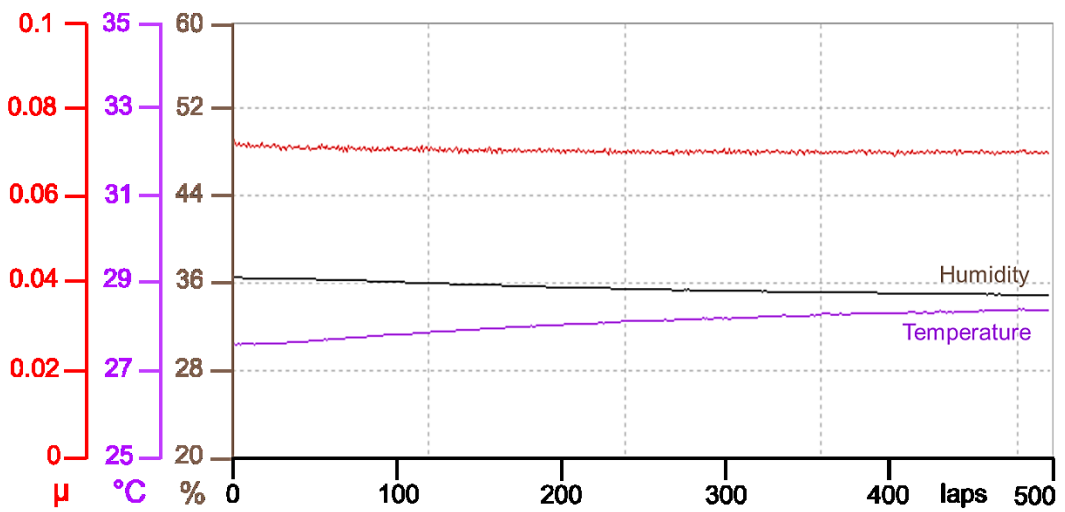


Figure 6.11. TRB, MVo, 2N load, 100rpm, linear reciprocating. Typical friction curve

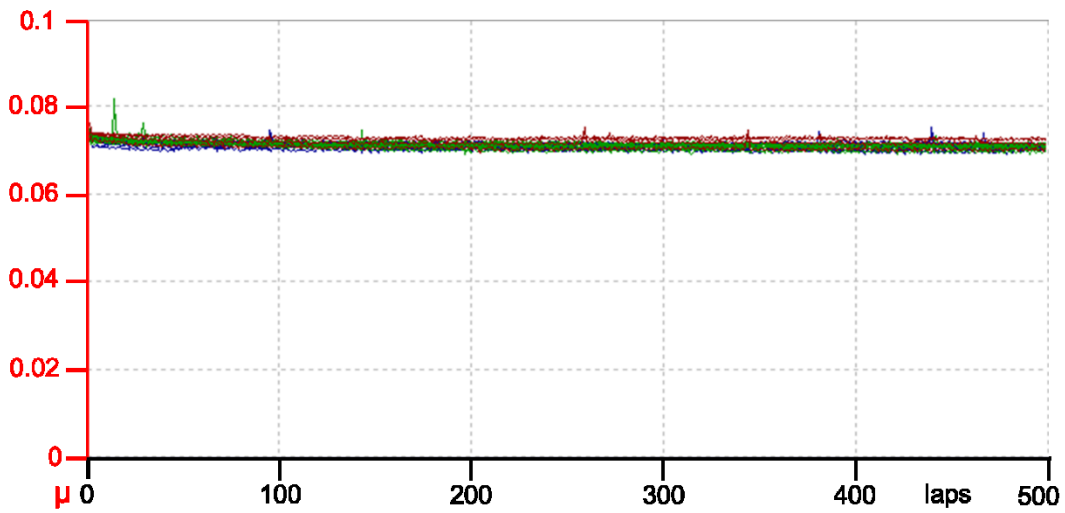


Figure 6.12 TRB, MVo, 2N load, 100rpm, linear reciprocating. Typical friction curve and overview of all the results

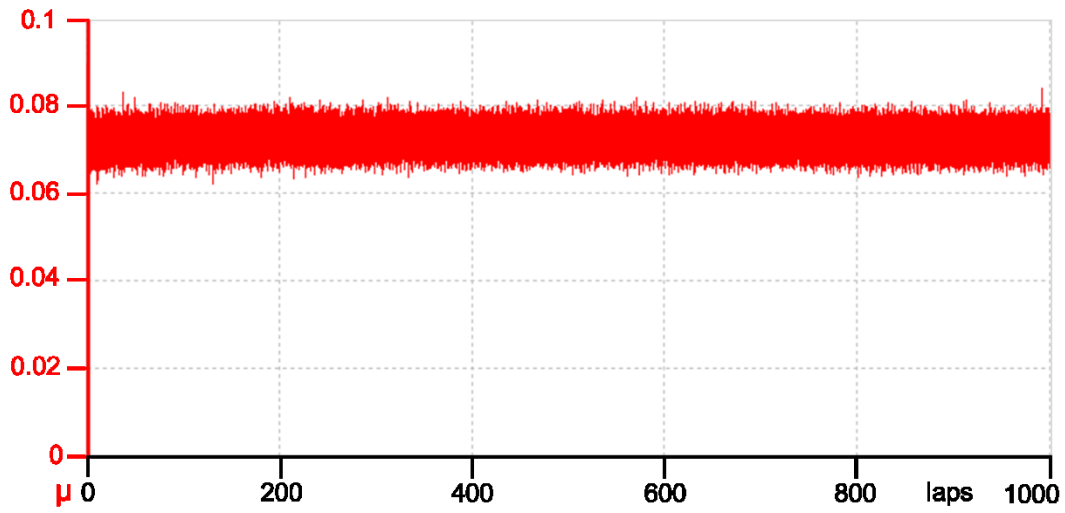


Figure 6.13. TRB, MVo, 2N load, 100rpm, rotating tests (PoliTo). Typical friction curve

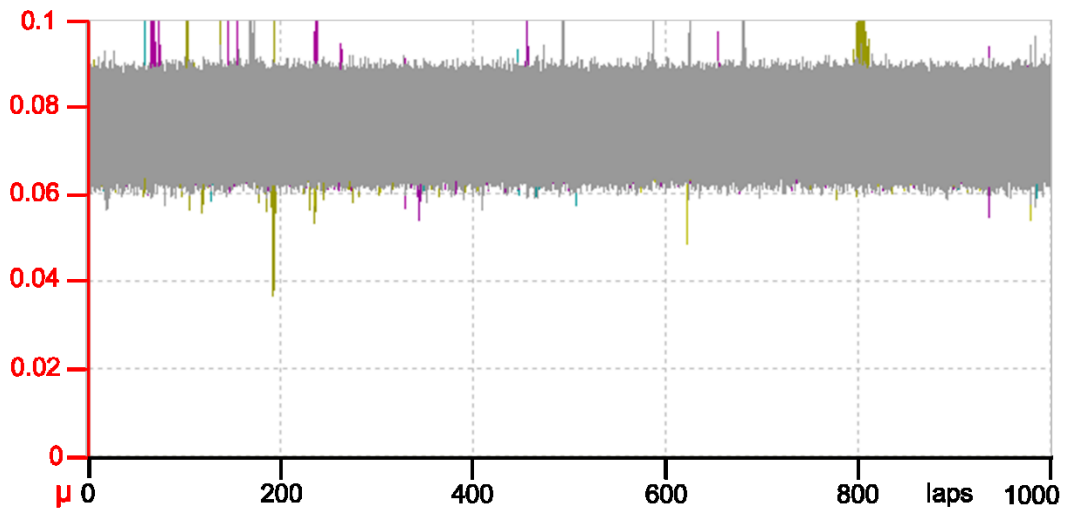


Figure 6.14 TRB, MVo, 2N load, 100rpm, rotating tests (PoliTo). Typical friction curve and overview of all the results

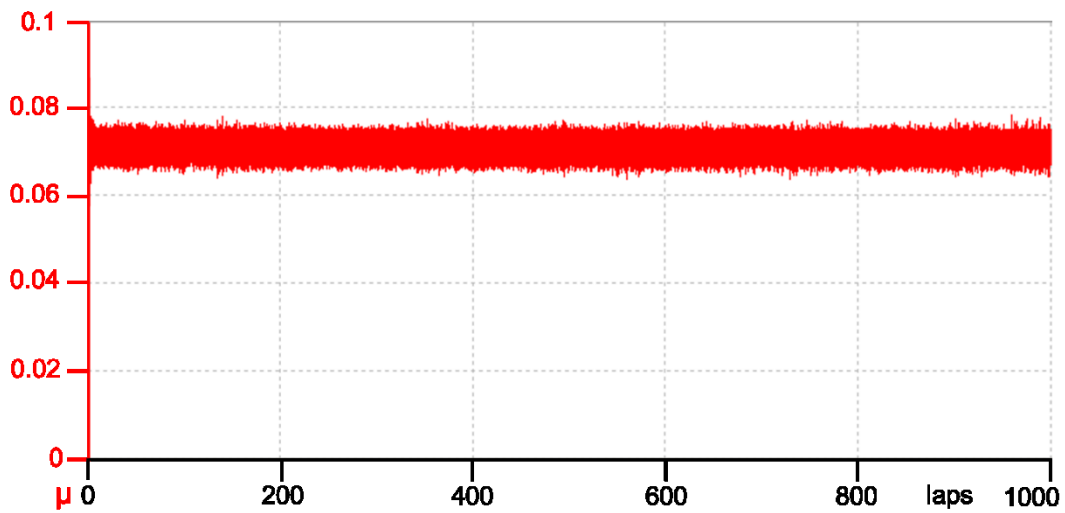


Figure 6.15. TRB³, HVo, 30N load, 150rpm, rotating test (PoliTo). Typical friction curve

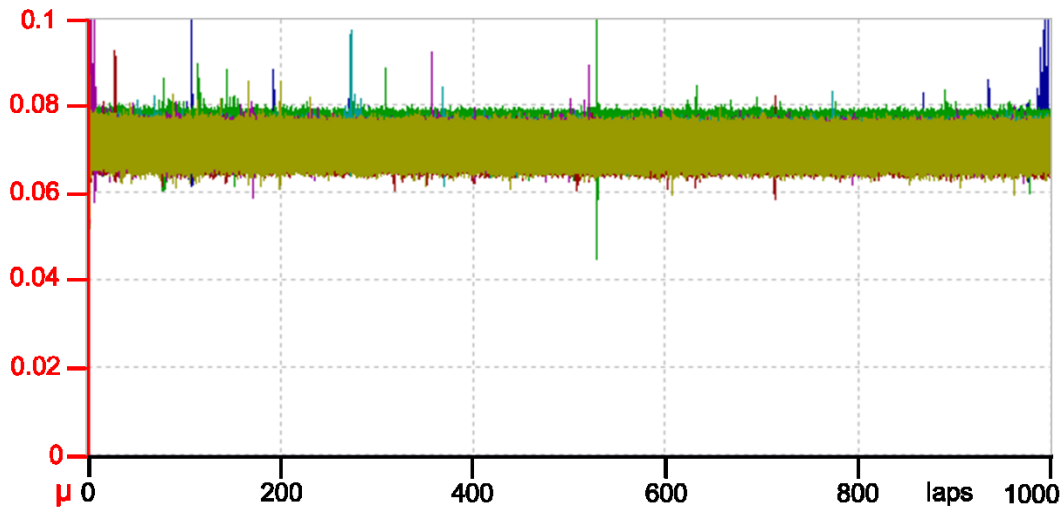


Figure 6.16 TRB, HVo, 30N load, 150rpm, rotating test (PoliTo). Typical friction curve and overview of all the results

In Table 5.3 the number of “valid tests” for each set is listed side by side with the total number of repetitions. It represents the subset actually contributing to the statistical quantities MAV, St.DAV, MSt.DV. Such a “discrimination” of data was necessary as during tests it ran the authors to recognise some external disturbances affecting the results. EHL friction tests appeared to be very sensitive to shocks and vibrations coming from the environment, even at very low intensity. Example of external disturbances are people walking by the machine, noise and vibrations coming from rooms nearby, accidental hits on the table, etc... The effect of these external disturbances is clearly visible in Figure 6.17. Under such circumstances the test average value remains practically unaltered, but the standard deviation is much higher. Therefore, the test is unrepresentative of the physics at the contact zone and it must be rejected.

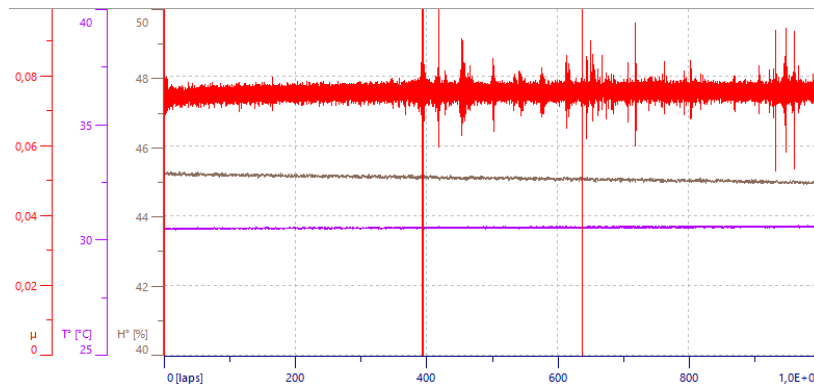


Figure 6.17: Stable curve altered by (people walking by the machine, noise and vibrations coming from rooms nearby, accidental hits on the table).

The cleanliness of the surfaces played an important role too. While carrying out the first sets of repetitions, it happened that some of them produced very unstable experimental curves, whose mean value and noise were very different from the usual ones. This kind of erratic behaviour was followed by no traces of wear on both the disk and the ball and could disappear in case measurements were stopped and then resumed in the same position or in another one. That inexplicable and seemingly random circumstance was first observed, then tentatively reproduced in order to find out the source. Figure 6.18 compares an example of an accidental event (Figure 6.18a) with a test in which the lubricant was intentionally polluted with dust, fibres (coming from the cleaning tissues) or diluents (Figure 6.18b).

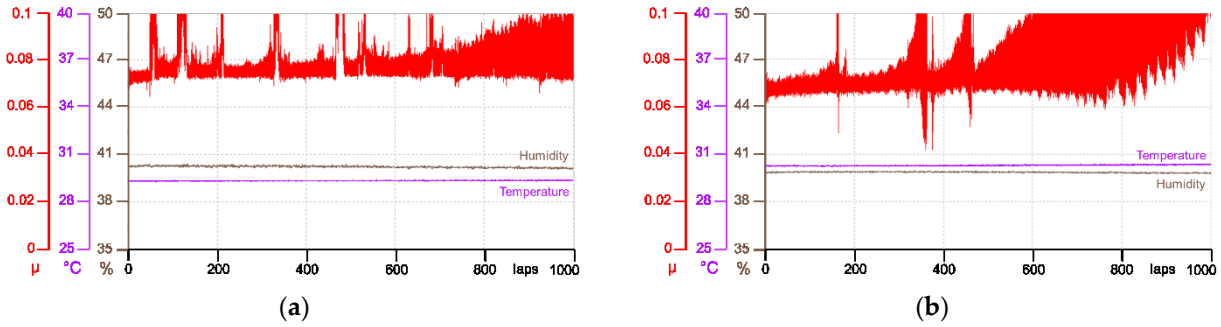


Figure 6.18. Comparison between an accidental event related to dirt (on the left) and an induced one (at right).

It was quite clear that imperfect cleaning of the surfaces or imperfect removal of used oil from the previous test negatively influenced the results and might deeply changes what normally happens. Then, great deal of attention has been devoted to the equipment clean-up and in case a reference condition of this kind will be proposed in future as a standard, a rigorous procedure for the preparation of tests must be included.

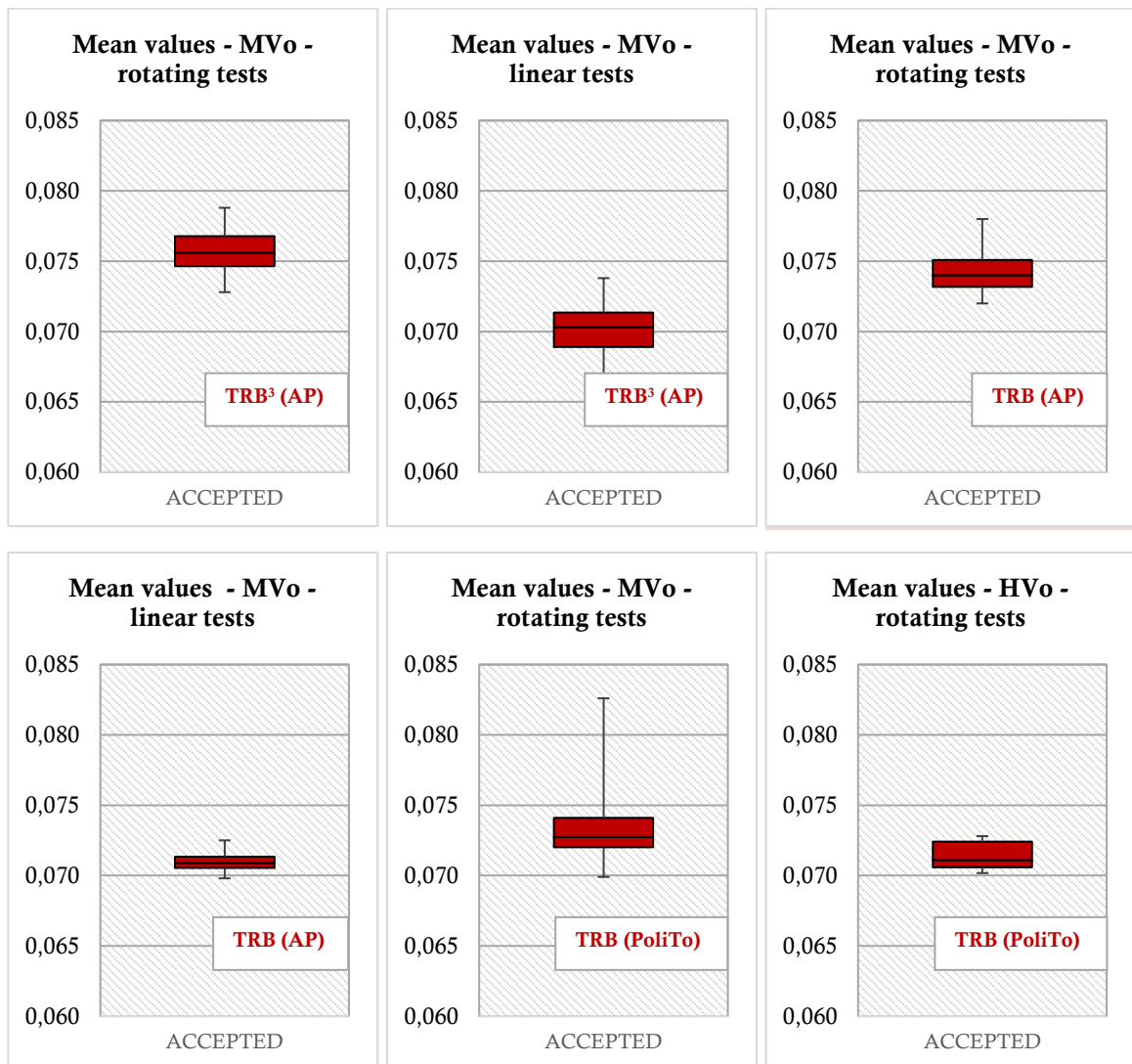


Figure 6.19. Box-plots of the accepted mean values for each set of repetitions.

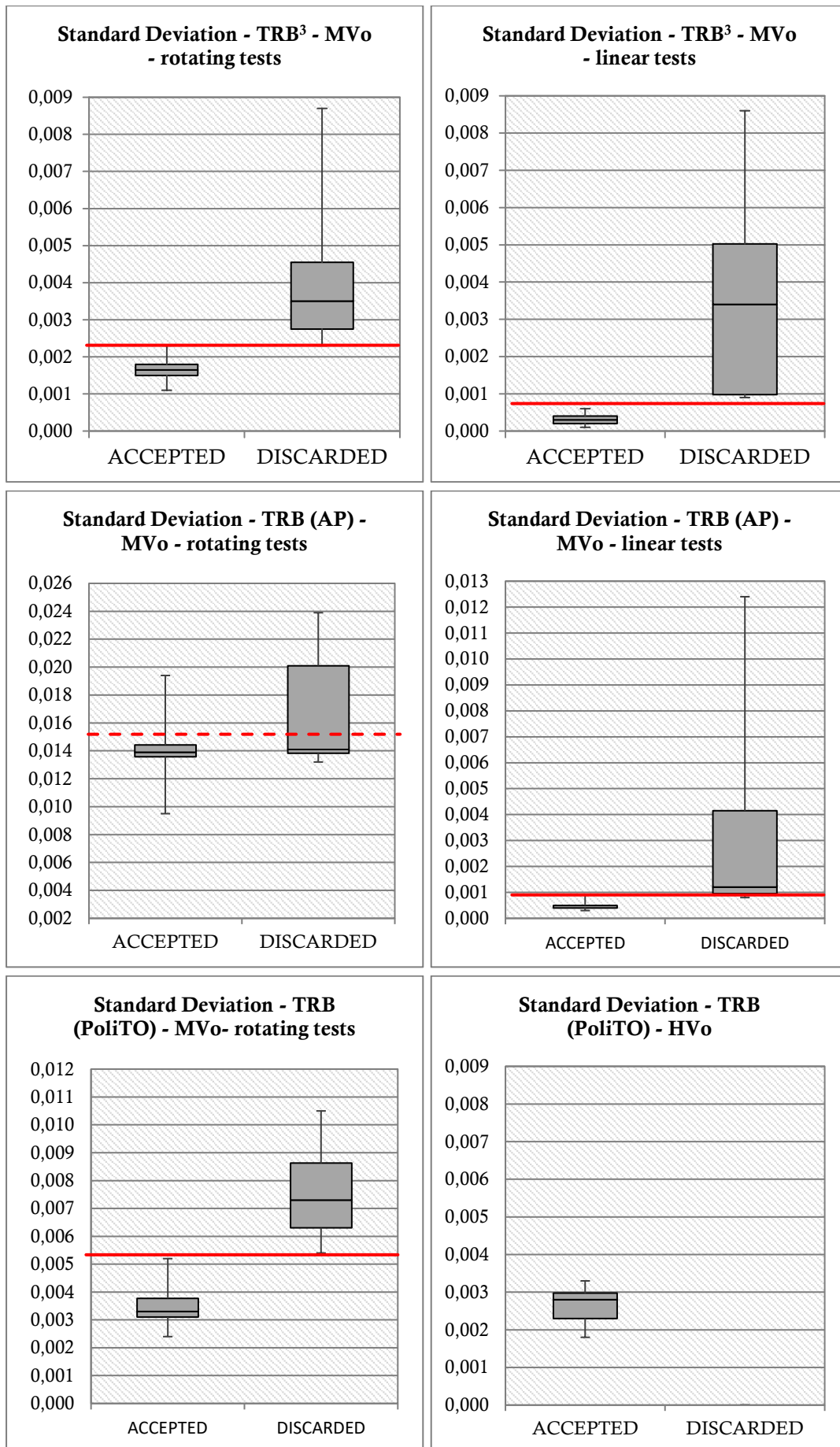


Figure 6.20. Box-plots of the standard deviation values.

The ASTM G99 standard recommends using all data from each set of measurements, including outliers. The authors of this paper would like to underline that the approach taken in this investigation is not in contrast with this guideline, despite the appearances. Outliers are values that deviate from the average “by accident”, i.e. linked to unavoidable accidental errors associated to the phenomenon under study. In this study, discarded tests are the result of systematic and well identified external causes (from anyway impossible to totally overcome). From this perspective, the discarded results are not even attributable to the phenomenon under study, so they are neither outliers.

The box-plots of Figure 6.19 show the scattering of the mean values within each set of repetitions presented in Table 3. By means of box plot portrayal, a comparison is also made in Figure 6.20 between the scattering of the standard deviation values of valid repetitions and the rejected ones. The painted areas in Figure 12 and 13 represent the 2nd and 3rd quartile of each set, i.e. the two ranges of values (straddling the median that is represented with the inner black line) including the 25% of the measures of the statistical sample each. Thanks to this comparison, you can be aware that the, so to speak, “aesthetic” criterium of rejection of tests first applied finds wide support in the ex-post statistical analysis. In most cases it is possible to determine a clipping value (highlighted by a red line in the diagrams): it constitutes the upper-bound of the values of standard deviation associated with accepted tests, while the values associated to the rejected results lie above the clipping value. For tests with the HV0 it is not possible to identify a clipping value as all tests were accepted and no strange results came out. For the sake of further verification, once the reasons for discarding a test are known, invalid test conditions could be intentionally sought to put to the test the validity of the clipping value. Anyway, this approach was followed here.

7 DISCUSSION OF THE RESULTS

7.1 STATISTICAL ANALYSIS OF THE RESULTS

Two types of variability of the results within each set of repetitions will be discussed below: tribometer-to-tribometer variability and test-to-test variability.

Details on the tribometer-to-tribometer variability of the CoF mean value can be deduced comparing the MAVs from each condition carried out on different test rigs. For rotating tests with the MVo the overall average is in the range of 0.0730 to 0.0760 with a maximum difference of 3.5%. For linear tests (with the MVo as well) the range is 0.0700 to 0.0715 and the maximum difference is 1.3%. For tests with the HVo the value is around 0.0715, but no comparative data are available yet as only one tribometer was used.

St.DAVs have to be taken into account to evaluate the test-to-test variability of the CoF mean value measured by the same tribometer. Values of St.DAVs ranging from 1.12% to 3% of the corresponding MAVs point out that scattering within each set of repetitions with any lubricant is minimal, even when more than one sample is used. Much of this scattering can therefore correlate with a change in position of the two counterweights necessary to equilibrate the arm own weight. A different position of the counterweights means a slightly different effective load applied on the contact. Since μ is so low, even minimal variations are found to affect somewhat the test mean value.

It becomes clear that each test condition owns “a characteristic value” of the coefficient of friction which is little affected by both the machine used to run the test and the sample. However, many more repetitions on several machines are necessary in the future to understand to what extent these values could further change.

A completely different scenario appears when comparing the MSt.DVs which are measures of the average noise of the friction curves. A similar noise (i.e. similar thickness of the curve itself) characterizes the curves measured in the same test condition on the same test rig. Conversely, a high tribometer-to-tribometer variability of the noise is obtained whenever the same test condition is repeated on different machines. Higher noise was experienced on TRB with respect to TRB3 at Anton Paar Laboratory. This difference was firstly attributed to the presence of a cooling fan installed into the electronic compartment of the TRB which lacks into the new TRB3 due to an improved thermal design. A baseline vibration was clearly perceptible indeed by touching the external frame of the machine. On contrary, a TRB of the same kind yielded curves with lower noise at Politecnico di Torino Laboratory, despite a similar baseline vibration present. It means that the scattering of the measured friction is more likely a machine characteristic feature, depending on either the machine fixture (i.e. the table) or the propensity of the structure to allow vibrations to spread out.

Linear tests have a MSt.DV that is one order of magnitude smaller than the corresponding value of rotating tests with the same oil. Such a discrepancy is nevertheless more apparent than real: curves of linear tests are not considered as-is, but after a cycle-by-cycle averaging technique in a manner which makes them comparable to the others. In a way, their MSt.DV suffers double averaging.

7.2 EHL CONTACT CONDITION ANALYSIS

This section has been introduced according to the will to avoid a “too empirical” approach which would have precluded some anomalous behaviours observed during experiments from being justified anyhow. These strange results have been already addressed in sec. 6.1.

Film thicknesses and the corresponding values of the roughness factor Λ are computed in Table 7.1 for every condition listed in Table 5.3. The table compares the classical analytical equations and one model developed for the EHD sliding contacts by Wilson and Shew. Strictly speaking, indeed, classical

analytical equations were developed for pure rolling contacts. Non-dimensional parameters U^* , W^* and G^* are computed according the equation presented in Sec.4.3 and C is the thermal-sliding factor introduced by Wilson and Shew [40] which takes into account the inlet shear heating effect.

Table 7.1. Analytical prediction of film thickness according to available

Equation	Oil Type	U^*	W^*	G^*	C	$p_{Hz} \text{ (max)}$ [GPa]	Calculated h_{min} [nm]	Λ
Hamrock and Dowson [41]							17.6	1.03
Piezoviscous-elastic [42]	MVo - rotating	$1.72 \cdot 10^{-11}$	$6.92 \cdot 10^{-6}$	$3.91 \cdot 10^3$	0.923	0.562	17.3	1.01
Wilson and Shew [40]							10.7	0.62
Hamrock and Dowson [41]							68.0	3.96
Piezoviscous-elastic [42]	HVo	$1.27 \cdot 10^{-10}$	$1.04 \cdot 10^{-4}$	$4.47 \cdot 10^3$	0.777	1.386	66.2	3.86
Wilson and Shew [40]							39.1	2.28
Hamrock and Dowson [41]							7.8	0.45
Piezoviscous-elastic [42]	MVo - linear	$5.12 \cdot 10^{-12}$	$6.92 \cdot 10^{-6}$	$3.91 \cdot 10^3$	0.958	0.562	7.6	0.45
Wilson and Shew [40]							5.0	0.29

Table 7.1 shows that the thickness of the lubricating film foreseen by the inlet shear heating model is approximately 60% lower than Hamrock and Dowson's one. Even if the contact conditions all reproduce pure sliding, the predictions of the Hamrock and Dowson isothermal model for rolling contact seem closer to the experimental evidence, especially for the MVo. In this work the spindle speed was kept as low as possible, primarily to avoid any impact on the results coming from the tribometer dynamics. Low speed and low load ensure low shear stress and little thermal effects even though sliding is there, and then large reduction of the lubricant film is likely avoided. The absence of considerable thermal effects was certified by running a 24h test whose friction curve is visible in Figure 7.1. The curve discloses a gentle wave which is attributable to the effect of the natural sine-shaped trend of the temperature over the day.

Table 7.2. Summary of the physical and gematrical parameters for the calculation of Lambda factor

Common parameters		Specific parameters			
			MVo - rotating	MVo - linear	HVo
E_{disc} [GPa]	73	v_{disc} [m/s]	0.0628	0.0189	0.0942
E_{ball} [GPa]	390	v_{ball} [m/s]	0.0000	0.0000	0.0000
Poisson _{disc}	0.208	U [m/s]	0.0314	0.0094	0.0471
Poisson _{ball}	0.220	F_N [N]	2	2	30
R_{disc} [m]	0.003	η_0 [cP]	105.2	105.2	621.1
R_{ball} [m]	∞	α [GPa ⁻¹]	30.5	30.5	34.8
k	1				
R' [m]	0.0015				
E' [GPa]	129				
SRR	2.00				

During the implementation of the tests, sliding speed has been handled as a “free parameter”, allowing it to change in the narrow range corresponding to the fixed rotating speed and varying radius. The values listed in Table 7.1 corresponds to the mid-range linear speed at 5.5mm radius. Table 7.2 summarizes the values of the physical properties and geometrical parameters having a role in the building of the lubricant film thickness at the contact region. For the meaning of each quantity the reader should refer sec.4.3.

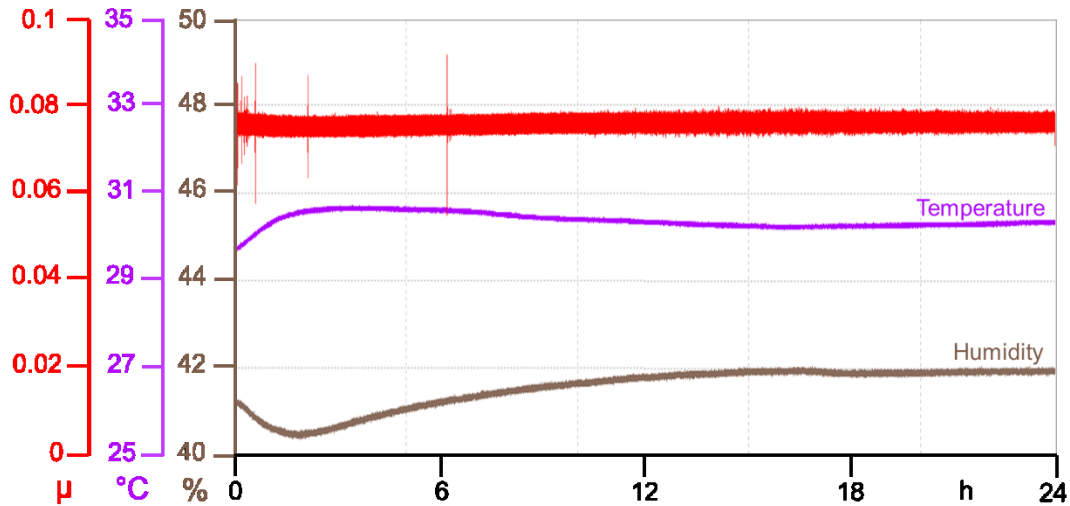


Figure 7.1. TRB3, MVo, 2N load, 100rpm, rotating test. 24h test attesting an excellent stability of the result even in the long run

These values represent anyway more qualitative than quantitative predictions anyhow, as outlined by Wheeler et al. [43], but several interesting remarks can be made from them. As introduced in sec. 4.4 $\Lambda = 3$ is the conventional widely accepted “safe” reference value above which solid contact among asperities disappears. Nevertheless, although Λ is low in the tests with the MVo, it does not necessarily follow that solid-solid contact arises (see Sec. 4.4.4).

Experimental evidences like the absence of macroscopic wear traces and the smoothness of the friction curves suggested that solid surfaces were always separated by a continuous film of lubricant. Of course, a “threshold” full-film lubrication (very close to mixed lubrication) is expected and it does not take much to have accidental asperities collision. The high sensibility to fibres or tiniest particles of dust in suspension in the oil is then probably related to this extreme working condition.

As to the HVo, the fully flooded regime predicted by the equations is in good agreement with the experimental evidence. The smaller number of rejected tests might be symptom of lower sensibility to lubricant particulate pollutants correlated to the thicker supporting film, even if the cleaning procedure is here longer and cumbersome. Being the load a minor parameter for the EHL, this prediction does not change if 40N or 50N load enters the equation. In this case, despite a “safe” operating condition (that is Λ factor closer to 3), the experimental evidence was very different. Being the changeover to instable friction behaviour between 30N and 40N load not foreseen by any analytical models, other influences never taken into account before should be involved.

Virtually all the experimental works on EHL in the scientific literature used optical interferometry, whose dedicated ball-on-flat test rigs make use of a tick flat glass disk. In this work, the samples consist of a very thin slip glued on the top of an aluminium sample holder. This layout was chosen instead of a sample made of glass as it was particularly convenient for industrial application. A glass sample is very fragile and repeated mounting onto and dismounting from the clamping system of the mandrel could easily frack the material. Moreover, in case of damaging of the surface of test it is enough to replace the slip with a new one. It serves for costs reduction too.

The presence of a layer of glue might play a fundamental role as it introduces two foremost uncertainties. First, gluing is never perfect and macro-irregularities (ridges and valleys) are likely there because of local stockpiles/shortcomings during cross-linking process of glue. Therefore, the surface of the thin slip cannot be as flat and regular as the surface of a polished glass block. These irregularities may intrude in the formation of a regular supporting film of lubricant in case they are large enough to be immune for flattening action of the lubricant that have been mentioned in Sec. 4.4.4.

Intuitively, the impact of these irregularities grows as the maximum contact pressure increases. Despite the film thickness is not function of load, its stiffness surely is and a stiffer supporting film induces larger stresses into the glass disk. It happened sometimes that the glass slips fell apart and it was probably because of an excessive local bending stress. Furthermore, a layer of glue, even a thin one, can influence the superficial elastic properties when laid out under an extremely thin body. The Young modulus of glass has been entered in the analytical models to account for the material in contact with the sphere whereas a “composite” elastic modulus, i.e. accounting for the layered sample surface, might be more representative.

Finally, the author found it strange that tests with HVo gave stable and repeatable friction results in a tighter range of track radii than tests with the MVo. Radii from 4 to 5mm and from 6 to 7mm seemed prohibited. No persuasive reason for this has been drawn up so far.

To the best of the author knowledge, no analytical equations have been developed to predict the film thickness of non-stationary/reciprocating sliding EHD point contacts. An early attempt was made by Petrousevitch et al. [44], but for nominal line contact only (e.g. cylinder-cylinder contact). The attempt of using the models for stationary conditions, by entering the average speed on the stroke, obviously leads to unrepresentative too low thickness values. Not to mention that they actually predict a null film thickness at both the stroke ends where speed is locally zero. There is evidence from various works in literature that under reversal of speed some oil remains entrapped between the surfaces and still supports the contact [45]. Moreover, the film thickness measured at the stroke centre is comparable to the one experimentally observed in unidirectional motion with similar non-dimensional factors [45], thus the analytical models introduced above may still apply to describe what happens at the interface at maximum speed. In Table 5 the calculus is made precisely following this hypothesis.

PART II

8 TRIBOLOGY OF THIN HARD COATINGS

8.1 OVERVIEW OF THE MECHANISMS OF DRY FRICTION AND WEAR

If two macroscopic or microscopic bodies are kept in contact by the action of a normal force and they are pushed to slide one over the other, an opposing force develops. This force takes the name of *friction force*: it belongs to the sliding plane and it is always oriented in the direction opposite to the relative motion. Friction forces are dissipative: their mechanical work is always negative; this entails a loss of energy for the system, which is degraded to heat.

Friction phenomena can be classified according to the two kinetics of relative motion:

- Sliding friction
- Rolling friction

In the following, this paper will focus on sliding friction and wear of hard interfaces, typical of ceramic materials, which is relevant to the subject of this study.

8.1.1 Friction

Historically, the Coulomb and Morin's model represents the first quantitative approach to the friction problem. It is based on wordings known from the time by the works of Da Vinci and Amontons [13]:

- There is proportionality between the maximum tangential force Q_s , acting on a body without altering its state of quiet, and the normal force F_N playing at the body-environment interface.
- In the state of motion, the tangential friction force F_T is proportional to the normal load F_N .
- The friction force is independent from the apparent contact area.
- The friction force is independent from the relative speed.

Until the force applied F_T reaches the limiting value Q_s , at the interface no slip occurs:

$$F_T < |Q_s| = \mu_s \cdot F_N \quad (32)$$

The quantity μ_s takes the name of *static coefficient of friction*. The two bodies remain in adherence because the reaction generated by the interface balances the thrust and maintain the static equilibrium of the system. Observations on real systems led to the assertion that in general μ_s is independent from the nominal contact area, while it depends on F_N and in certain situations also on the continued static contact before the onset of motion [46].

Once Q_s is exceeded, the imbalance of the forces triggers the motion: from this moment on, it is necessary to bring Q to a value Q_d to restore the dynamic equilibrium. Q_d is in general different from Q_s . According to this, an equivalent *kinetic coefficient of friction* is introduced.

$$F_T / F_N = \mu \quad (33)$$

Experimental investigations illustrate that also μ is independent from the nominal contact area, whereas it can depend on P , speed, contact materials and their surface finish [46].

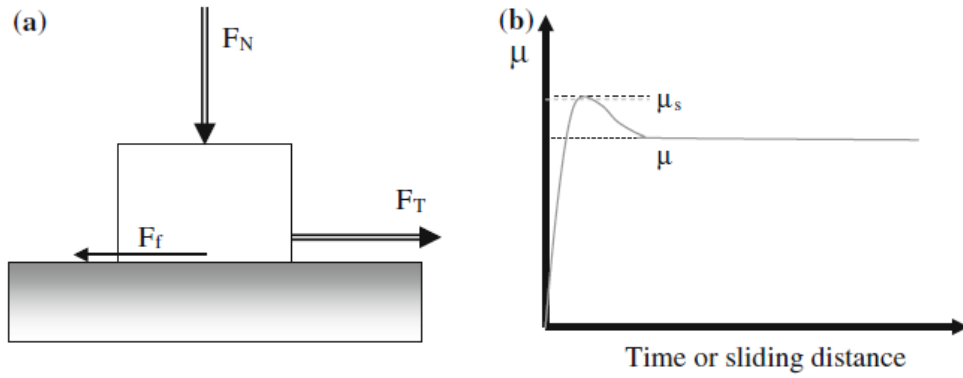


Figure 8.1 (a) Schematic of friction forces acting on a generic tribo-system; (b) Typical CoF trend at the onset of sliding
G. Staffelini, *Friction and wear*, 1 Ed., Springer, 2015

Coulomb-Morin's model is phenomenological and empirical: it is convenient to study friction from an engineering point of view. It proposes a practical approach which describes the consequences on the dynamics of the mechanical system, but it is inadequate when questions concerning the physics of the phenomenon arise.

The Bowden and Tabor's *adhesive theory* of friction is a mechanical theory [47] which traces back the tribological behaviour to the adhesive-cohesive interactions at the level of asperities. The adhesive theory affirms that the tangential force F_T , required to maintain a constant sliding velocity, is directly proportional to the critical shear stress τ_m required to separate the asperities in contact:

$$F_T = \tau_m \cdot A_{r,\tau} \quad (34)$$

Where: $A_{r,\tau}$ is the real contact area when a tangential force makes (or simply attempts to make) the surfaces slide. $A_{r,\tau}$ is higher than A_r which represents the static real contact area.

Under the action of a force that pushes the two contacting bodies to slide, a shear stress τ (Fig. 2.5), stressing the elements of material inside the ridges, is generated by a reaction. Sliding occurs when the shear stress acting at the joints reaches the critical value τ_m . In no way this value can be greater than the shear strength τ_y of the softer material, which is approximately:

$$\tau_y \approx H/(5,2 \div 6) \quad (35)$$

Where: H is the material hardness;

If the shear strength of the junctions is lower than the shear strength of both the materials, sliding takes place once the shear stress at the junction plane reaches τ_m . If the adhesion is so strong that it results in a strength ideally greater than the one of neighbouring materials, then τ_m corresponds to the shear limit of the softer material.

In the theory of adhesion τ_m is modelled as a function of the *work of adhesion* per unit area, usually indicated as W_{12} . It represents the energy that theoretically must be supplied to separate two surfaces in contact, and it is related to the surface energies of the bodies.

$$W_{12} = \gamma_1 + \gamma_2 - \gamma_{12} = c(\gamma_1 + \gamma_2) \quad (36)$$

Where: γ_1, γ_2 are the surface energies of the interfaces with the surrounding environment [J/m²];
 γ_{12} is the surface energy of the interface that the two bodies form when they are in contact [J/m²];
 c is a coefficient called *tribological compatibility*.

Surface energies vary between 0.1 J/m² and 0.5 J/m² for ceramics (cleaned and degreased surfaces) but the possible presence of organic contaminants on the surfaces tends to reduce them. The constant c is an experimental constant that accounts for γ_{12} which is very difficult to determine. c is equal to 1 for the contact between identical materials and always lower when different materials come in touch. In the case of contact between ceramics, Rabinowicz [46] has determined through experimental data that the compatibility parameter can be set to 0.6 for compatible ceramics (such as two oxides or two nitrides), and 0.36 for incompatible ceramics.

Polymer and ceramic materials are prone to give rise to prevalent elastic deformations of the contacting asperities at rest, i.e. their Greenwood-Williamson index of plasticity is $\Psi < 0.61$. The widespread elastic behaviour usually persists even if a tangential force is applied so that $A_{r,\tau}$ is slightly higher than A_r . Nevertheless, asperities of hard (ceramic) materials may locally disclose plastic deformations because the compressive load at the small contact areas is extreme. This means that practically every material shows a microscopic elasto-plastic contact behaviour.

In these conditions the adhesive CoF can be calculated resorting to the Greenwood-Williamson model of A_r [46]:

$$\mu_{ad} = 3.2 \sqrt{R_S/\sigma_S} \cdot (\tau_m/E^*) \quad (37)$$

Where: R_S is the composite asperity radius;
 σ_S is the composite standard deviation of the asperity height distribution;
 E^* is the composite elastic modulus of the material pair.

Even metals, in some conditions, may undergo deformations more accurately modeled as elastic deformations. This is the case, for example, of cemented or nitridated steels having high surface hardness.

Alongside with adhesion, *abrasion* plays a major role in friction phenomena at the tribological sliding interfaces. There are two types of abrasion [46]:

- Two-body abrasion;
- Three-body abrasion.

Two-body abrasion occurs when hard particles embedded in one of the two contacting bodies penetrate and plough the partner surface. Typical abrasive particles are ceramic reinforcing particles (Al₂O₃, SiC) or carbides in stainless steels (FeC, Cr_xC_y). Two-body abrasion can appear between homogeneous materials too, provided that a sizeable difference in hardness is there. In this case, the asperities of the harder surface act as abrasive bodies.

The reason why a friction force originates is to be partly attributed to adhesion again. Together with the mechanical action, result of the displacement or removal of material, sliding is also counteracted by adhesive bonds coming from the interpenetration of surfaces (instead of simple rubbing of ridges).

Equation (38) is the output of the simplified model for two-body abrasive friction proposed by Rabinowicz [48]. Abrasive particles are modelled as non-deformable conical bodies with a certain attack angle Θ , as shown in Figure 8.2a.

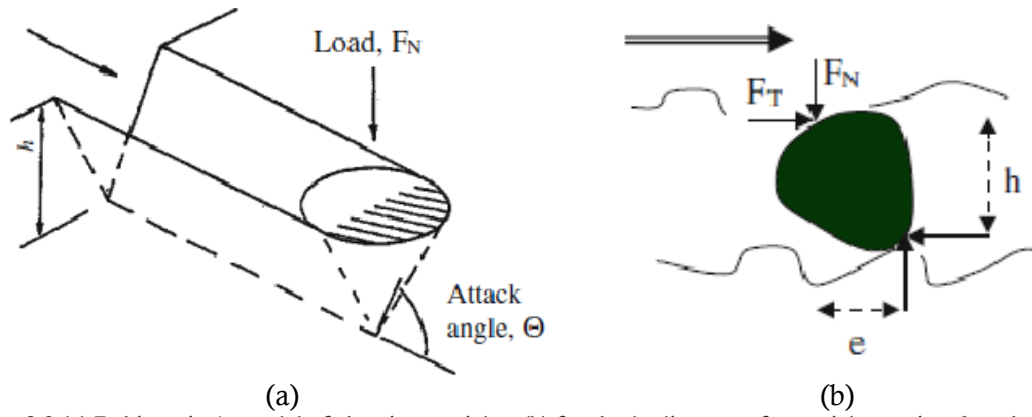


Figure 8.2 (a) Rabinowicz's model of abrasive particles; (b) free body diagram of a particle causing three body abrasion
G. Straffelini, *Friction and wear*, 1 Ed., Springer, 2015

The normal load F_N is calculated considering that one half of the lateral surface of the cone (the ploughing side) is able to support the load; the tangential force F_T is supposed proportional to the yielding pressure of the material and the cross-sectional area of the groove.

$$\mu_{abr} = F_T / F_N = 2 \tan \Theta / \pi \quad (38)$$

This model works for both ductile and brittle materials, regardless of whether particles remove the material or let it plastically flow sideways. The influencing parameters of the phenomenon are just the penetration depth and the attack angle.

As to the three-body abrasion, it originates when hard particles are free to roll between the mating surfaces. Particles may either be unleashed by one of the contacting materials (including wear debris) or come from the environment (dust, sand and other inorganic debris). The theoretical evaluation of the coefficient of friction is much more problematic in this case because you cannot know the type of motion of such particles: it could be rolling or more likely of rolling-sliding. It can be argued that if pure rolling is there, the following relationship must apply:

$$F_T / P = \mu_{abr} < e / h \quad (39)$$

Finally, it can be observed that real tribological systems always experience a mix of simultaneous adhesive and abrasive actions. Assuming that superimposition of effects holds, the coefficient of friction of a specific tribological system should be predicted as the sum of the two contributions:

$$\mu = \mu_{ad} + \mu_{abr} \quad (40)$$

Adhesion and abrasion are the two most importance friction mechanisms in dry contacts. In a general case, other phenomena may contribute to friction and equation like equation (40) still applies provided that each contribution is added with a dedicated term. For example, contribution exists from hysteresis of materials, rolling, viscous/viscoelastic deformations of solid material (or lubricants), etc...

$$\mu = \mu_{ad} + \mu_{abr} + \mu_{hys} + \mu_{roll} + \mu_{vic}$$

8.1.2 Wear

Wear is any natural damage of real bodies due to the use and leading to the formation of fragments (or debris) that leave the tribological system. Understanding the causes of wear and knowing the involved physical phenomena allows the designer to limit its adverse effects on the components of a mechanical system, e.g. the increase in vibration and noise, fatigue, impulsive loads, increase of the backlashes in mechanical connections.

Depending on the nature of the interaction between the bodies, various wear processes can be identified: wear by sliding, by rolling, by rubbing (or fretting), by erosion, etc. However, in each process the damage from wear can be traced back to the action of one or more precise wear mechanisms. DIN 50320:1979 recognizes only four wear mechanisms:

- Adhesive wear
- Abrasive wear
- Tribo-chemical wear
- Fatigue wear

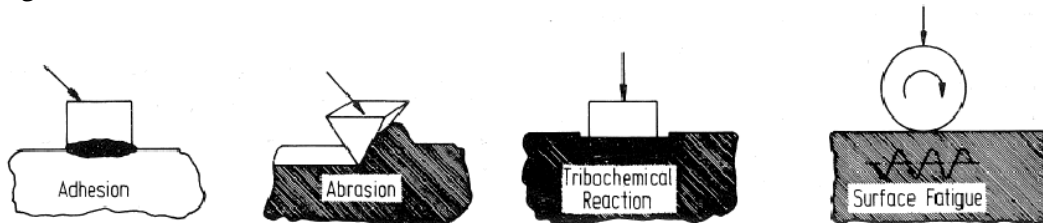


Figure 8.3. Fundamental wear mechanisms by DIN 50320:1979
K.H. Zum Gahr, *Microstructure and Wear of Materials*, Elsevier, 1987

Adhesive wear is a mechanism in which the adhesion of ridges plays a predominant role. Recalling the theory of adhesive friction (see Sec.8.1.1), if a micro-junction is able to withstand a virtually greater shear stress than τ_y , failure occurs within the material of one of the two asperities, when τ is exactly as high as τ_y . At every breakage of a micro-junction, a small portion of material may remain welded to the surface and give rise to a wear debris when released. However, the probability of a cleavage at the junction plane is greater than the probability of asperity failure. Therefore, the junctions releasing a wear fragments are a very small part of the total number, in usual conditions [49].

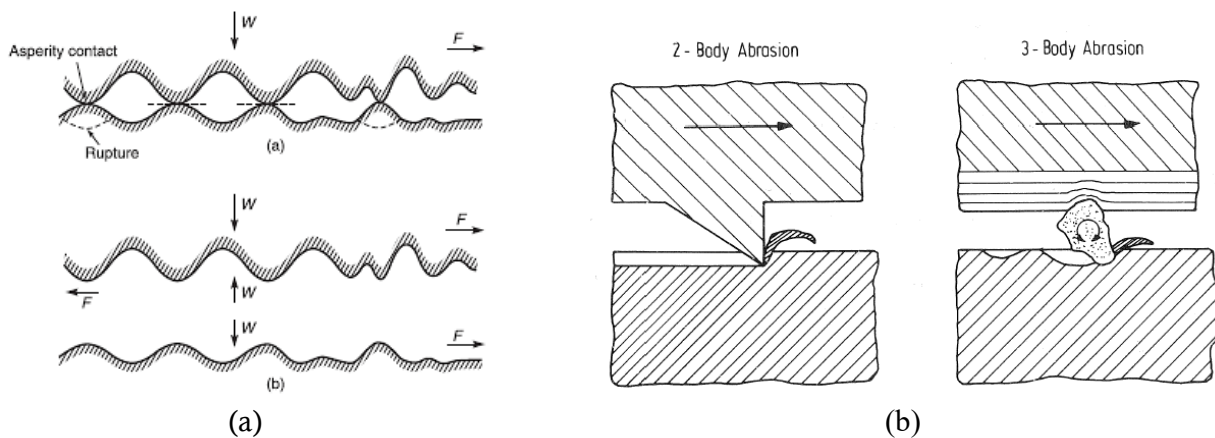


Figure 8.4 (a) Schematic of the formation of an adhesive wear debris; (b) abrasive wear modes
K. H. Zum Gahr, *Microstructure and Wear of Materials*, Elsevier, 1987

If the applied pressure is greater than a critical value p_{max} , large cracks (whose dimension exceeds that of asperities) may originate and propagate towards the bulk material. Wear by brittle fragmentation may affect larger portions of the material. Otherwise, as stated in the first instance, fragmentation is rather confined at the asperities. In this latter case, friction and wear are relatively low and wear debris is very fine; in the former case, friction and wear are quite large and fragments have a blocky or plate-like shape on the scale of the grain size [46].

$$p_{max} \geq \frac{5.36 \cdot K_{Ic}}{\sqrt{\pi c} \cdot (1 + 10\mu)} \quad (41)$$

Where: K_{Ic} is the fracture toughness;
 c is the crack length;
 μ is the coefficient of friction.

Abrasive wear is connected to the presence of abrasive bodies into the tribological system, either belonging to it or coming from the outside. Abrasive wear leads to considerable removal of material; the presence of abrasion is always marked by characteristic deep superficial grooves indeed. Abrasion is a widespread phenomenon, the most common in actual tribological interfaces.

In analogy to Sec. 8.1.1, two abrasive wear mechanisms can be distinguished: *two-body* and *three-body abrasive wear*, depending on whether the abrasive particles are respectively constrained or free to roll between the mating surfaces. It has been experimentally observed that the phenomena of abrasive wear are different in form and entity, depending on the parameter r , that is the ratio between the hardness of the surfaces undergoing abrasion and the hardness of the abrasive particles.

$$r = H_{\text{surface}}/H_{\text{particles}} \quad (42)$$

Based on this, Richardson [47] proposed a second possible classification:

- *Abrasion by hard particles* ($r \leq 0.5 \div 0.8$): their hardness is higher than the one of the worn surfaces and the wear rate is high.
- *Abrasion by soft particles* ($r \geq 1 \div 1.4$): their hardness is equal to or less than the one of worn surfaces and the abrasion is delicate, uniform and with a very low wear rate.

The most severe case of abrasion is the two-body abrasion by hard particles which gives rise to four different modes (Figure 8.5):

- Microploughing;
- Microcutting;
- Microfatigue;
- Microcracking.

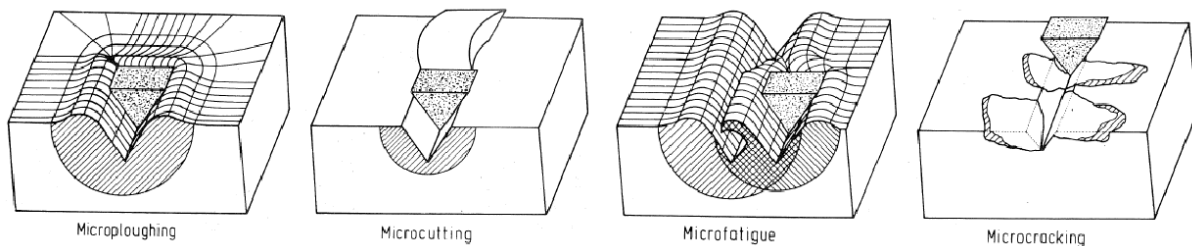


Figure 8.5 The four modes of the two-body abrasion

K.H. Zum Gahr, *Microstructure and Wear of Materials*, Elsevier, 1987

Microploughing and microcutting are the most common modes. Microploughing appears when each abrasive particle produces a groove without (ideally) any volume of wear, i.e. the material simply flows on the side of the particle. On the contrary, microcutting appears when the particle completely removes the volume of the groove without any other displacement of material. Wear is maximum in these latter conditions. According to Mulhern et al., the incidence of one or the other condition depends on the attack angle of the abrasive particles which in turn depends on [46]:

- Geometry;
- Size;
- Hardness;
- Turnover of particles at the interface;

If simultaneous or successive scratches from microploughing occur in the same area, the cumulation of plastic deformation for ratcheting may lead to the detachment of little portions of material. This is called microfatigue and it is typical of ductile material as long as microploughing.

Microcracking is typical of brittle material for which the mechanism of spalling dominates. The loss of material is caused by the nucleation of brittle cracks around the tip of the particle in contact with the surface. These cracks grow towards the surface following the mechanism showed in Figure 8.6 and a debris is eventually produced.

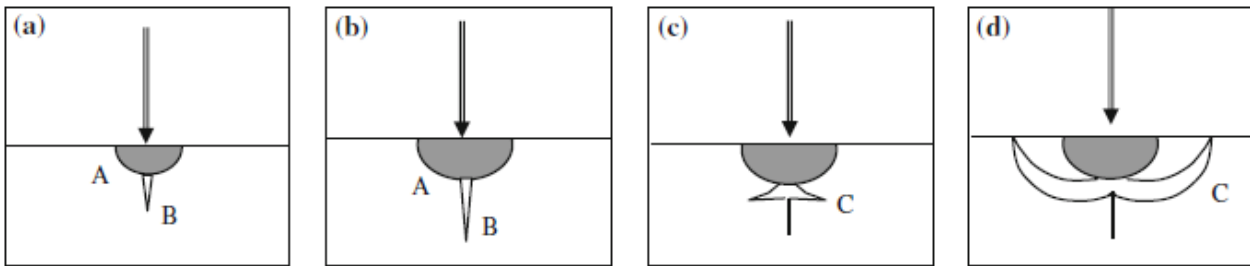


Figure 8.6 Formation of a brittle cracks by the Lawn and Swain mechanism. (a) Initial plastic deformation with the opening of a crack perpendicular to the surface; (b) propagation of the crack with increasing applied load; (c) load removal followed by closing of the first crack and formation of new radial cracks by the action of local residual stresses; (d) spalling when the radial cracks reach the surface.

G. Straffelini, *Friction and wear*, 1 Ed., Springer, 2015

Wear by *surface fatigue* is caused by alternating and repeated loads that cyclically stress the surface of a body. The superficial fatigue proceeds by nucleation and propagation of cracks, until, after a certain number of cycles, one reaches the detachment of an entire portion of surface material. This mechanism of wear, unlike the others, is not “progressive”: it does not manifest continuously and in a growing way to the continuation of the interaction. For this reason, little importance is given to the actual volume of material removed. In this case, the evaluation of the useful life of the tribological system (before fatigue emerges) is far more significant.

Surface fatigue wear is strongly influenced by the lubrication regime (see sec. 4.4). Two different conditions can be distinguished with reference to this latter [50]:

- Microscopic fatigue;
- Macroscopic fatigue.

Microscopic fatigue is experienced in limiting or no lubrication conditions. When the asperities enter in contact with each other or with debris, it may happen neither adhesion nor reciprocal abrasion but simple rubbing results. Such a situation is very common if an adsorbed lubricating layers covers the surfaces preventing the solid-solid contact. Anyway, adsorbed layers still allow for the cyclic mechanical deformation of asperities [9] and cracks generate at the surface level in a way similar to Figure 8.6.

Macroscopic fatigue involves mixed or fluid-film lubrication conditions where a thick layer of lubricant is interposed between the surfaces. Close contact between asperities is totally or partially avoided but cyclic hydrodynamic loads are still there. Unlike microscopic fatigue, cracks originate in depth (Figure 8.7) and mainly in the vicinity of reticular defects (hard particles, microporosity...).

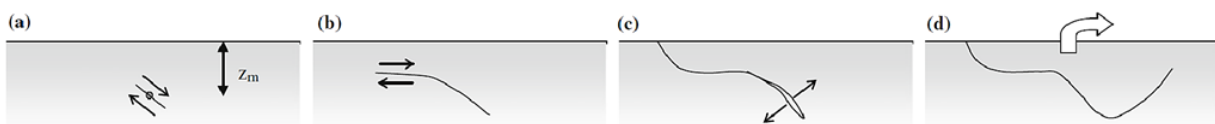


Figure 8.7 Nucleation and propagation of a subsurface fatigue crack.

G. Straffelini, *Friction and wear*, 1 Ed., Springer, 2015

Tribo-Oxidative wear is a particular form of corrosive wear. Generally speaking, corrosive wear is any loss of material by the chemical attack of an aggressive environment. In the specific case, the aggressive agent is the atmospheric oxygen yielding surface oxidation.

Tribo-oxidative wear is more complex than other wear mechanisms as it involves both chemical and mechanical actions. Causal relationships between mechanical and chemical contributions may be different. Sometimes the production of debris comes first and then oxidation takes place as they stay in the contact zone (*indirect tribo-oxidative wear*). Alternatively, a layer of oxides may first coat the surfaces so that debris are the result of the oxidized layer fragmentation (*direct tribo-oxidative wear*).

8.2 CLASSIFICATION AND PROPERTIES OF HARD COATINGS

Wear resistant coatings consist of layers of (usually) hard materials which are intended to give prolonged protection against wear to mechanical components. Applications of wear resistant coatings are found in many fields of industry, for example excavator shovels and crushers, cutting and forming tools, rolling bearings, etc... In most of these applications, wear rather than friction is the critical problem. One of the methods to control wear is thus adding an exotic, high-performance resistant material on the top of a cheap substrate material. Most engineering items are made of steel because it is a cheap and well-known material although it often does not meet wear and friction requirements. At the same time, the vast majority of wear resistant materials are very expensive and brittle (with inadequate mechanical characteristics) and can only be used as a coating. The best trade-off is then to continue designing engineering components by using the classical material to fulfil structural requirements and protect them from wear with the suitable film on the top.

A hard coating on a softer substrate has proved to be a tribologically very beneficial material combination with both high and little thickness. The thinner coatings are usually suitable for precision components while the thicker coatings are more appropriate for large clearance components and in presence of hard abrasive or erosive wear.

Table 4.1 shows a possible list of the most widely used hard coatings in engineering and industrial applications, with their main physical characteristics [51].

Table 8.1. List of the main commercial coatings

Material	Hardness [kg mm ⁻²]		Young's modulus [kN mm ⁻²]	Poissons ratio	Thermal expansion coefficient [10 ⁻⁶ K ⁻¹]	Melting or decomposition temperature [°C]
	Bulk	Film				
TiN	2000	≤3680	440	0.25	9.35	2949
TiC	2900	≤4000	450	0.19	7.4	3067
TiB ₂	3370		480		8.0	
VN	1500		460		8.1	2177
VC	2900		430			2648
ZrM	1500	≤4500	510	0.25	7.2	2982
NbN	1400		480		10.1	2204
NbC	2400		580	0.22	6.6	3600
TaN	1000				3.6	3093
CrN	1100		400		2.3	1500
Cr ₃ C ₂	1300		400		10.3	1810
HfN	1600	≤4700			6.9	3387
HfC	2700	≤3900	460	0.18	6.6	3928
WC	2100		695	0.185	4.3	2776
Al ₂ O ₃		≤2100	400	0.23	9.0	2300
SiC	2600	≤4000	480		5.3	
BN	3000–5000		660			
B ₄ C	3000–4000		440		4.5–5.6	
C, diam.	9000		440–590		0.8	

B. Bhushah, *Handbook of hard coatings*, I ed., Noyes

Table 8.2. List of the most important properties of coatings

1. Adhesion
2. Thickness
3. Surface finish
4. Corrosion resistance
5. Friction/wear performance
6. Hardness
7. Porosity
8. Composition
9. Internal stress
10. Structure/morphology

K. Holmberg, A. Matthews, *Coatings tribology*, Elsevier, Amsterdam, 1994

Table 8.2 shows the list of the most important coating properties according to Holmberg et al. [4]. It is important to underline that the ranking in their importance is extremely variable depending on whether the coating is intended for production or research and development use.

The reader can refer to specific textbooks for a detailed discussion of each property. In the following few words it will be said about the properties of thickness and adhesion whose complexity and influence on the system response is too often trivialised.

Thickness is only apparently a simple property: it has some criticality, especially in tribological applications. First, high thickness does not always imply longer lifetime of the coating. There is indeed a complex interplay between thickness and other properties like adhesion, intrinsic stress within the coating, porosity, lattice morphology, hardness. Thus, simple step-height measurements of thickness could be meaningless, as the tribological behaviour would not be necessarily linked to thickness values alone. In addition, the definition of the thickness depth is unclear for some coatings since no sharp transition between the layer and the substrate is visible.

Adhesion is the vital ability of a coating to remain attached to the substrate under the required operating conditions. Adhesion is theoretically defined as the energy stored in the chemical bonds between the coating and the substrate. It is however hard to evaluate this property in such a way that it remains possible to compare different coatings, laid onto different substrates, under different application conditions. Many other extraneous factors have to be taken into account, such as internal stress, defects, type of stress and so on.

For example, a porous columnar coating with low nominal adhesion strength is more likely to remain adherent under bending or scratching stress, since it will simply crack perpendicularly to the surface along column boundaries. A dense cohesive film, despite strongly bounded from the chemical point of view, could experience greater interfacial stress. In this case it is more likely that debonding and thus flaking occurs under bending or scratching stress. Simultaneously, coatings with similar bond strengths may exhibit different adhesion behaviours in different working conditions. In this scenario the concept of *practical adhesion* or *effective adhesion* must be introduced, as opposed to the chemical concept of basic adhesion [4].

8.3 DEPOSITION METHODS

There are many different methods available to cover a substrate with a hard-protective layer. Stachowiak et al. [13] provide a useful table where the main coating techniques with their principal merits and demerits are listed and compared.

Physical and chemical vapour deposition	Thin discrete coating; no limitations on materials
Ion implantation	Thin diffuse coating; mixing with substrate inevitable
Surface welding	Suitable for very thick coatings only; limited to materials stable at high temperatures; coated surfaces may need further preparation
Thermal spraying	Very thick coatings possible but control of coating purity is difficult
Laser glazing and alloying	Thick coatings; coating material must be able to melt
Friction surfacing	Simple technology but limited to planar surfaces; produces thick metal coating
Explosive cladding	Rapid coating of large areas possible and bonding to substrate is good. Can give a tougher and thicker coating than many other methods
Electroplating	Wide range of coating thicknesses, but adhesion to substrate is poor and only certain materials can be coated by this technique

Table 8.3. Available techniques for modifying the surface to improve its tribological characteristics

G.W. Stachowiak, A.W. Batchelor, *Engineering Tribology*, Butterworth-Heinemann

The most widely used techniques to produce thin coatings are the physical vapour deposition (PVD) and chemical vapour deposition (CVD) and ion implantation. They fall within the category of vapour-phase plasma-based deposition methods and allow to have high quality coatings with no limitation on the coating or substrate material. The layers obtained usually have a thickness ranging from 2 to 10 μm and are particularly suited to improve sliding wear and low-stress abrasive wear. This paper will describe in detail only these three techniques. More details about surface coating technique can be found in specialised papers, like the textbook by Holmberg et al. [4].

8.3.1 Physical Vapor Deposition

Physical vapor deposition is based on the condensation of the vapours of the hard material onto the substrate surface. The PVD processes require moderate temperature (less than 500 $^{\circ}\text{C}$) and are conducted under sub-atmospheric pressure either in vacuum or in a controlled atmosphere of inert gas. These extreme conditions are needed to ensure that no trace of atmospheric oxygen and water are there: they would cause indeed oxidation of vapor molecules due to high temperature. These very clean conditions are fundamental to have a perfect adhesion between the atoms of coating material and the atoms of the substrate and also to minimize porosity (thanks to the absence of dirt inclusions). By resorting to PVD, virtually any material or compound which does not undergo dissociation can be deposited onto any kind of substrate; this flexibility has made PVD an extensively used technique in recent years.

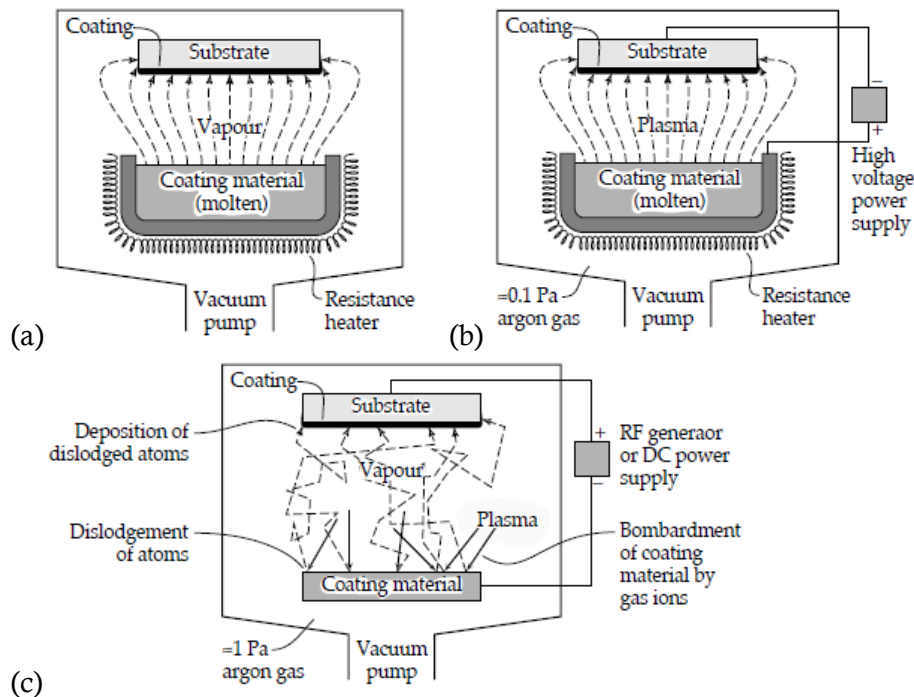


Figure 8.8 The three main PVD processes: (a) Evaporation; (b) Ion-plating; (c) Sputtering
G.W. Stachowiak, A.W. Batchelor, *Engineering Tribology*, Butterworth-Heinemann

There are three main processes under the name of PVD, although other variants do exist.

- *Evaporation* (Figure 8.8a). The source material for coating is heated up to the melting point. High power density heating methods, such as an electron beam, are usually used with materials having high melting point, e.g. refractory ceramic materials. The high temperature and low pressure promote the evaporation of the source material, atoms in the vapour state travel in straight lines towards the substrate where condensation takes place. The adhesion of the coatings atoms to the substrate is function of their kinetic energy, which is maximized by adjusting the distance between the source and the substrate so that it is less than the mean free path of gaseous atoms (about 0.15 - 0.45m). Because the atoms of vapour travel in straight lines, this results in a 'shadowing effect': the external surface of the coating layer will not directly face the coating source and components like gears, moulds and valve bodies are difficult to coat

uniformly. Sometimes this process may resort to reactive gas atmospheres (e.g. nitrogen, oxygen, or hydrocarbon). The gas reacts with the ionized coating vapour to form a compound that is deposited on the work piece. For example, TiN is obtained by using a titanium source and pure nitrogen.

- *Ion-plating* (Figure 8.8b). The process of ion-plating involves both thermal evaporation of the source material, like the evaporation process, and the ionization of the vapour due to the presence of a strong electric field. The process is carried out into an inert gas atmosphere. The gas ionisation, usually argon, occurs by applying an electric potential between two electrodes (the molten coating source and the workpiece). When sufficient voltage is applied, a stable passage of current is obtained and the atoms of the coating material are conveyed from the 'source' electrode to the 'target' electrode pushed by the 'propulsive' force of the electric field. The argon and coating ions are accelerated towards the workpiece and the coating material is embedded in the substrate with no clear boundaries between the film and the substrate, because of the high impacting energy. Ion-plating differs from other processes because a modification of the microstructure and composition of the deposit takes place during the ion bombardment. Also in this case, the presence of reactive gases allows the deposition of compounds. This process is widely used in numerous applications, although limited to metals.
- *Sputtering* (Figure 8.8c). The source material is bombarded by high-energy inert gas ions (typically argon ions) without any evaporation or heating of the former. Individual atoms are disclosed and ejected by mechanical actions of an ions' beam and then attracted to the work piece thanks to a weak electric field. The negligible substrate heating and the absence of direct heating of the source material are features that make sputtering universal, in the sense that even substances which decompose at elevated temperatures can be sputtered. The condensation process is here critical to coating quality: sputtered films generally display a better adhesion on the substrate than the evaporated coatings, but a porous structure with poor wear resistance may grow. Coating rate, argon gas pressure and bias voltage must be accurately set.

8.3.2 Chemical Vapor deposition

In the CVD processes, the vaporised coating material and other gaseous chemical reactants are introduced into a closed reactor. Differently from PVD, the deposition of a hard film takes place after a chemical reaction that involves the source material, the substrate surface and other relevant chemical compounds. The portion of the workpiece where deposition occurs is kept at a higher temperature than the vapour source, but still below the melting temperature of the coating, and the reaction is activated by the thermal level itself (from 1000°C to 2000°C). During the process the coating material is thus deposited, atom by atom. The CVD process at low pressure allows the deposition of coatings with superior quality and uniformity over a large substrate area and with high deposition rates. Although coatings layers usually exhibit excellent adhesion, such a technique is suitable to cover hard metals or refractors materials tolerating high temperatures.

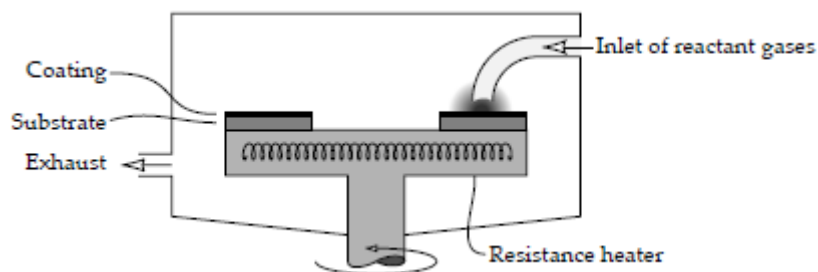


Figure 8.9 Schematic diagram of the chemical vapour deposition process

G.W. Stachowiak, A.W. Batchelor, *Engineering Tribology*, Butterworth-Heinemann, 2005

8.3.3 Ion implantation

Ion implantation is an 'extremization' of the ion-plating process (see Sec. Physical Vapor Deposition 8.3.1) in which the energy of ions in a plasma is raised to such a high level that the plasma is converted into a direct beam and conveyed to the substrate surface. The kinetic energy of coating material ions is so high that they penetrate the surface of the substrate and destroy the crystal structure. A peculiar near-surface microstructure results and it is very often an amorphous mix of remnants of the crystal structure and interstitial implanted atoms.

This technique allows the deposition of both metallic and non-metallic materials into metals, ceramics or even polymers as the ion implantation is carried out at low temperatures. However, compared to other surfaces, the hard layers from ion-implantation are very shallow, about 0.01 to 0.5 μm . On the one hand, this is a disadvantage of the method as it reveals useful in lightly loaded contacts only; on the other, it is an asset because tolerances are maintained, and the precision of the component is not distorted.

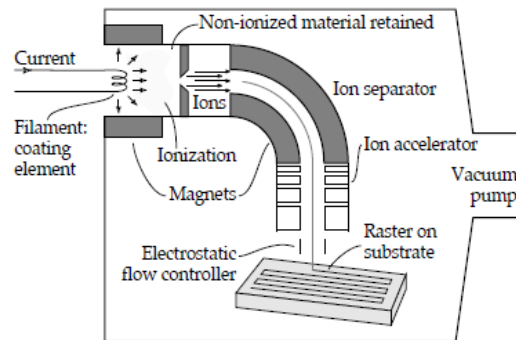


Figure 8.10. Schematic diagram of the ion implantation method
G.W. Stachowiak, A.W. Batchelor, *Engineering Tribology*, Butterworth-Heinemann

8.4 TRIBOLOGY OF THIN FILMS

8.4.1 Macroscopic behaviour

In contacts with one or two coated surfaces, four main parameters to control the tribological contact process can be defined according to Holmberg et al. [4]:

- the coating-to-substrate hardness relationship
- the thickness of the coating
- the surface roughness
- the size and hardness of the debris in the contact.

With respect to these parameters and their possible combination, many different contact conditions result. The very typical tribological contacts are schematically summarized in Figure 8.11. The tribological behaviour of each condition strongly depends on the key mechanisms involved and has to be treated on its own merits. In the following, only the case of a soft substrate covered by a thin hard coating will be dealt with as it is the case of the experimental results.

Thin hard layers are intended to separate the substrate from the counter-face in order to increase the wear resistance at the tribological interface. This is possible if the added layer on the top is hard and able to prevent ploughing to take place. If ploughing is cut back, both friction and wear could benefit. However, a harder layer introduces also a higher shear strength at the contact interface. Recalling the adhesive theory of friction (see Sec. 8.1.1), the higher the shear strength of the material involved into the contact is, the higher τ_m and the coefficient of friction value will result. Since adhesion is almost always present, the hard coating can have the effect of increasing sliding friction instead of reducing it if no tribo-films are formed. Unfortunately, the increase in friction coupled to the increased shear strength is generally dominant.

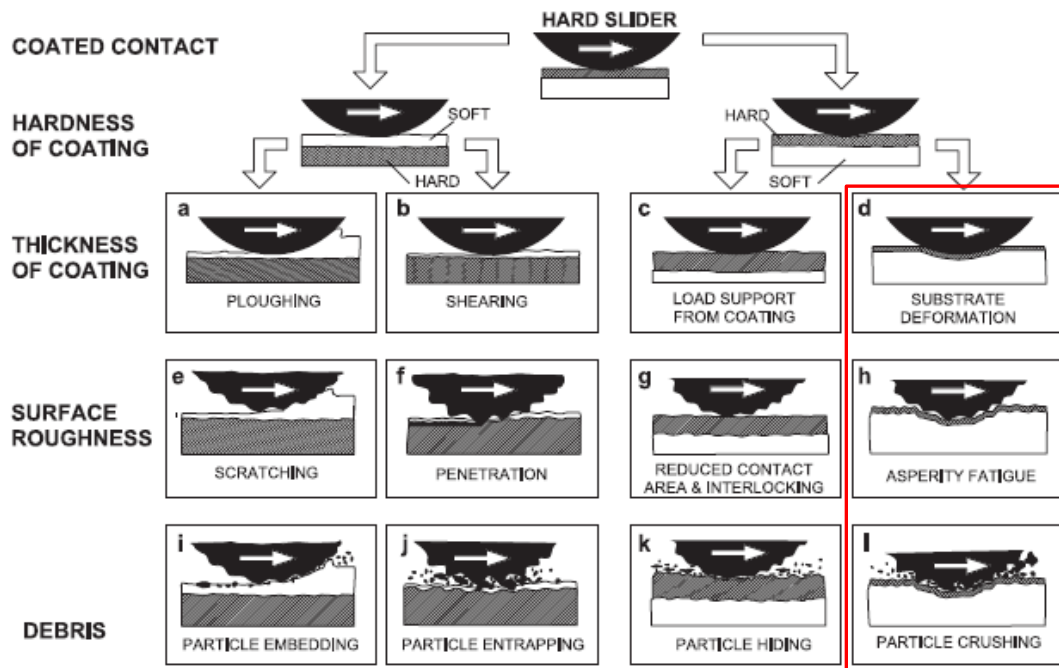


Figure 8.11. Contact conditions and mechanisms influencing friction when a hard-spherical slider moves on a coated flat surface

B. Bhushan., *Introduction to Tribology*, II ed., John Wiley&Sons

The protective action against ploughing by a thin hard layer on top of a softer substrate is anyway effective if the coating is able to support the load. For very soft substrates and thin layers, a considerable deflection of the substrate may take place, wreaking two main drawbacks for tribo-systems. First, the deflection of the surface brings about the enlargement of the contact path between the slider and the coating. Since the contact area is, along with τ_m , the other influencing parameter of adhesive friction, an extra increase in friction derives. Furthermore, an indentation effect may arise at the contact which in turn adds a 'ploughing effect' on friction.

As to the ability to resist the high stresses, it also depends on the strength of adhesion at the interface. Single or repeated loading can result in breaking of the adhesive bonds between coating molecules and substrate molecules, followed by the liberation of flake-like wear debris from the coating.

Secondly, deflection increases the stress in the coating and at the coating-substrate interface, possibly resulting in fracture or fatigue cracks either in the coating layer or into the substrate material. The fragmentation of the coating by brittle fracture is also called *cohesive fracture*. Figure 8.12 represents the occurrence of a typical situation of thin and ultra-thin coating. In the extreme case cohesive fracture may evolve in *adhesive failure* (i.e. flaking of the coating), that is favoured by low coating-substrate adhesion and by the presence of compressive stresses that induce debonding and buckling

Coatings with a higher ratio between hardness and elastic moduli have a longer elastic strain to failure [9], and are thus more able to deform without yielding and without cracking as the substrate deforms. As the thickness of the protective layer grows, the load-bearing capacity is improved, and the overall deformation is reduced even with soft substrates.

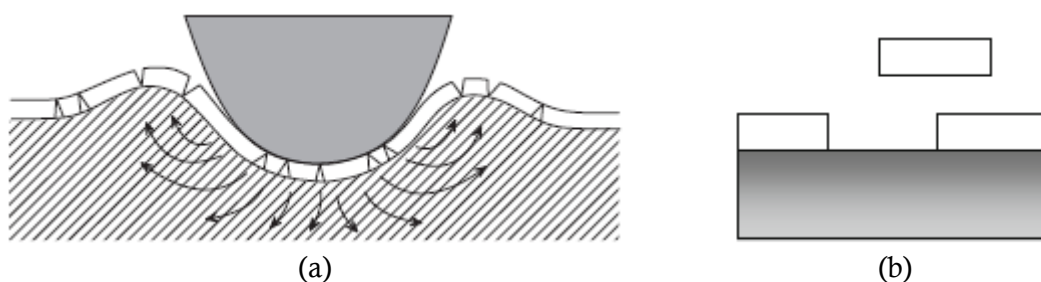


Figure 8.12. (a) Cohesive fracture of a hard-brittle coating on a soft substrate due to indentation effect; (b) flaking of the coating

It is important to point out that the presence of a thicker layer is not always beneficial. Under similar deformation conditions, a thicker coating will experience higher bend stress and its fatigue life may be considerably shorter than the one of a thin coating. Coatings typically have columnar growth morphologies and normal cracks at the surface are the most common cases. These are large in a thick coating and may easily exceed the critical crack length causing irreversible propagation according to the LEFM theory. However, as thickness is increased, the presence of defects in the coating also increases and crack formation becomes more likely.

Residual stress plays an important role too. Generally speaking, the deposition methods working at higher temperatures are more prone to give rise to residual stress state into the coating layer. This stress state typically brings about a compressive state which is beneficial with regard to cohesive fracture since they decrease any applied tensile stress under load. On the other hand, if the adhesion coating/substrate is weak, it could induce flaking of the coating. The picture is further complicated by the local temperature experienced during sliding. An abrupt temperature rise induced by frictional heating can induce the formation of tensile stresses that favour brittle cohesive fracture within the coating.

8.4.2 Microscopic behaviour

Following the energy accommodation concept by Holmberg and Matthews, the microscopic coating response at the level of the asperities can be split up into three components: elastic deformation, plastic deformation, and brittle fracture.

If the elastic deformation dominates, at the end of the interaction the material will elastically move back to its original position. The mechanical work of the slider is degraded to heat and the main parameter indicating the material response is the Young's modulus. In the event of plastic behaviour, the deformation is permanent, and the original shape is not restored at the end of the interaction. The mechanical work (i.e. the rubbing action) is transferred to heat and permanent modification of the crystal lattice. The key parameter here is the shear strength. Since the hardness represents, in a way, the plastic deformation resistance of the surface, the hardness can be chosen as the key parameter too.

In case brittle fracture appears, the material movement is arranged by both deformation and material cracking. It means that the sliding contact creates new cracks in the surface and the mechanical work becomes partly heat and partly surface energy needed for the formation of new internal free surfaces. The most important parameter is the fracture toughness, K_{IC} , which can be more conveniently expressed as strain energy release rate, G_C .

It should be taken into account that in real cases these three components of the tribological response have an effect on a real material that is not defect-free. There are many kinds of defects in a real coating layer: micro-pores due to molecular pile-up during the deposition process, fissures at the coating-substrate interface due to weak adhesion, cracks perpendicular to the surface after earlier sliding situations, etc.

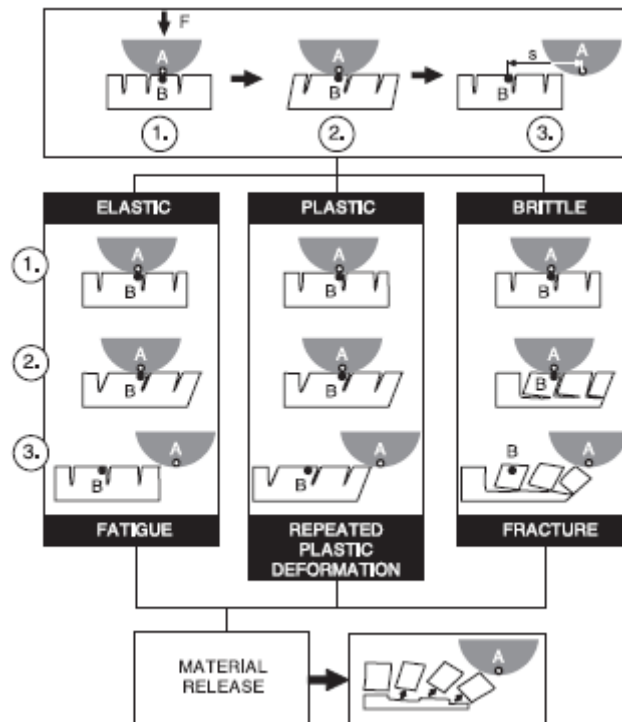


Figure 8.13 Particle formation mechanisms in the elastic, plastic, and brittle energy accommodation modes.
 B. Bhushan., *Modern tribology Handbook.*, CRC Press, 2001

Therefore, both in the prevailing elastic and in plastic regime, the reoccurrence of a certain number of contacts will lead to the growth of pre-existing cracks or the formation of new fatigue cracks. In the brittle fracture situation, the repeated contacts will result in the nucleation of more new cracks a fortiori. These modes are schematically depicted in Figure 8.13.

You can see that in all three cases the focal point is the generation and propagation of cracks that eventually result in material release from the surface, and wear particles will be formed finally. In ceramic coatings, the coating thickness and grain size are important parameters which govern the crack propagation. A microstructure with large grains generally displays poor cohesive strength compared with a fine-grained microstructure. Thus, the fracture strength of the coating tends to increase with decreasing grain size and thickness.

When wear particles are released, the tribological behaviour of the system is affected. Hard surfaces typically produce small wear particles with weaker agglomeration tendency. Experimental evidence shows that the introduction of small hard particles into a sliding contact does not always imply a more severe tribological contact.

If the mating surfaces have high rugosity (or worn surfaces form with high rugosity during the sliding), the particles can hide inside the valleys formed by the asperities. They will have no great effect neither on friction nor on wear, provided that their dimension is of the same order than asperity height. Particles with dimension exceeding the asperities height and with higher hardness than the surfaces will cause ploughing and scratching. These scratching particles will carry indeed part of the load and concentrated pressure peaks arise while they try to penetrate the surfaces. The high-pressure peaks may well be the origin of crack nucleation in the coating. With regards to the latter scenario, it is clear that thin coatings are not particularly suitable for applications with high-stress abrasive because of their high brittleness.

On the contrary, reduced roughness surfaces can experience increasing friction and wear as the particles cannot but interact with the surfaces by scratching and interlocking. A special case is when hard enough

particles with fairly round shape are interposed between smooth surfaces and act as rollers reducing the friction.

If the particles in the contact for some reasons are soft or characterised by some lubricity (as the oxides/hydrated oxides particles are), then their tribological effect is quite different. Soft particles with low shear stress trapped in the contact can carry part of the load and inhibit the direct contact of hard surfaces, thus reducing both wear and friction.

In the situation of a hard slider moving over a hard surface, the overall contact stress is lower than the yield stress of the contacting materials and the contact is elastic. Nevertheless, asperities of ceramic materials may deform plastically because the compressive load at the small contact areas is much higher. High localized contact stresses can generate dislocations and pile-up of dislocations even in brittle materials and eventually crack nucleation beneath the surface. These cracks grow by coalescence in a plane parallel to the surface and a loose particle eventually forms as described by Suh in his delamination theory of wear. The delamination particles are flake-like and may be some hundred micrometres long.

9 SETUP AND MATERIALS

The study on the tribological procedure for hard coatings was performed on a selected hard coating that nowadays is commonly used in many industrial applications: the TiN coating. Titanium Nitride is a ceramic compound largely used to reduce wear and improve surface slip in particular dry contacts as those of cutting tools and certain bushings.

Several round steel samples with a micrometric layer of TiN on the top were tested against spheres of different dimensions and materials. The ceramic material was applied on the steel substrate through the Physical Vapor Deposition (PVD) technique. Samples were produced by Oerlikon Balzer AG.

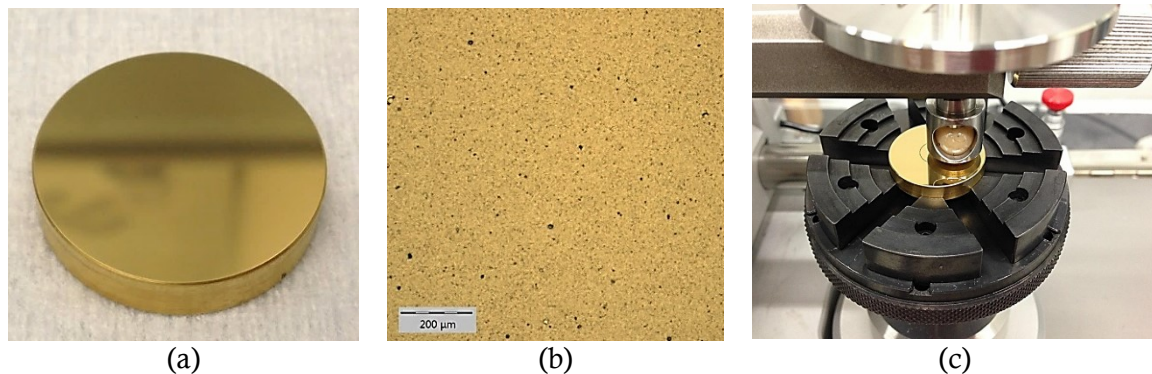


Figure 9.1. (a) A TiN sample; (b) TiN surface appearance under the optical microscope (10x); (c) Experimental set-up

Table 9.1. Measured values of coating hardness and thickness

	Average coating hardness HV0.025 [kgf/mm ²]	Average coating hardness [GPa]	Average coating thickness [μm]
Sample for test 1	654.7	6,421	1.85
Sample for test 2	472.3	4,632	1.69
Sample for test 3	634.1	6,219	1.89
Sample for test 4	474.1	4,650	1.73
Sample for test 5	482.4	4,731	1.80
Sample for test 6	564.6	5,537	2.00
Sample for test 7	814.9	7,991	1.88
Sample for test 8	523.9	5,138	1.66
Sample for test 9	533.1	5,228	1.75
Sample for test 10	514.6	5,046	1.73
Sample for test 11	590.5	5,791	1.73
Sample for test 12	491.1	4,816	1.70
Sample for test 13	555.7	5,450	1.72
Sample for test 14	553.6	5,429	1.69
Mean value	561,40	5,51	1.77
Standard deviation	88,77	0,87	0.09
Standard deviation [%]	15,81	15,81	5.28

The thickness of the ceramic film was checked experimentally by means of the Anton Paar CAT²c calotest machine presented in Sec.3.3 and found to be $1.77 \mu\text{m} \pm 0.09 \mu\text{m}$. The value is in line with the technical data provided by the manufacturer who declared a range from 1 to 4 μm. The hardness was

measured experimentally as well resorting to microhardness tester described in Sec.3.3. Detailed values of these material properties for each sample are listed in Table 9.1. In both the cases measurements were taken in the central part of the samples, as that region of the surface is unused for pin-on-disc tests.

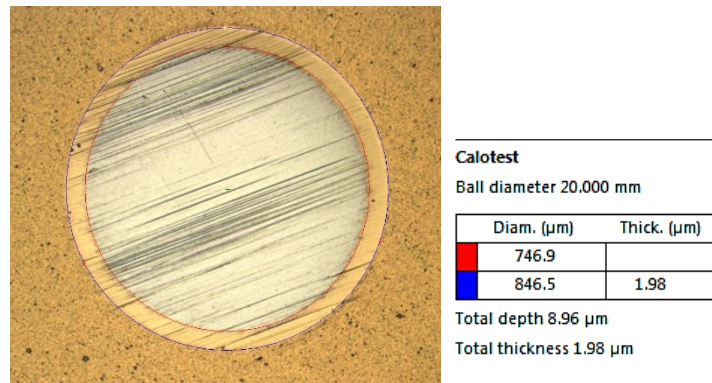


Figure 9.2. Example of thickness measurement after a ball crater test

It should be noted that Vickers microhardness value for TiN are usually around 2300HV, very different from those measured. It is likely that substrate played a role during indentation, maybe due to the combination of the relatively high indentation load (25g) and the small thickness of the ceramic layer. However, lower loads made it difficult to calculate the hardness as the indentation footprint was blended into the surface porosity (see Figure 9.1a). In future other methods should be resorted to, for example instrumented nano-indentation. Even if probably no valid, these values were used all the same as they can still represent the relative variability in terms of surface hardness among the samples.

The main properties of the samples and the different kinds of spheres tried out during experiments are listed in Table 9.2. As recalled in Sec. 5, in a standard pin-on-disk tester the sphere is the static partner and the flat sample is the moving partner, i.e. the one mounted on and driven by the spindle.

Table 9.2. Material properties

	Material	Number	Average Young modulus [GPa]	Roughness R_a [μm]	Diameter [mm]
Sphere	Alumina (Al_2O_3)	1	370	-	6
		2		-	10
	Tungsten carbide (WC)	1	680	-	6
		1		-	10
	100Cr6 Steel	1	210	-	10
Sample	Titanium Nitride (TiN)	19	600	0.023 ± 0.004	25

The experimental study was organised in two phases. The first phase consisted in the preliminary feasibility study for a procedure of this kind. A broad tribological characterisation of the selected compound was performed by testing different configurations, materials of the sphere and parameters to identify the best conditions for this purpose. As already stated in the introduction to this dissertation, the idea was to use lighter loads and faster speeds than those proposed by the original ILS that is part of the actual release of the ASTM G99 standard. Numerous combinations of load ranging from 1N to 6N and linear speed ranging from 0.1m/s and 1m/s were tried out exploring different radial positions on samples. In addition, three further features of the friction curves of paramount importance were considered:

- the presence of a clearly visible transition between the on-coating run and on-substrate run;
- the stability of the coefficient of friction before and after the coating failure;

- a satisfactory repeatability of the friction curve shape and of the mean value of the coefficient of friction.

In the second phase, a potential optimum combination of testing parameters was repeated several times. Table 9.3 provides an overview of the chosen parameters. A new sample was used for every repetition so as to keep the radius of the track constant.

Table 9.3. Optimum testing parameters

Repetitions	Valid repetitions for the wear volume	Sphere	Load [N]	Speed [m/s]	Duration [m]	Track radius [mm]	Average Temperature [°C]	Humidity [%]
14	5	10mm Al ₂ O ₃	1	0.1	Variable	4.2	29	30 to 45

A great deal of attention was paid to avoid any kind of chemical and physical contamination of the sample surfaces. Latex gloves were worn before handling samples and every other tool. The entire equipment was periodically cleaned with chemical pure acetone and isopropyl alcohol (IPA). The sample and the ball were cleaned by immersion into IPA before starting each test and wiped with lint-free tissues.

10 EXPERIMENTAL RESULTS

10.1 PRELIMINARY TESTS

The first part of the investigation covers more than ... tests, too many to be all displayed in this section. What follows is a tiny piece of such an amount of data since the author's purpose is just to outline what was the process of assessment of the proper value for each testing parameter.

First, and so as to have a background condition to start the investigation, the same parameters adopted by the original ILS (10N load and 0.1m/s) were checked. Figure 10.1 shows the results obtained with a 10mm 100Cr6 steel ball and a 10mm Al_2O_3 ball, two materials used in the ILS in above. In both cases, the track radius was 8.5mm.

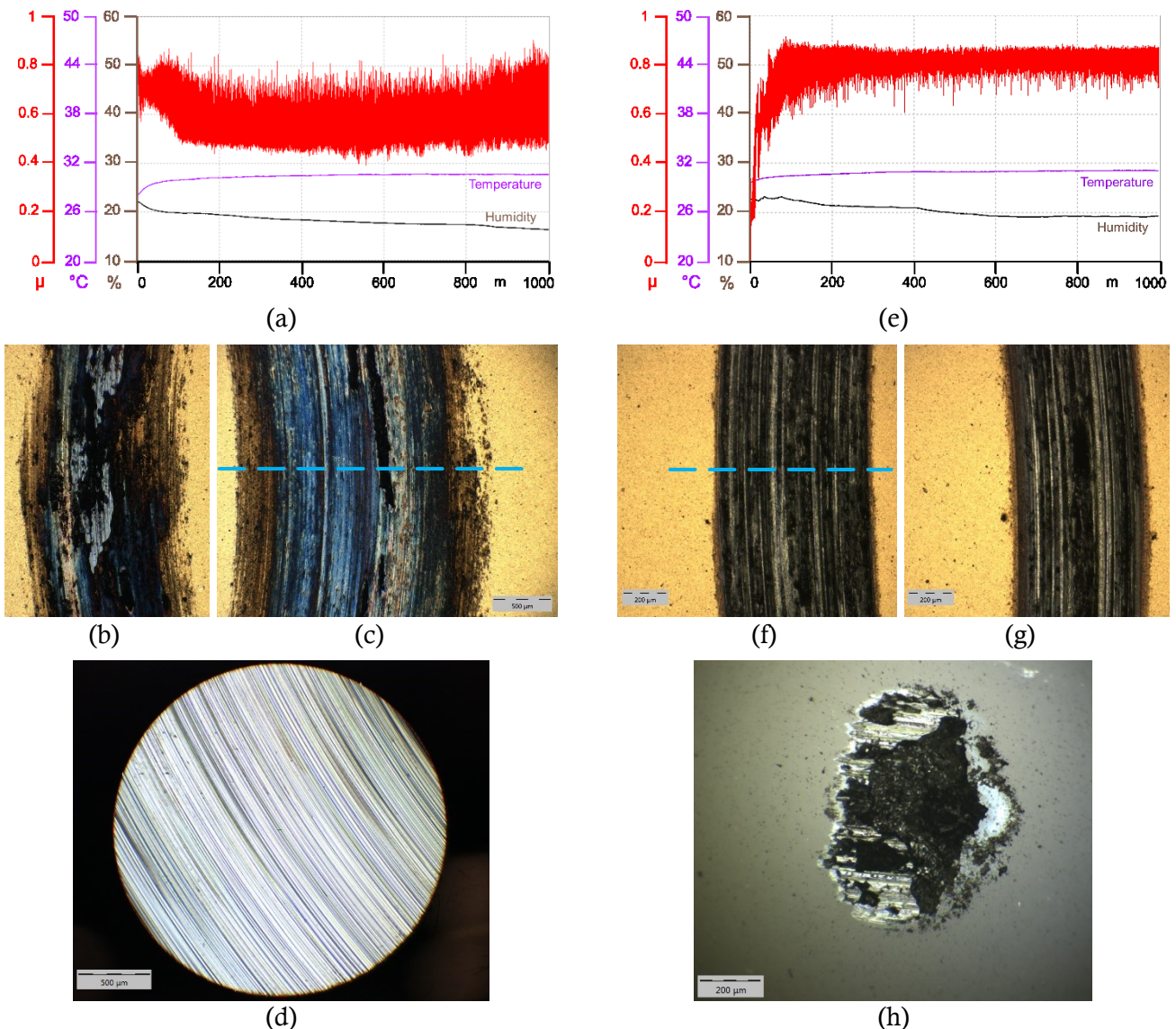


Figure 10.1. 100Cr6 steel ball: (a) Friction curve; (b) and (c) microscopy of the wear track in diametrically opposed position; (d) worn cap on the sphere. Al_2O_3 ball: (e) Friction curve; (f) and (g) microscopy of the wear track in diametrically opposed position; (h) worn cap on the sphere.

Figure 10.1 indicates that none of those conditions is viable to characterise the coating. If a steel ball is used, no wear scar appears on the sample, as the stylus profilometry in Figure 10.2a reveals. Wear is localized on the sphere (Figure 10.1d) because its hardness is much lower. The large black trace of Figure 10.1b and Figure 10.1c is nothing but oxidized steel welded on the ceramic surface and the only sign of damage is the presence of deep grooves caused by abrasion phenomena.

Other authors in the literature (e.g. Malliet et al. and Miyoshi [4]) observed the formation of metal films on the coated surface for a TiN coating sliding against a metal counterface. They show that the adhesive wear of the TiN coating is facilitated by the openness of the microstructure and surface porosity. As iron becomes trapped in the open regions of the coating microstructure, it increases the adhesion at these positions. This may explain the high CoF measured within the first 100m. After some sliding, a transferred layer made of deformed, oxidized and agglomerated fragments built up. Friction tends to decrease as this thick transfer layer (in light grey in Figure 10.2b) grows on the surface, because of the lubricating effect of the oxides. In the last part of test friction comes back to grow weakly as a result of the contact region enlargement. Also the occurrence of grooves and ploughing was reported by other authors in the scientific literature, e.g. Sue and Troue and Miyoshi [4].

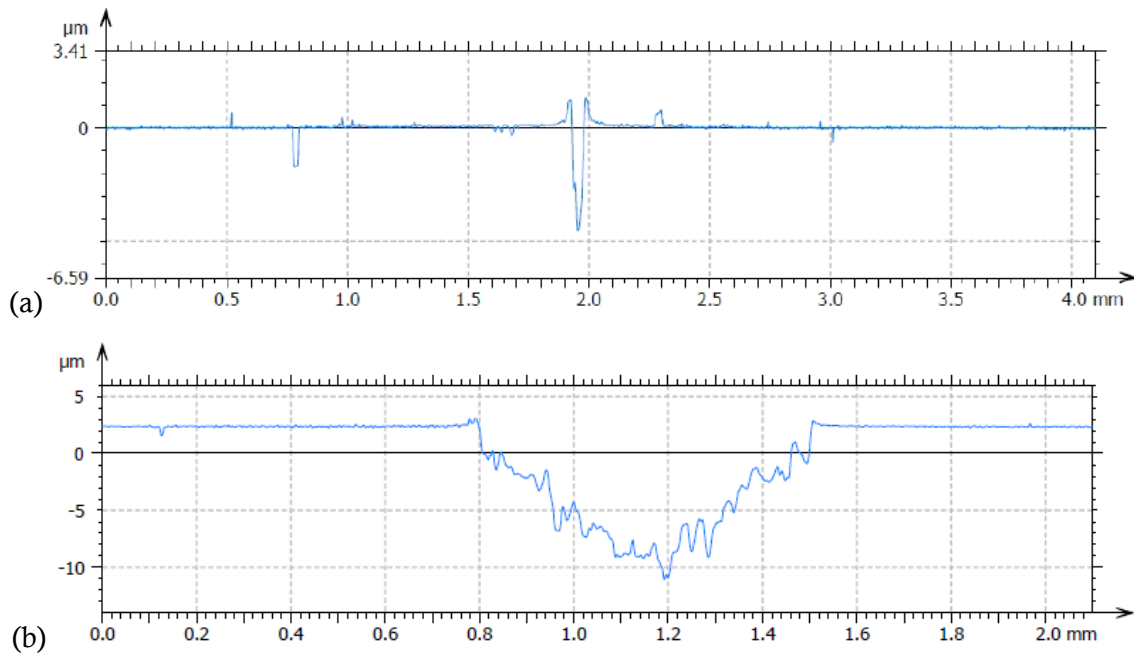


Figure 10.2. (a) Stylus profilometry corresponding to the path in Figure 39d; (b) Stylus profilometry corresponding to the path in Figure 39f

In case of alumina ball, a uniform wear track is gouged, and the TiN layer is completely removed as the hardness of the sphere is higher this time. The black appearance is linked to the oxidation of the substrate; Figure 10.2b shows indeed that the maximum depth of the wear scar is far larger than the average thickness of the coating. The friction curve is rather stable, but the removal of the coating is too fast and almost all the test runs on the substrate.

Now, it becomes clear that such parameters have to be changed. On the one hand, Steel revealed itself the wrong partner and, on the other hand, the aggressive action of alumina suggested to try an alternative material with hardness in between. Tungsten carbide was then selected. In the following the impact of the change of each parameter on the behaviour of the system is analysed on its own, letting other parameters, which are not yet established, to change.

Starting with load, Figure 10.3 to Figure 10.7 clarify why loads higher than 1N are impracticable. All the curves disclose an early perforation of the coating after the wear-in ramp and lack a well recognisable transition phase from the on-coating run to the on-substrate run. Except the case in Figure 10.6, the failure of the coating is strongly non-uniform: along the same track areas where coating is totally worn out coexist with areas where coating is still there. Furthermore, the combination of high load and high speed has the primary effect to enhance the dynamics by increasing the kinetic and potential energy content of the system. Consequently, the stability of the measuring arm is undermined and hopping of the pin is common, especially when the coating starts to fail. The reiteration of the impact on the surface of a brittle material induces the nucleation and propagation of sub-surface cracks which make their way towards the surface. Once a crack reaches the surface, a large debris is ejected:

this may explain the occurrence of craters and bumps (e.g. Figure 10.5 and Figure 10.7) that are sources of high noise and banging.

As soon as these circumstances are met, the test is invalidated because the test rig begins to influence too much the tribological result. The test in Figure 10.6 differs from the other since the speed is considerably lower. The features of the wear scar are the most desirable; the same cannot be said for the friction curve.

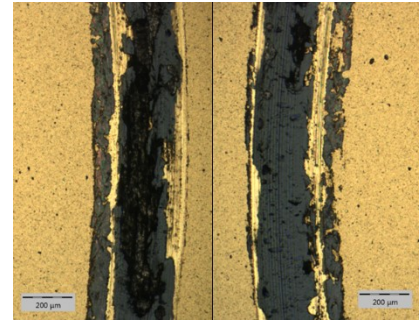
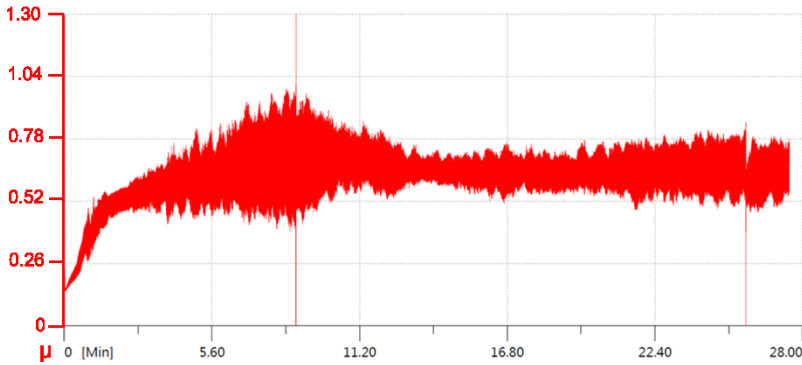


Figure 10.3. Discarded test: 6N, 6mm radius, 0.5m/s, 6mm WC ball. Friction curve and wear track.

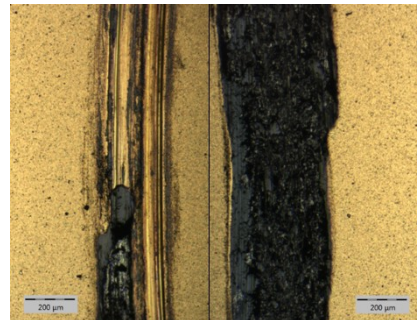
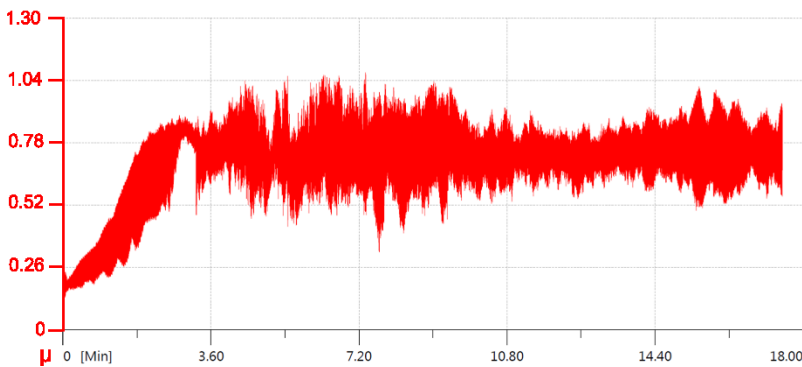


Figure 10.4. Discarded test: 5N, 11.4mm radius, 0.48m/s, 6mm WC ball. Friction curve and wear track.

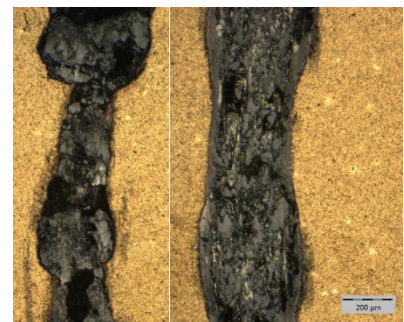
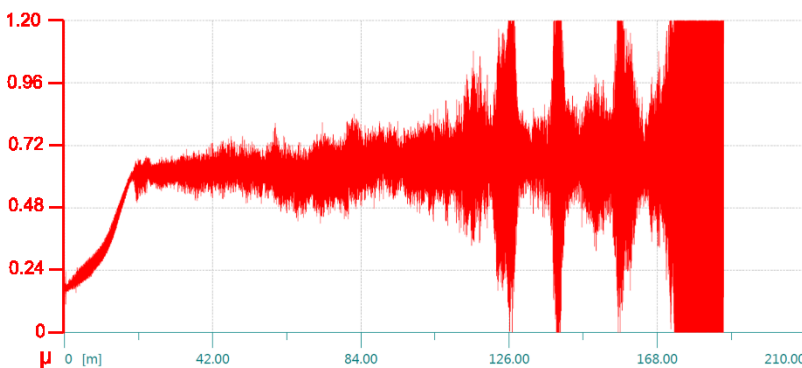


Figure 10.5. Discarded test: 3N, 5.3mm radius, 0.5m/s, 6mm WC ball. Friction curve and wear track.

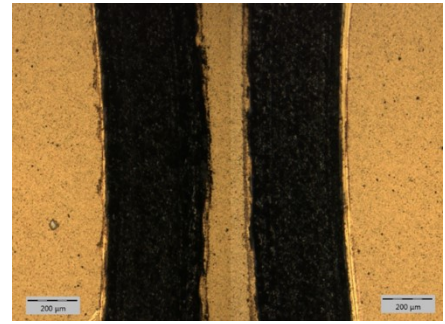
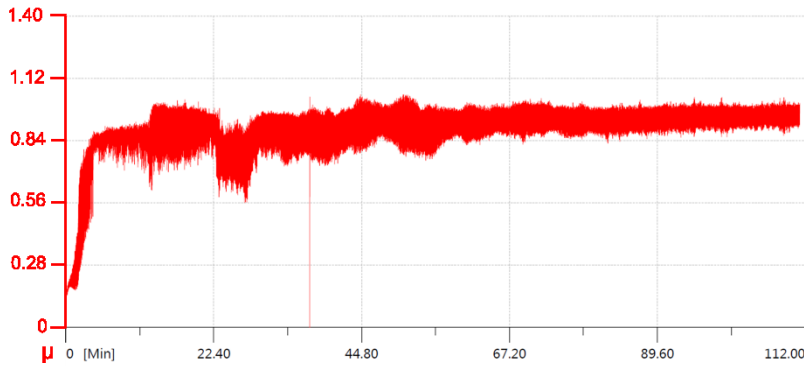


Figure 10.6. Discarded test: 3N, 7mm radius, 0.15m/s, 6mm WC ball. Friction curve and wear track.

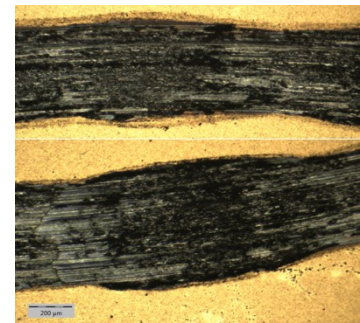
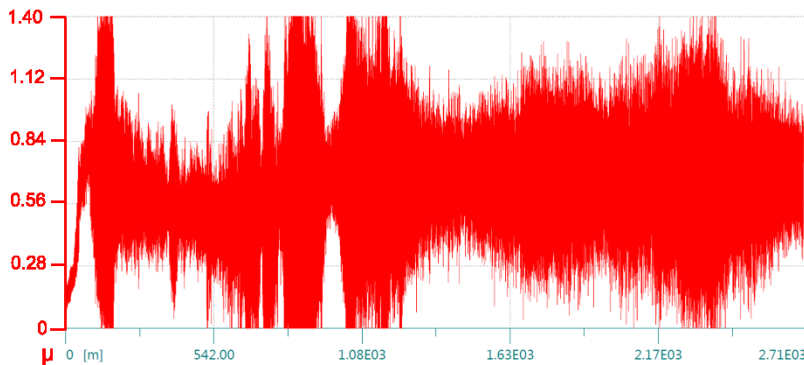


Figure 10.7. Discarded test: 2N, 10mm radius, 1m/s, 6mm Al₂O₃ ball. Friction curve and wear track.

As to *speed*, similar remarks on dynamics as those for load apply, even though the load is limited to just 1N. Strong non-uniformity of the wear scar and irregular perforation of the coating layer cannot be avoided if speed is faster than 0.1m/s (see for example Figure 10.8 and Figure 10.11). Figure 10.10 represents an acceptable result in terms of friction curve. Two main issues come with this test anyway. Despite the stable mean value of the coefficient of friction in the ending part of the test, the transition phase from coating to substrate had not been completed yet. Secondly, this condition was proven to be non-repeatable during later attempts with the same parameters.

These remarks underline a great limit of the pin-on-disc layout: dynamics can deeply affect the results because of the specific mechanical layout of the test rig itself. This is perfectly consistent with what was said about *model tests* in the introduction to this paper. Model tests are not intended to reproduce actual tribological condition of industrial applications. They are simple (or simplified) but a higher level of abstraction is unavoidable as a drawback.

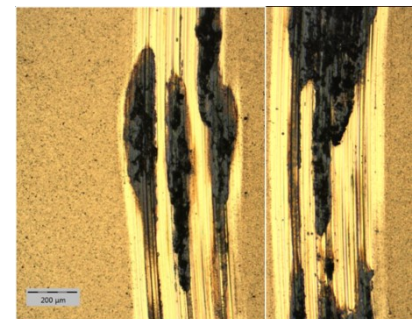
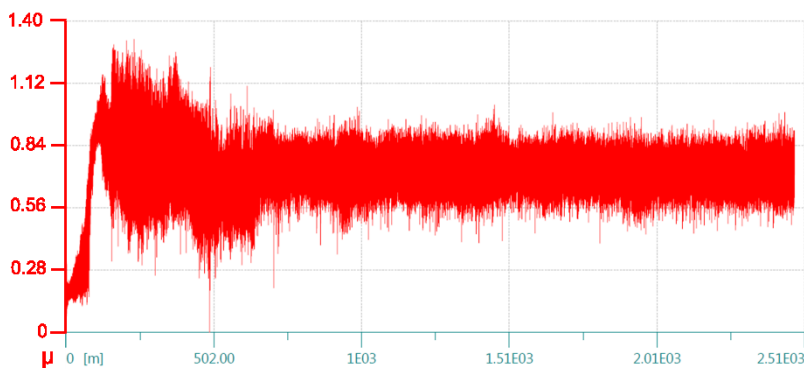


Figure 10.8. Discarded test: 1m/s, 1N, 11.2mm radius, 10mm Al₂O₃ ball. Friction curve and wear track.

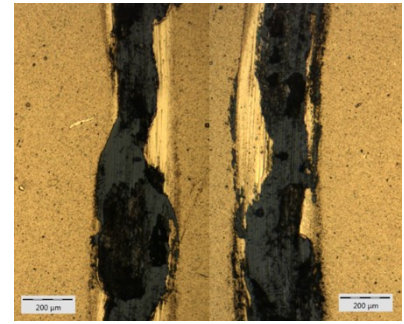
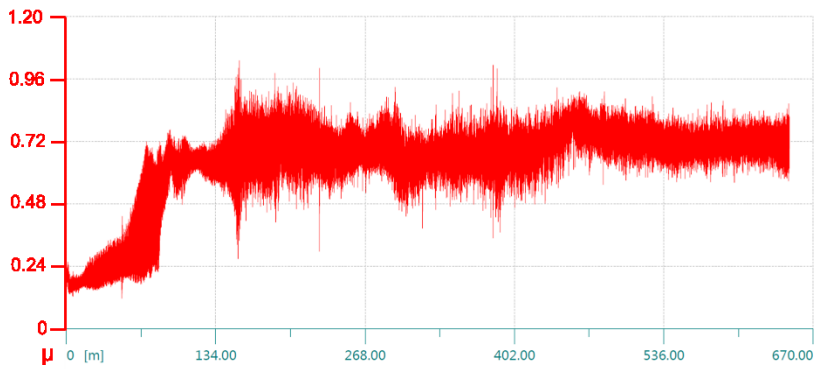


Figure 10.9. Discarded test: 0.67m/s, 1N, 6.7mm radius, 10mm WC ball. Friction curve and wear track

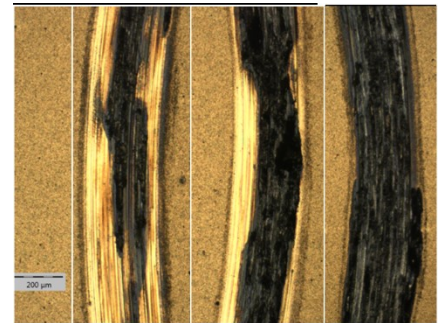
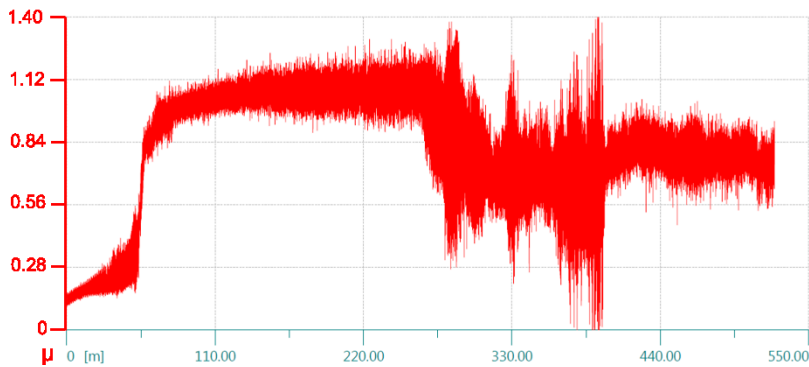


Figure 10.10. Discarded test: 0.5m/s, 1N, 5.2mm radius, 10mm WC ball. Friction curve and wear track

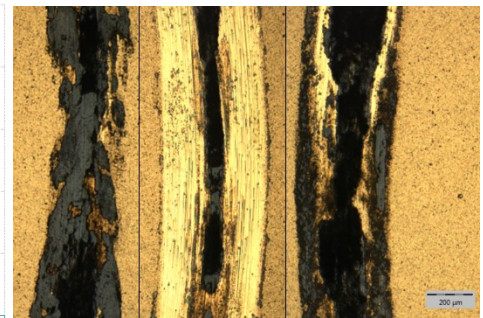
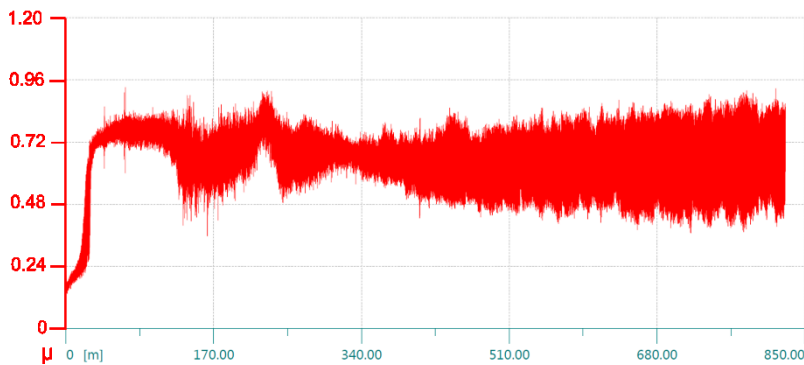


Figure 10.11. Discarded test: 0.5m/s, 1N, 5.2mm radius, 10mm WC ball. Friction curve and wear track.

Now, the only one parameter left free is the material of the sphere. Figure 10.12 and Figure 10.13 show two tests carried out with the previously fixed values of speed and load and running with a WC ball. Inspection of the wear scars points out that WC can damage the hard layer, although it is not able to entirely remove it, at least within a reasonable duration of the tests. Besides, there was evidence of a grey transfer layer welded onto the track that would probably grow as the interaction would go forward. The presence of this protective layer might downright prevent the coating from failing.

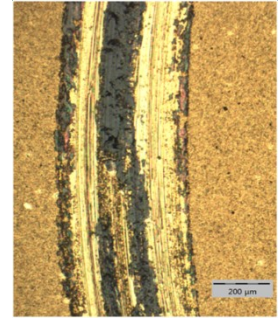
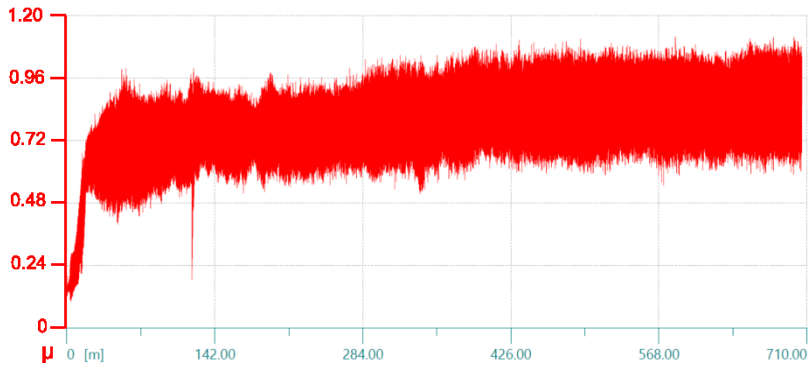


Figure 10.12. Discarded test: 6mm WC ball, 0.1m/s, 1N, 4.75mm radius. Friction curve and wear track.

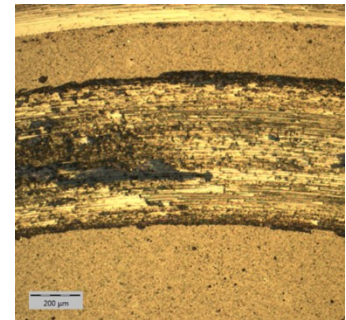
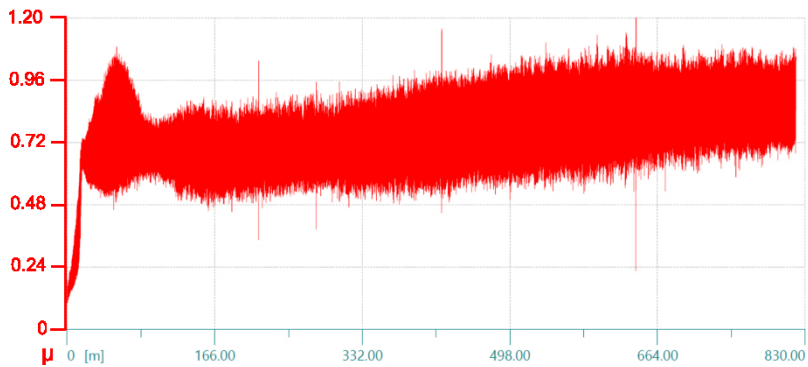


Figure 10.13. 10mm WC ball, 1N, 0.1m/s, 4.5mm radius. Friction result and wear track.

10.2 REPETITIONS WITH OPTIMUM PARAMETERS

The analysis of preliminary results set out in the previous section allowed to identify the optimum parameters for the second part of the investigation. Table 10.1 summarises the results of each of the 14 repetitions according to ASTM G99 guidelines. It is clear how this representation of results is totally inadequate for a coated system: no relevant information on the behaviour are contained.

Table 10.1 Summary of the results of the tests with optimum parameters

	COF Maximum value	COF Minimum value	Duration [m]
Test 1	0.948	0.212	450
Test 2	0.904	0.156	530
Test 3	0.937	0.220	465
Test 4	0.906	0.211	375
Test 5	0.927	0.237	400
Test 6	1.015	0.165	600
Test 7	0.924	0.240	465
Test 8	0.892	0.197	450
Test 9	0.914	0.194	350
Test 10	0.888	0.219	350
Test 11	0.900	0.175	350
Test 12	0.907	0.210	350
Test 13	0.896	0.223	350
Test 14	0.899	0.187	350

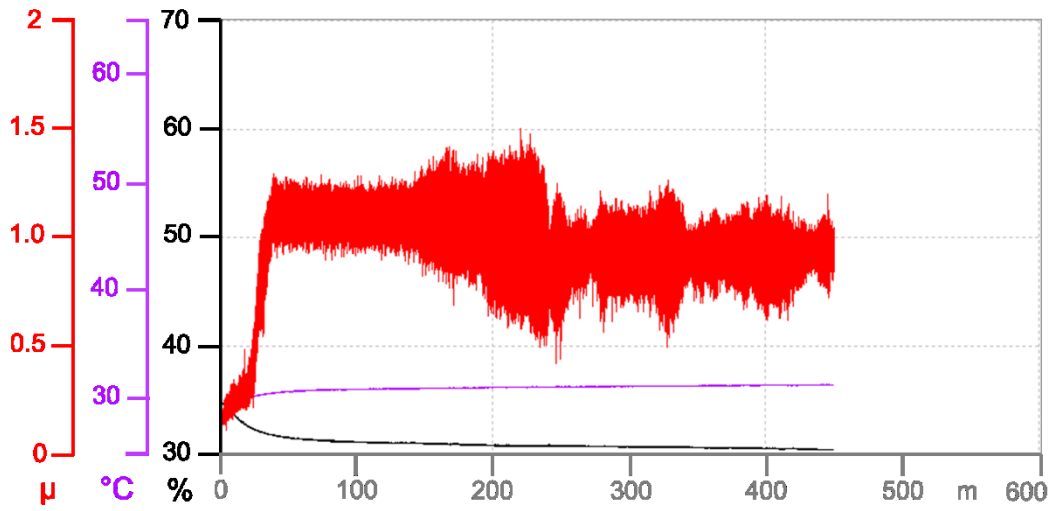


Figure 10.14 Test 1: rough friction curve

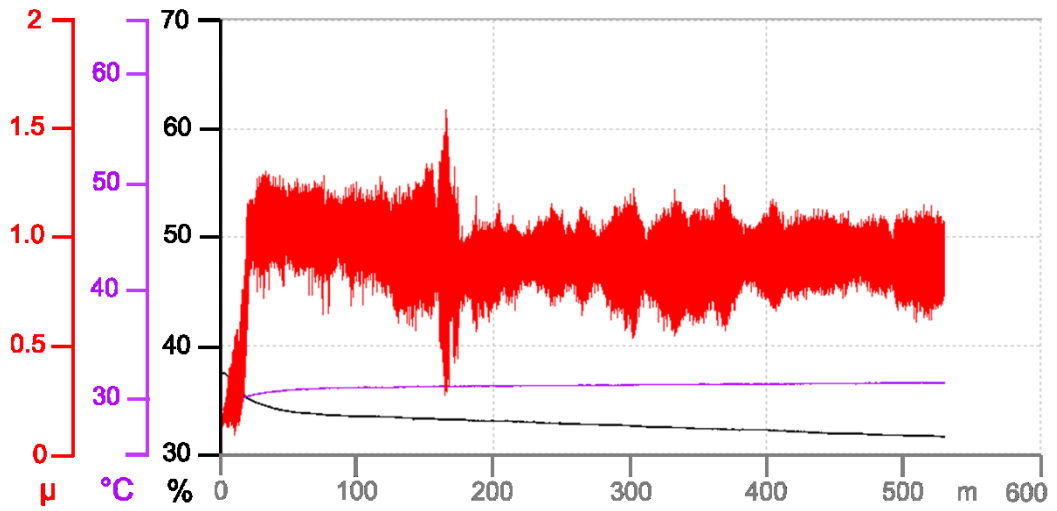


Figure 10.15 Test 2: rough friction curve

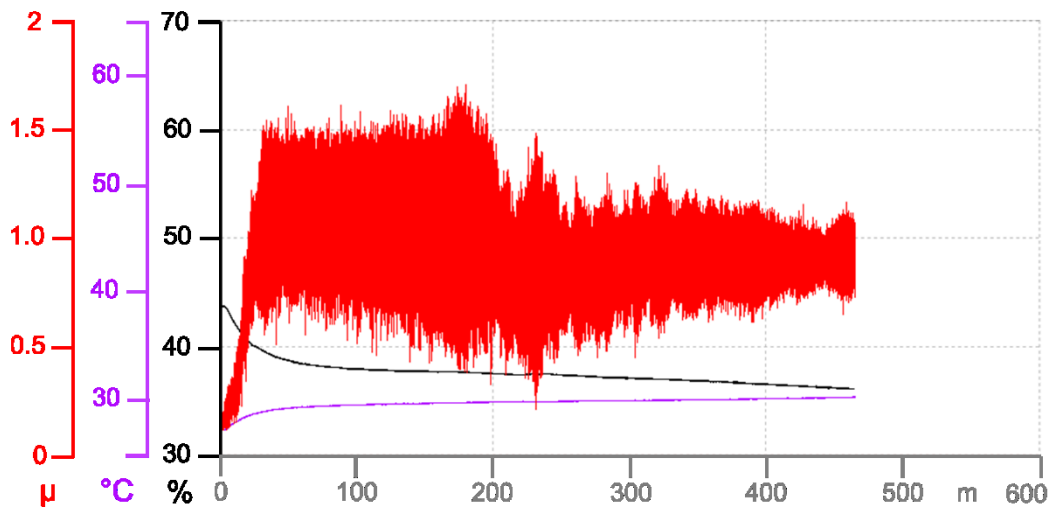


Figure 10.16 Test 3: rough friction curve

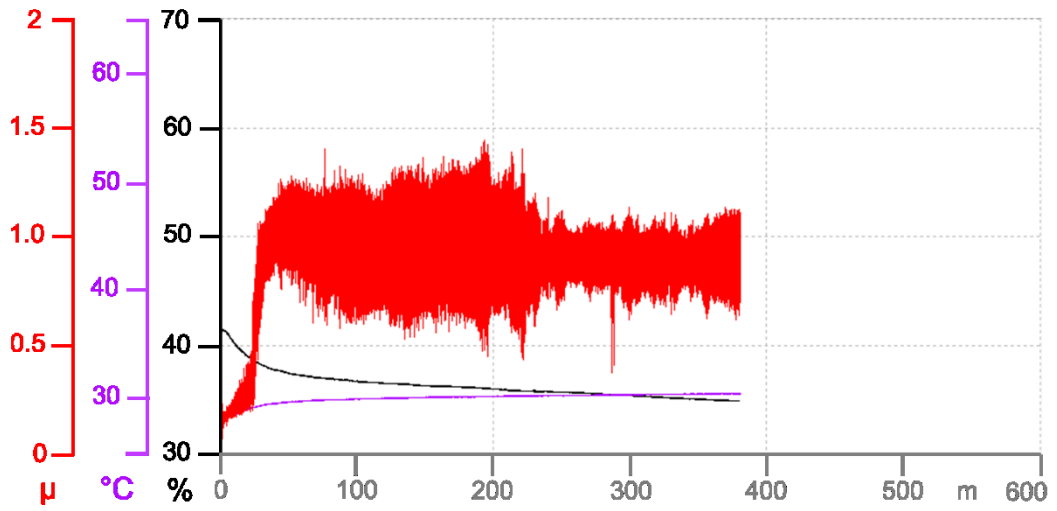


Figure 10.17 Test 4: rough friction curve

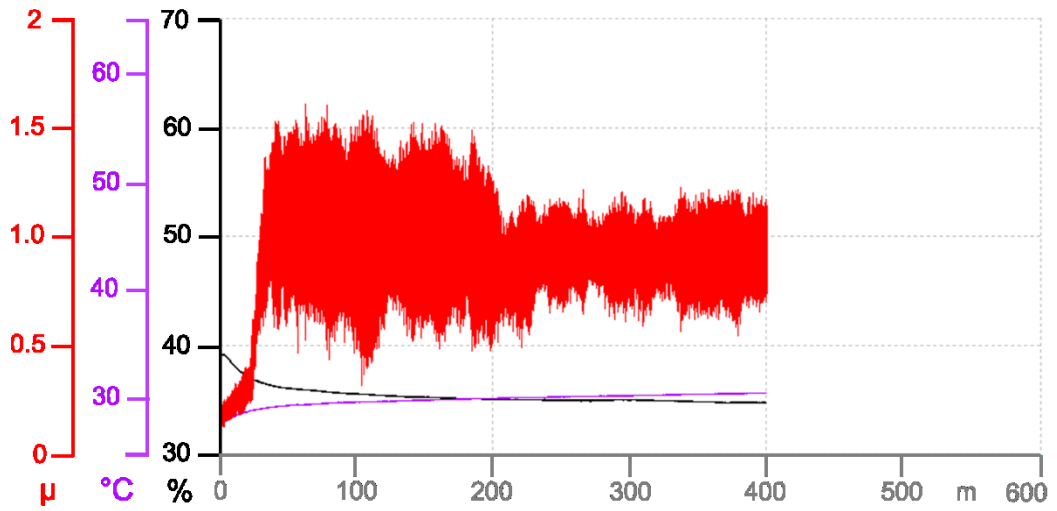


Figure 10.18 Test 5: rough friction curve

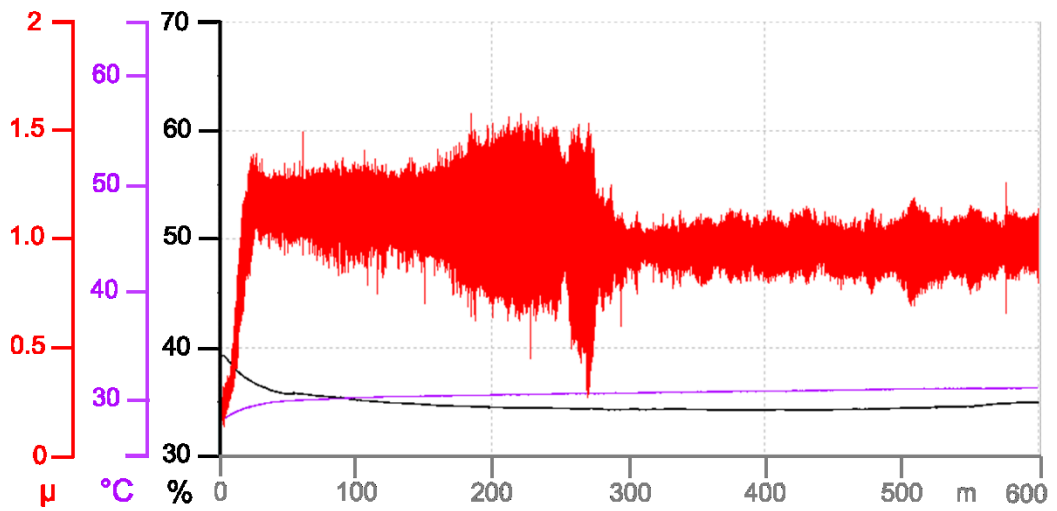


Figure 10.19 Test 6: rough friction curve

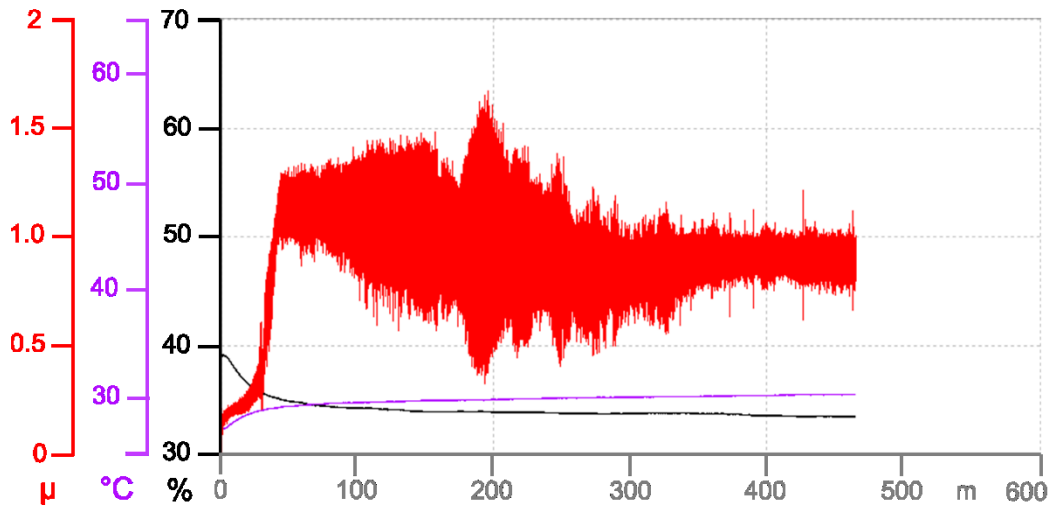


Figure 10.20 Test 7: rough friction curve

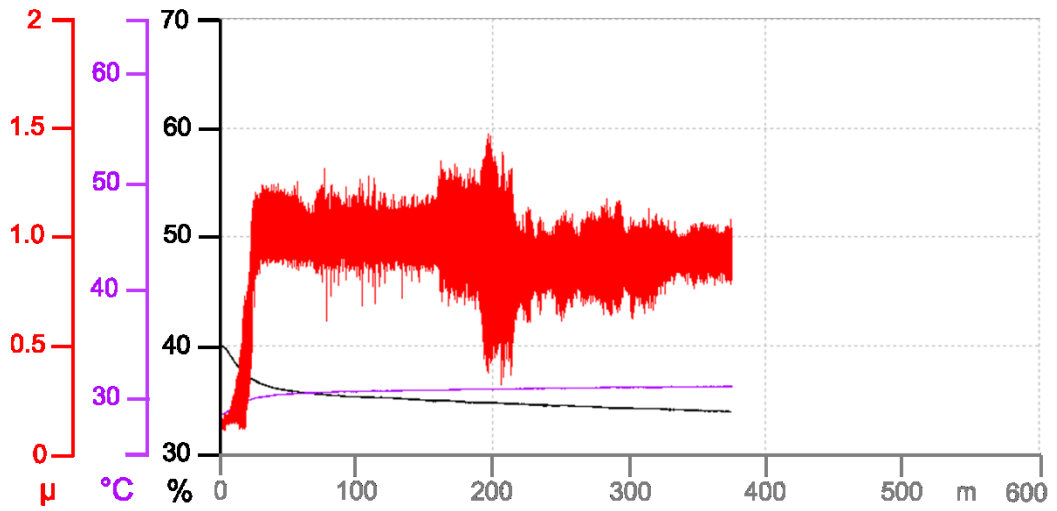


Figure 10.21 Test 8: rough friction curve

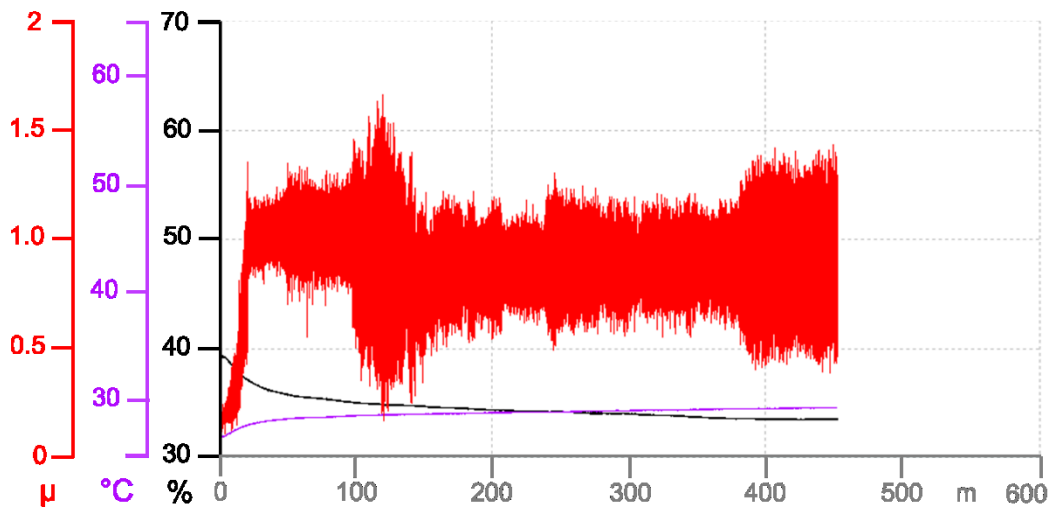


Figure 10.22 Test 9: rough friction curve

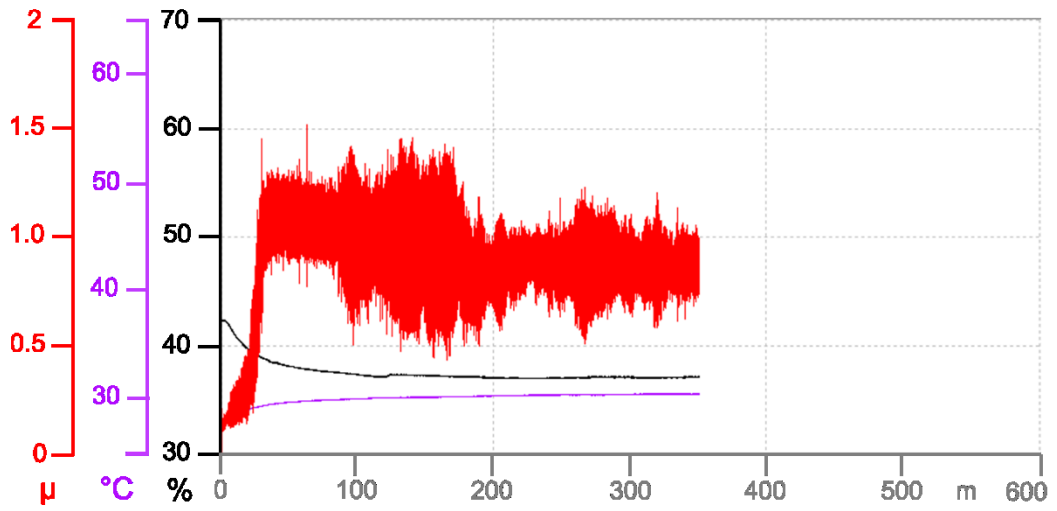


Figure 10.23 Test 10: rough friction curve

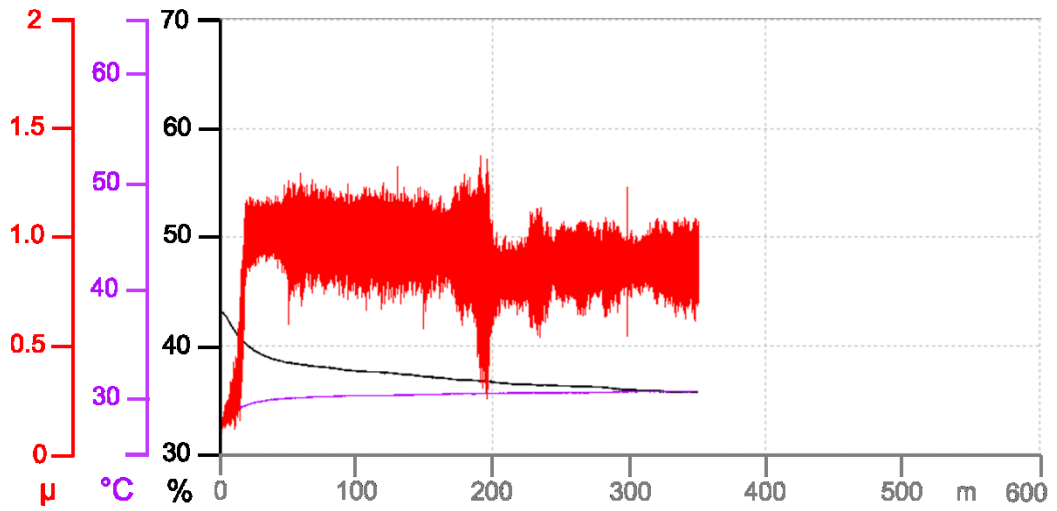


Figure 10.24 Test 11: rough friction curve

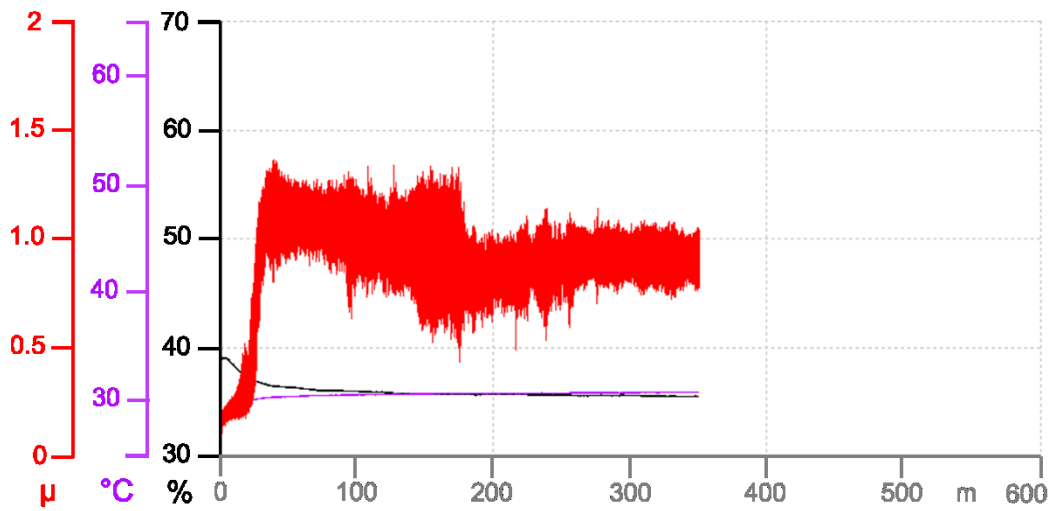


Figure 10.25 Test 12: rough friction curve

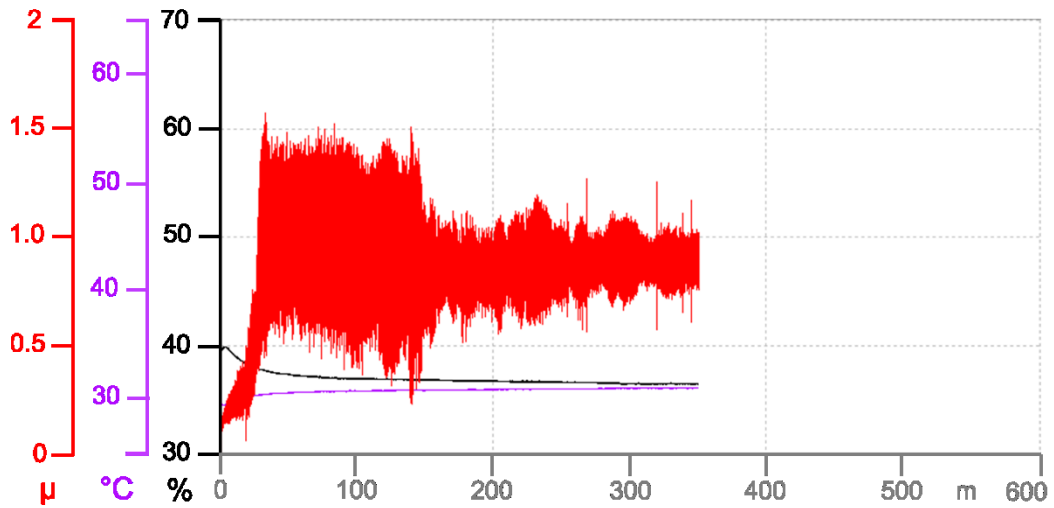


Figure 10.26 Test 13: rough friction curve

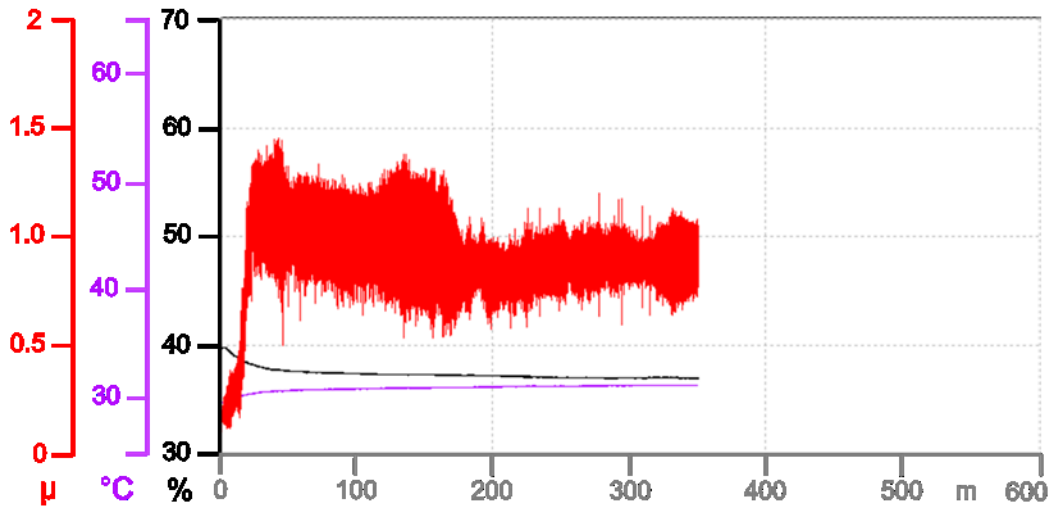


Figure 10.27 Test 14: rough friction curve

As to the wear volume, the inspection of the alumina balls under the microscope suggested to overlook its loss of material, as neither flat nor circular worn cap were there (Figure 10.30b). Under the assumption of ‘no significant pin wear’ [7], the total wear volume of the system is disk wear only.

The total amount of material removed from the disk was calculated according to ISO 18535:2016. The wear scar profile was measured in four different locations at 90° to one another with the Taylor-Hobson profilometer presented in Sec.3.2.

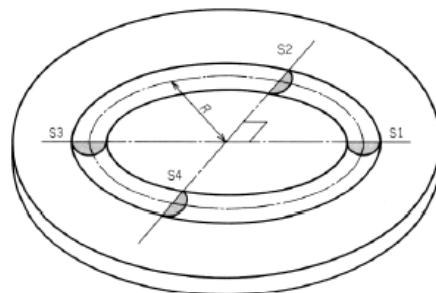


Figure 10.28. Wear volume measurements according to ISO 18535:2016.

Data were analysed with the software TalyProfile Gold® v7.2. By integrating each profile, the corresponding track cross-section area was calculated (an example is given in Figure 10.29). The average area value was multiplied by the average track length to eventually obtain the total wear volume.

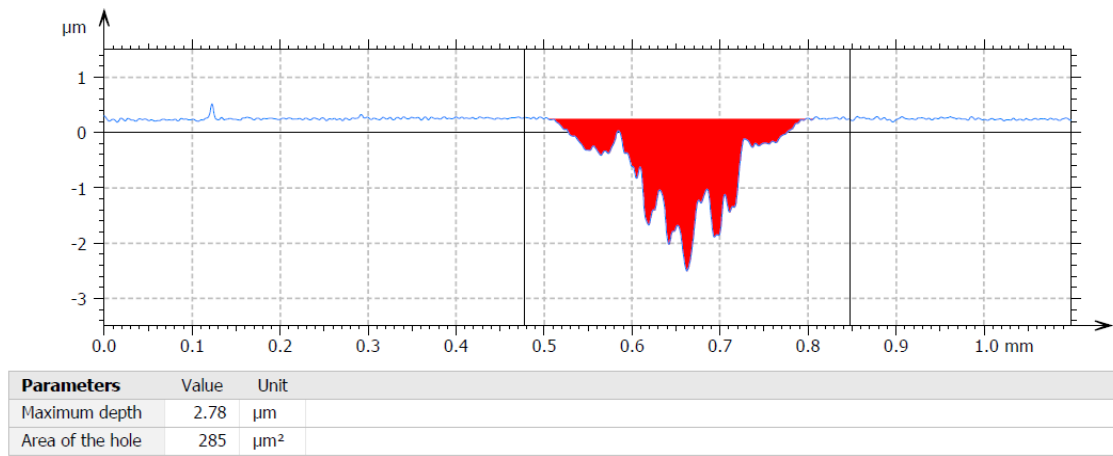


Figure 10.29 Example of wear scar profile with measurement of the track cross-section area

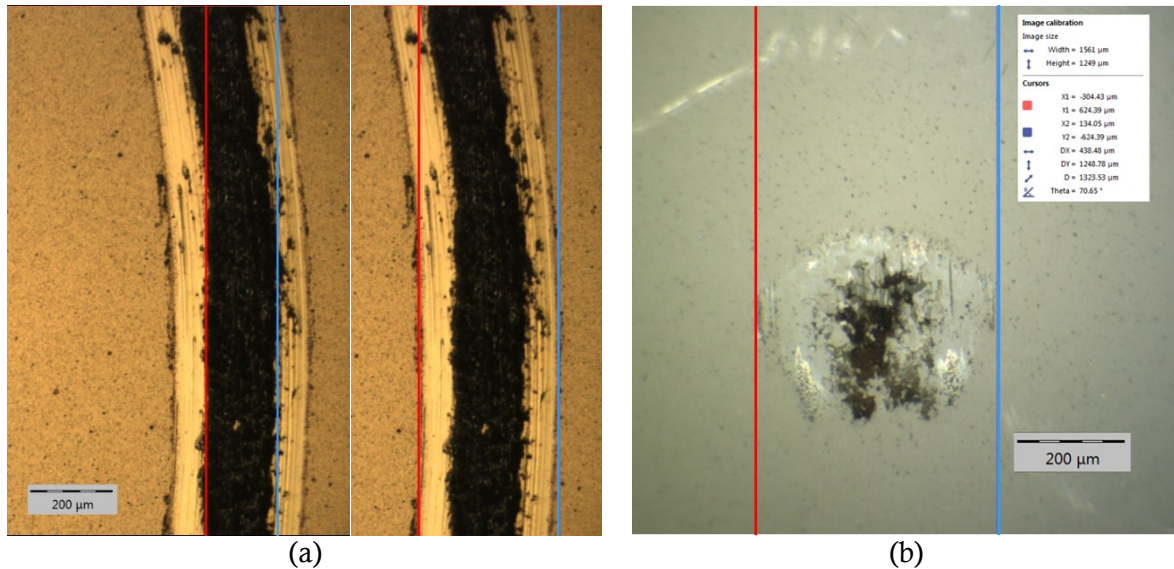


Figure 10.30 Optical microscopy (10x) and measurement of (a) the wear scar; (b) the wear trace on the alumina ball. Total wear track is 327 µm wide; wear track on substrate is nearly 170 µm wide; ball wear trace 438 µm wide.

11 DISCUSSION OF THE RESULTS

Despite the original wish was to characterise the coating in high speed conditions, the extended investigation on the tribological behaviour of TiN made it clear that high speed conditions were not suitable, at least for the pin-on-disk configuration.

Emphasis was put on the fact that the parameters here identified as optimum were very similar to ISO 18535:2016 standard for DLC-like films. This latter standard suggested [8] to use 0.1m/s and 3N or 5N depending on the purpose of the test. Anyway, it concerned low speed and moderate load in order to reduce detrimental dynamic effects during the test. The use of a higher load was justified by the fact that DLC is much harder than TiN and it has an excellent resistance to wear action; lower load would not allow any significant wear track to appear.

The most surprising feature of these curves was the evolution of the COF from coating to substrate. Contrary to what was expected, the mean friction value is higher in the first part of the test (when the ball was in contact with the TiN) and decreases in the second part. Such a situation is completely different from what was observed during the preliminary test. Recalling Figure 10.1, the coefficient of friction stays around 0,6 as long as the coating resist (few meters); once the film fails friction grows and stabilises beneath the value of 1. The difference makes you realize that the wear and friction mechanisms vary a lot merely by changing the applied load, evidently.

TiN is primarily an anti-wear coating and, in general, shows low lubricity and low anti-sthick. It usually exhibits ant-friction properties in sliding against itself [4]. In accordance to the theory in Sec. 8.4, the function of the coating is to separate the substrate from the counterface and to prevent ploughing thus reducing both the friction and the wear. At the same time, the hard layer introduces a higher shear strength at the contact interface with an increasing effect on friction in sliding if no microfilms are formed. This can explain the very high coefficients of friction which often occur in sliding contacts of thin hard coatings [4].

By comparing the rough curves of the coefficient of friction displayed in Figure 10.14 to Figure 10.27, a fairly good repeatability of the results is obtained and similar features emerge. Four phases emerge during the tribological interaction:

- 1) A *wear-in* phase takes up the first 50m of test. The coefficient of friction evolves from at a value of about 0.2 and quickly stabilises at about 1 - 1.1.
- 2) A *first steady-state* period corresponding to the on-coating run, let us call it. The shape of the curve is here regular and the scattering of the local values of the coefficient of friction may be higher than elsewhere.
- 3) A *transition phase* of variable length which lessens the coefficient of friction towards a new stable mean value. The behaviour of the system is often characterised by a transitory increase of the curve noise, i.e. a larger scattering of the coefficient of friction values.
- 4) A *second steady-state* period corresponds to the on-substrate run which persist until the stop of the test. The curve is, on average, thinner but unregular.

These phases are outlined schematically in Figure 11.1, resorting for better understanding to the friction curve from test... after a filter has been applied to reduce noise. The first two phases are merged in one phase called *coating lifetime*. This latter represents the portion of the test during which a continuous layer of coating insulated the substrate from the ball.

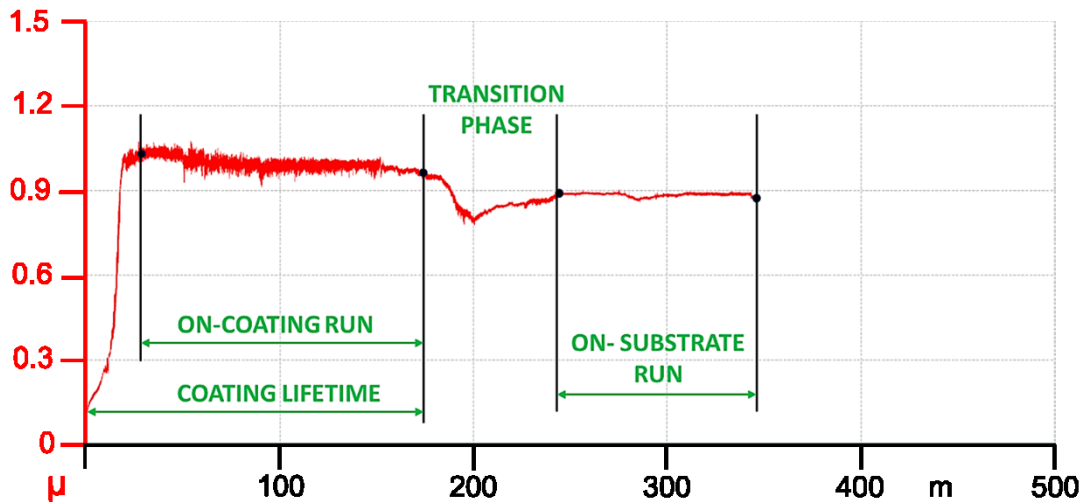


Figure 11.1 Schematic representation of the tribological phases during a test run

The wear-in phase is in turn subdivided into two subperiods. In the very beginning the value of the coefficient of friction stays low and increases with a moderate slope. The trend suddenly changes after 10 to 30 meters and the value peaks with a steep ramp covering few meters. This transitory phase which experiences a fivefold increase of friction comes to its end when the coefficient stabilises at $1 \div 1.1$. Interestingly, as soon as the ramp wanes with debris of TiO_2 usually appear at both side of the wear track. It probably means that the severe abrasion becomes the predominate tribological mechanism, as the strong increase in CoF also suggests.

During the first steady state (herein referred to as *on-coating run*) the wearing out of the ceramic coating takes place. It has a duration that is variable from test to test as it correlates to the unavoidable variability in the ceramic layer properties from sample to sample. The friction curve has a linear silhouette, Figure 10.23, Figure 10.25 and Figure 10.27 being exceptions. The interaction between the ball and the surface is smooth and quiet, just a low-intensity whistle may arise.

The transition phase comes out to be rather inhomogeneous: its duration as well as the tribological behaviour varies from test to test. For the sake of the analysis, two recurrent behaviours can be recognised. In some cases, the transition phase ceases in a short time; the changeover from on-coating to on-substrate period is rather sharp and coupled with localized increases of vibrations and noise of the curve. In Figure 10.15, Figure 10.21, Figure 10.22, Figure 10.24 and Figure 10.25 this mode is flagrant. In some other cases the changeover is gradual and covers a longer time, this time leading to a widespread increase in the noise of the curve. Evidence of this alternative mode is in Figure 10.16, Figure 10.17, Figure 10.18, Figure 10.20, Figure 10.26 and Figure 10.27.

The predominance of one or the other mode depends on how the coating fails. If the rupture sets off in several points along the track at the same time, the first mode is favoured because it does not take long for the ball to reach the substrate everywhere. If, on contrary, the rupture sets off in few locations, longer time is needed until the ball has evenly penetrated the coating.

During the second steady-state period (*on-substrate run*), much higher uniformity is reached: the curve is nearly horizontal, and a new quiet running condition settles in all the repetitions. The sphere is here partly in contact with the substrate and partly with the ceramic film, as Figure 10.30a suggest. The presence of a black area in the middle of the track means that oxidation effects took place and the overall reduction of the COF is in all likelihood due to the lubricating effect of steel oxides.

What said above makes one realize that heterogeneous behaviours and phenomena play a role when testing coated components. If the concern is not limited to study the behaviour of the ceramic film but to characterise the coated system in its entirety, a new specific approach different from both the ASTM G99 standard and the ISO 18535 standard is necessary. The latter fails because it ignores the possibility

that the coating breaks down. The former fails as it recommends a way to analyse the results that is, although very general, unsuited when more than one material is there. For instance, Table 10.1 contains the maximum and minimum value of the CoF for each repetition, as prescribed by the ASTM G99 standard, but these two values are not representative at all. They are both encountered during the very first part of the test, always at the onset of sliding and at the end of the wear-in ramp respectively.

The only way to properly characterise the system is to identify two stable mean values of the CoF: the first one before the coating failure and the second one after the failure. To this end, it is no more possible to use the results from friction tests as is but becomes mandatory to further analyse friction curves and extract the relevant parts serving the purpose. A new issue arises consequently: how to uniquely identify the relevant parts of the curves.

11.1 CONVENTIONAL IDENTIFICATION METHOD OF FRICTION CURVES

It does not really exist a unique way to analyse the friction curves in order to identify the moment of failure and either to choose which data are actually to include to calculate the CoF of each phase. There is the risk that each analysis comes down to how the operator interprets the result following his personal feeling or understanding.

Such an approach would be however wrong and prone to inconsistency: the subjectivity of the analysis must be kept as small as possible. A conventional identification method based on a graphical technique is thereby put forward and evaluated in this paper. It is summarised in bullet points in the following.

1) *Filtering of the curves*

Figure 10.14 to Figure 10.27 show that rough curves do not provide a clear representation of the CoF trend during the test. It is not possible indeed to pinpoint the starting and the ending point of each phase from such a measurement output. Therefore, curves were filtered using a moving average technique in order to obtain a thinner curve and a straightforward picture of the behaviour. Being the rotation speed about 3.8rps and the sampling frequency 80Hz, 21 points of measure are stored each turn of the mandrel. In order to maintain the representativeness of the phenomenon a 21 points filter was adopted. **Errore. L'origine riferimento non è stata trovata.** Figure 11.2 is an example of how a friction curve looks like after applying the filter and Figure 11.3 is the overall view of the 14 filtered curves belonging to the set of repetitions.

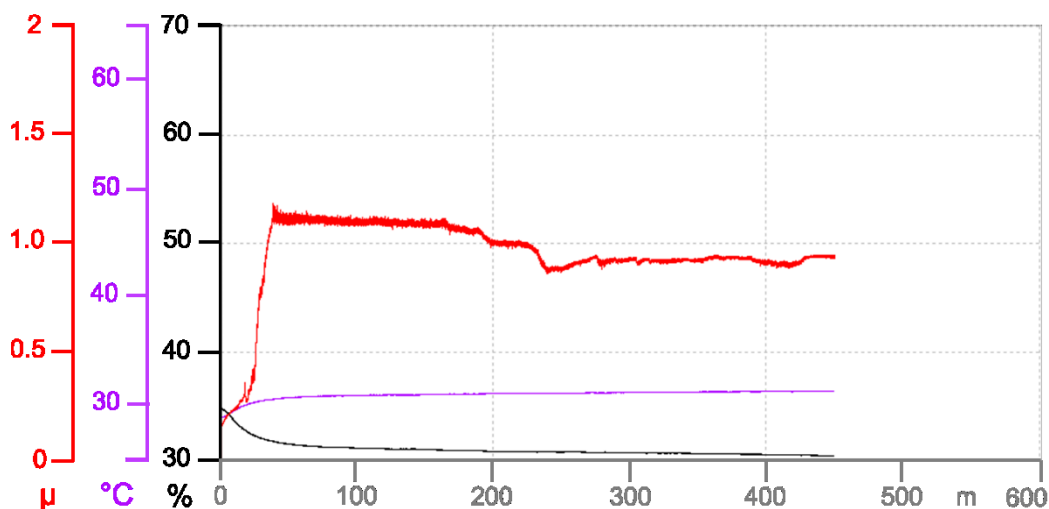


Figure 11.2 Test 1: filtered friction curve

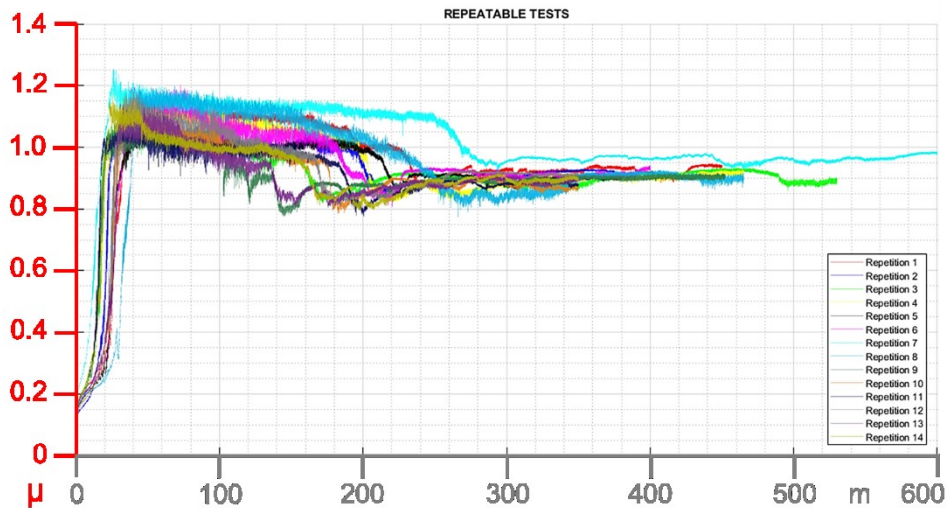


Figure 11.3 Overall view and comparison of the 14 filtered curves

2) *Conventional ending point of wear-in phase*

The wear-in phase comes to an end when the trend stabilises the first time. This transition is rather sharp and clearly identifiable for most of the curves but sometimes shows a gradual adjustment. For the sake of consistency, the point can be obtained as intersection of two significant lines describing the local geometry of the curve. The first line is a horizontal line corresponding to the maximum value of the CoF. If the information on the maximum value is not automatically provided by the data acquisition software (as is the case with Anton Paar InstrumX software) the value is easily obtained by exporting the curve and using the analysis tools of any worksheet. The second line is an interpolation line describing the slope of the last portion of the ramp disclosing a linear trend. The geometrical construction may be done either in an approximate way, drawing “by hand” the lines on the diagram or by resorting to a worksheet for higher precision.

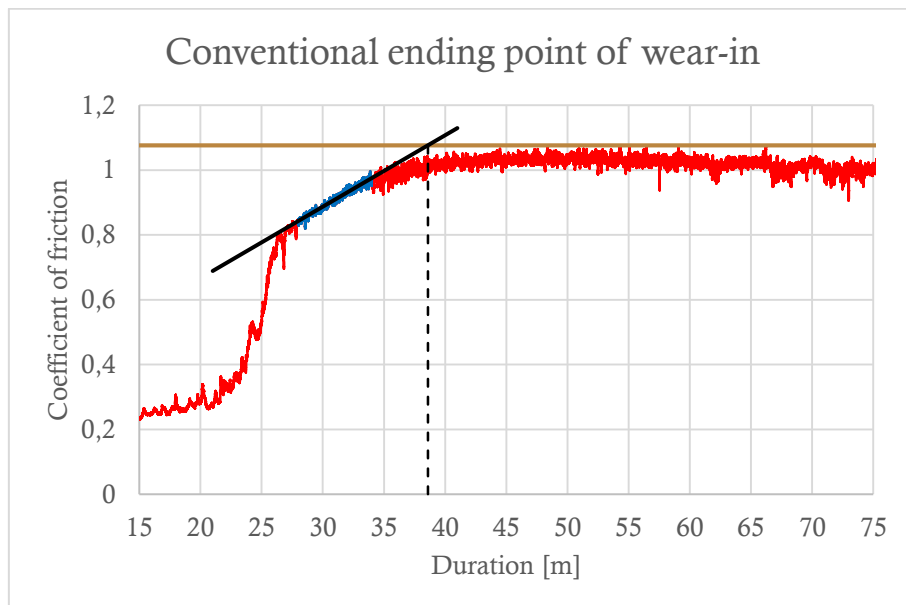


Figure 11.4. Conventional ending point of wear-in

3) *Conventional ending point of the on-coating run*

First, the curve has to be trimmed so that the wear-in phase is deleted. The ending point of the on-coating run can be obtained again as intersection of two significant lines and one of the lines is again the maximum of the CoF. To draw the second line, it is necessary to identify the point

of relative minimum of the trimmed curve; it is usually around the middle of the transition phase. The second line is now defined as the interpolation line in a region where the friction curve clearly discloses a linear decreasing trend, on the left of the minimum point. If more than one linear portion appear during the transition, the closest one to the minimum must be taken. The point thus identified must be now validated as *nominal coating lifetime*. If the corresponding value of the coefficient of friction is higher than the median between the maximum and the minimum CoF, the point is valid. Otherwise, a second attempt is made by changing the position of the second line, matching another linear portion of the curve more to the left. However, the point should be accepted all the same only if:

- the beginning of transition phase is clear;
- no other linear portions more to the left are available.

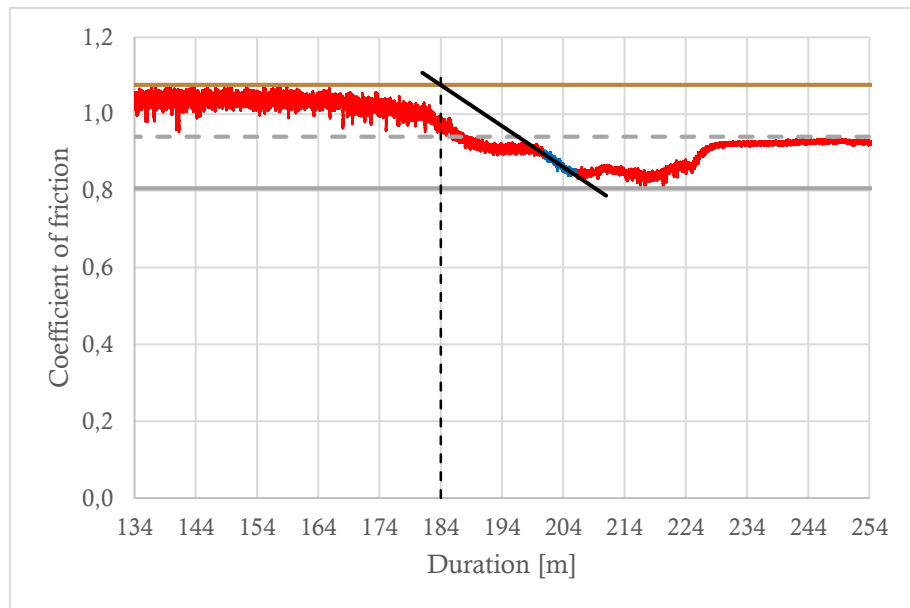


Figure 11.5. Conventional ending point of the on-coating run

4) *Conventional ending point of the transition phase*

The transition phase is v-shaped: after the point of local minimum the CoF grows and stabilises again. The average CoF over the fourth quarter of the curve is calculated and a horizontal line is placed on the curve at the same friction level. The ending of the transition phase may be arbitrarily placed at the first point on the left in which the curves moves away from this horizontal line near the zone of the v-shaped coating to substrate transition.

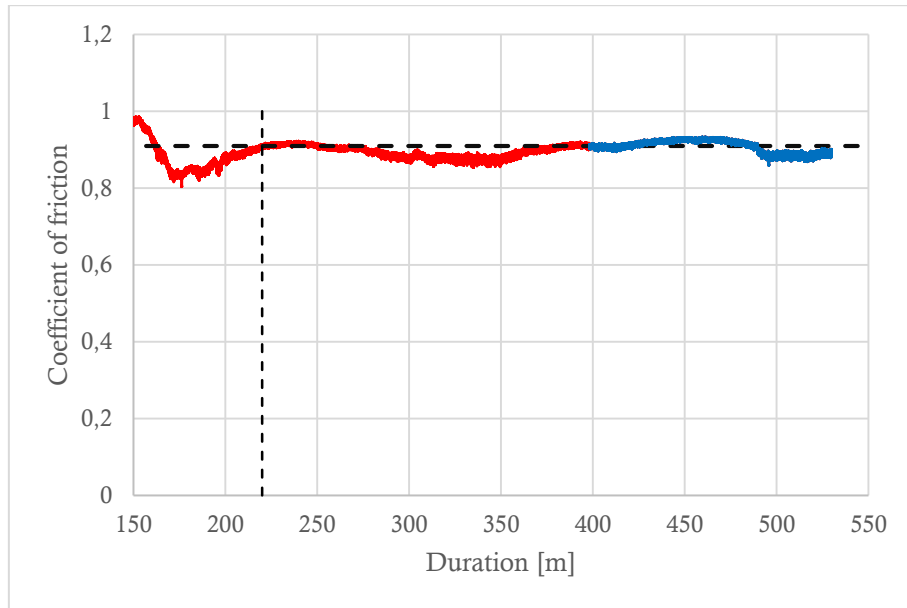


Figure 11.6. Conventional ending point of the transition phase

5) *Extraction of characteristic sectors*

At the completion of the identification process, it is possible to trim the curves and collect the homologous sectors to compute the on-coating and on-substrate statistics. The moving average filter should be released as it affects the scattering of the points of measure, impairing the standard deviation value.

Figure 11.7 and Figure 11.8 display the overall view of the on-coating sectors and on-substrate sectors cut out of the rough friction curve.

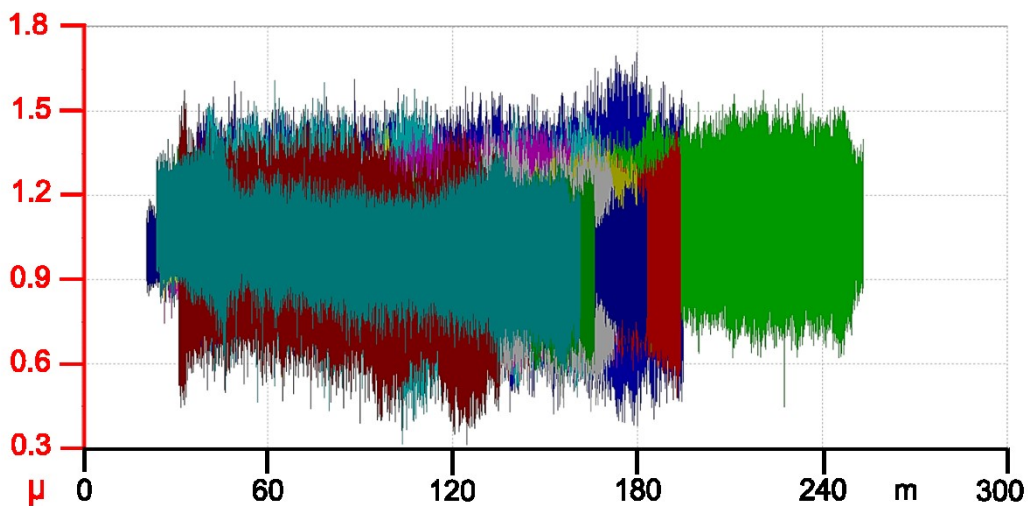


Figure 11.7. Overall view of the on-coating sectors

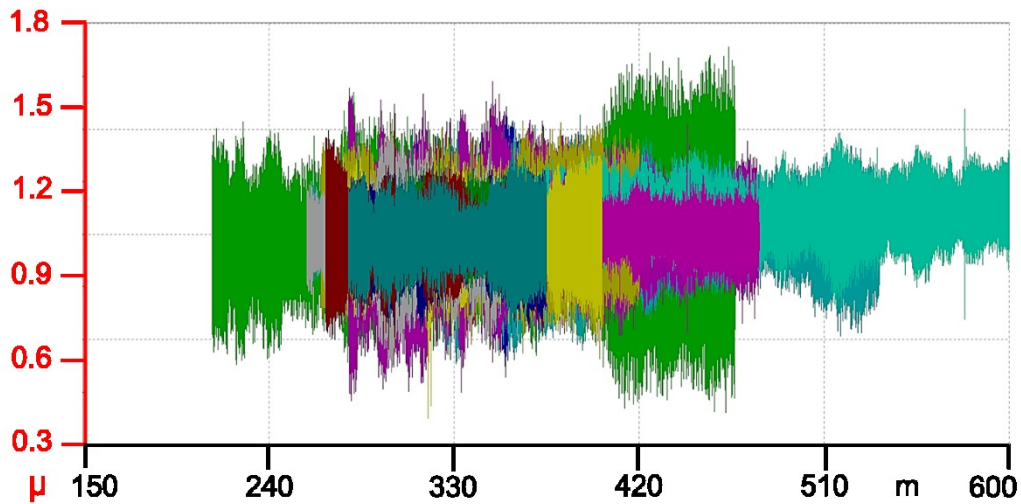


Figure 11.8. Overall view of the on-substrate sectors

11.2 SOME REMARKS TO THE METHOD

The procedure proposed in the previous section sets within the framework of a general method which is potentially suitable for any kind of thin hard coating. The authors should like to make some remarks about that yet.

- 1) It is always necessary that a stable testing condition is identified in advance.

The parameters used to run the test were identified after a rather long preliminary investigation that was vital to understand the tribological response of the chosen coating. The parameters recognised as optimal in this study are then convenient for TiN but they may be unsuited for other materials. Every time a new coating is to be characterised using a standard procedure of this kind, a preparative study should be performed to optimise testing parameters and set-up. The resulting friction curves should be, in fact, such that a flat, stable and clearly identifiable plateau appears before and after the coating failure. In addition, repeatability is a prerequisite. No attempt to characterise the system is worth otherwise.

- 2) The same procedure can also apply to the case of a system whose CoF is lower before the coating failure and higher afterwards.

In the previous section the procedure was explained in a special case, i.e. a system whose CoF is higher before the coating failure and lower afterwards. The same procedure can be equally valid in the opposite case, shown in Figure 11.9. Nevertheless, the reference horizontal lines needed to pinpoint the conventional end of wear-in and the conventional lifetime are no more valid. The local maximum of CoF should be taken instead of the global maximum for the end of the wear-in phase, as depicted in Figure 11.9. Similarly, the local minimum instead of the global maximum should be considered for the conventional lifetime estimation.

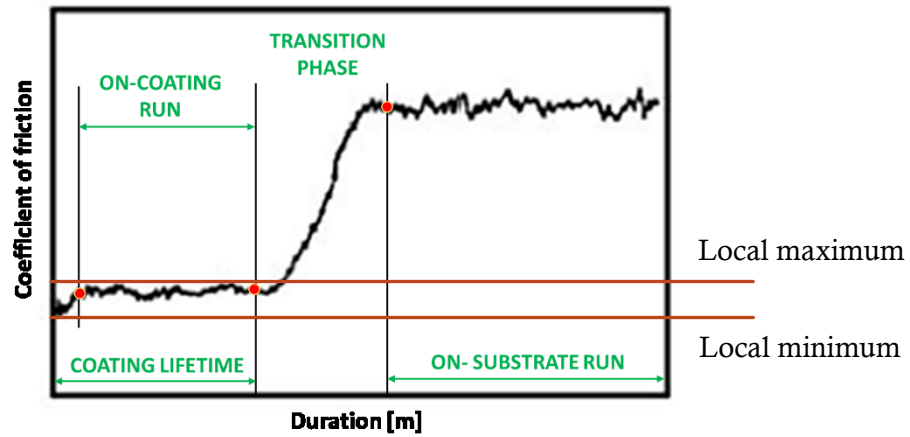


Figure 11.9. Simplified friction curve of a test during which CoF grows after the coating failure

11.3 ANALYSIS OF THE TRIBOLOGICAL RESULTS

11.3.1 Friction results

Table 11.1 is the numerical outcome of the method described in the previous section. It lists the average CoF for each identified on-coating and on-substrate sector and the average values of coating thickness and hardness of the corresponding sample. A very good repeatability is obtained for friction results. The variability in terms of standard deviation among the test average values is under 5% for the on-coating CoF and under and 3% for the on-substrate CoF.

Table 11.1

	Wear-in [m]	Nominal lifetime [m]	Average on-coating CoF	Average on-substrate CoF	Threshold CoF
Test 1	40.0	176.0	1.098	0.924	1,023
Test 2	23.5	140.5	1.009	0.900	0,956
Test 3	36.0	197.0	1.075	0.896	1,001
Test 4	38.0	201.5	1.008	0.900	0,961
Test 5	39.5	176.5	1.077	0.914	1,004
Test 6	28.5	239.0	1.130	0.963	1,082
Test 7	44.5	180.5	1.121	0.906	0,989
Test 8	21.5	100.0	1.033	0.892	0,941
Test 9	33.0	195.0	1.013	0.907	0,970
Test 10	35.5	172.0	1.016	0.881	0,974
Test 11	20.5	175.0	0.992	0.884	0,952
Test 12	37.0	174.0	1.046	0.915	1,017
Test 13	30.0	157.3	1.007	0.887	0,989
Test 14	23.5	147.0	1.015	0.893	0,984
Mean value	-	169.1	1.046	0.905	-
Standard deviation	-	35.2	0.044	0.021	-
Standard deviation [%]	-	20.8	4.24	2.28	-

In the following, the quantities measured during each test are plotted against coatings properties in order to highlight potential correlations.

Figure 11.10 shows the diagram of the nominal lifetime obtained with the standard method proposed in sec. 11.1 versus the coating thickness.

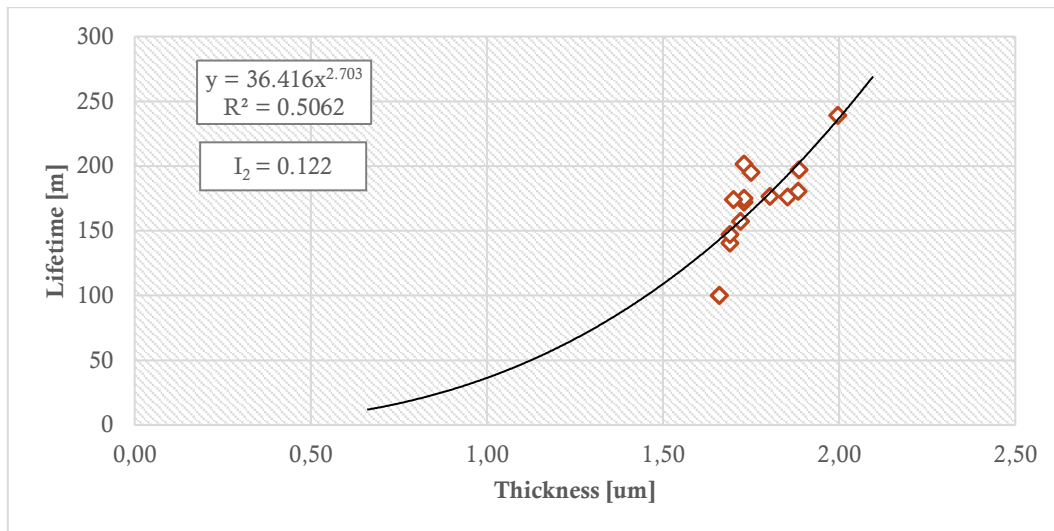


Figure 11.10. Nominal lifetime versus coating thickness

As stated in sec.8.4 the influence of thickness is not at all straightforward and there are plenty of parameters whose importance may prevail as the amount of hard wear-resistant material grows. PVD TiN coatings have typically a porous structure due to a columnar growth on the substrate surface during deposition. Thicker layers are then more prone to crack along the columnar formations, making it easier for the coating to meet flaking or delamination as soon as a shear stress is applied.

It is thus unlikely to expect that lifetime proportionally increases with increasing the coating thickness since it is not merely a question of material which has to be remove before the ball reaches the substrate. However, a possible correlation should take into account that the lifetime will reduce to zero if thickness is zero (no hard layers cover the substrate), i.e. the fitting curve should pass through the origin of the diagram.

In Figure 11.10 a *power law* is attempted to perform a statistical interpolation of the identified coating lifetime values. The coefficient of correlation R , that is calculated with the *Ordinary Least Square* method, is equal to 0.659. It tells, theoretically, how strong the interpolation of experimental values is [52]. Being it higher than 0.5, it seems that a positive correlation exists. However, coefficient R is a subtle parameter which should not be trusted completely. It is no more referred to in the following analysis.

In order to evaluate the goodness of the correlation proposed, the *index of quadratic deviation* I_2 can be resorted to. This index takes into account how much experimental points deviate from the corresponding ones predicted by the interpolation curve. It is believed a more representative parameter indeed for the purpose of this analysis. Figure 11.10 shows that the power-law interpolation seems to acceptably describe the scattering of experimental point, but some uncertainty still remains. The index I_2 indeed takes a rather high value equal of 0.132, whereas a good agreement between experimental data and trend line would conventionally require $I_2 < 0.1$ [53]. More robust assessment would require many more test on samples with more different coating thicknesses.

A completely different portrayal appears if the average values of CoF are plotted against the coating thickness. The relating diagram are show in Figure 11.11. A linear interpolation seems ideal to describe the influence of thickness for both the on-coating and on-substrate CoF, at least when small changes between 1.5 and 2 μm occur.

The linear correlation between on-coating CoF and thickness is manifest in Figure 11.11a. It is not obvious why this linear correlation should be there, yet other researchers observed a similar behaviour. For example, Shimazaki and Winer (1987) observed that the friction increases with the absolute value of film thickness when a steel ball is used as counterpart [4]. Other experimental evidences indicate that CoF is a function of film thickness and it has a minimum value typically at film thicknesses of about 1

μm [4]. Of course, the film thickness variability was purposely kept as low as possible in this study, therefore it is not possible to make an assessment with general validity. Many more tests with a larger thickness variability are needed to further validate this conclusion.

In the ending part of the test it is expected to have a nearly constant CoF mostly independent of the layer itself. Figure 11.11b shows indeed that experimental values suffer a minor increase with increasing thickness, evidence that the thickness of the ceramic layer pales into little significance after the coating wear-through. During the on-substrate run however, the sphere interacts with both the substrate (in the middle of the wear scar) and the ceramic layer. The influence of thickness may be limited to the different extension of the contact region where the ball still interacts with the ceramic material and this might explain the upward trend.

The index of quadratic deviation is very low in both the cases, meaning that the trend line describes very well the position of the experimental point on the diagram.

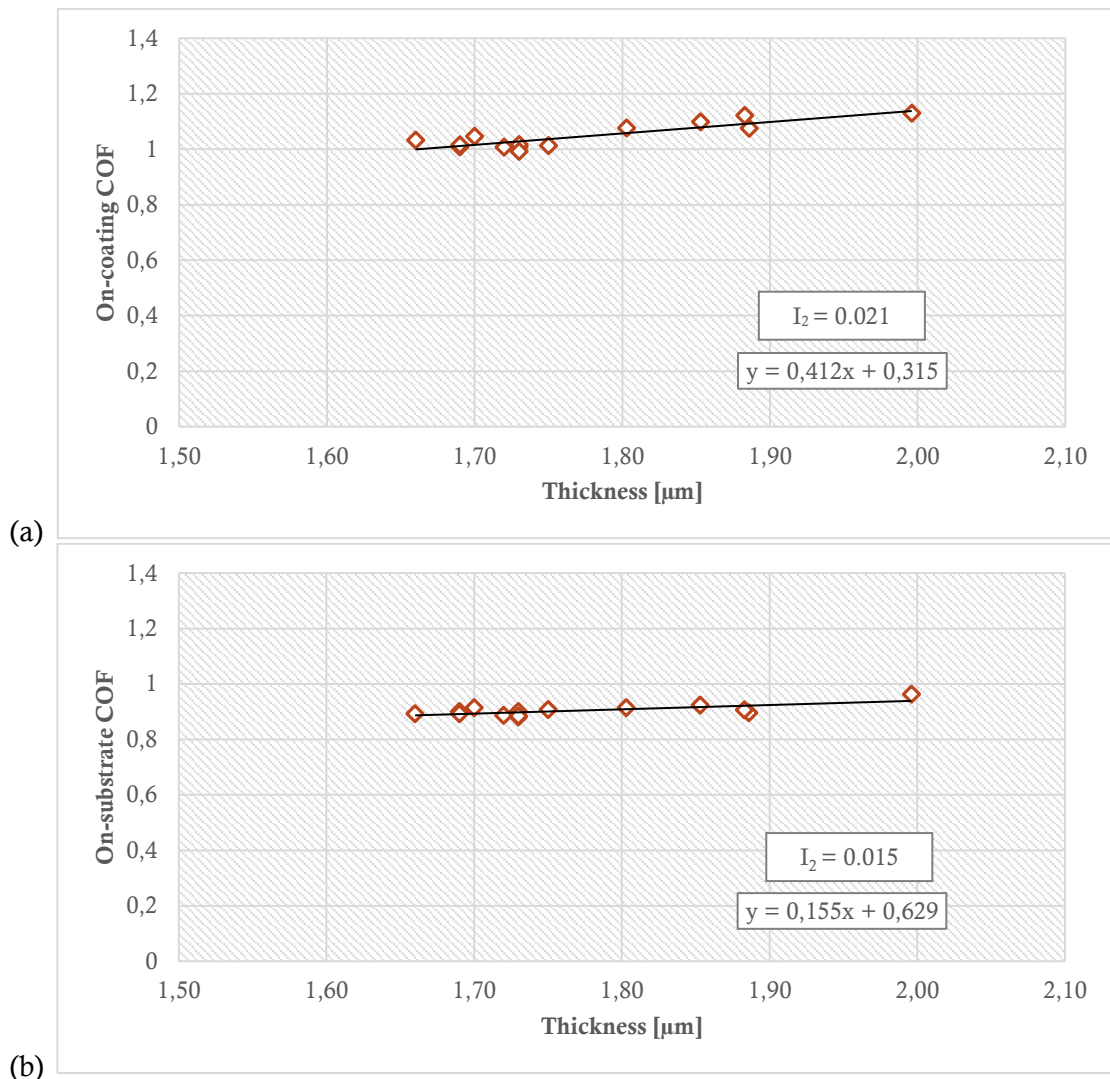


Figure 11.11. On-coating CoF versus coating thickness

Figure 11.12 displays the diagram where on-coating CoF is plotted against nominal lifetime. No correlation seems present: the experimental values are practically aligned at a same value, as the little slope of the trend line suggests. This result is evidence that the same friction and wear mechanisms act at the tribological interface as long as the contact persists on the coating. It is perfectly consistent with the fact that a flat and nearly horizontal friction curve appeared in in the first stable part of the tests.

One may come to a very similar conclusion by analysing Figure 11.13, from which on-coating CoF seems independent of the ceramic layer hardness too.

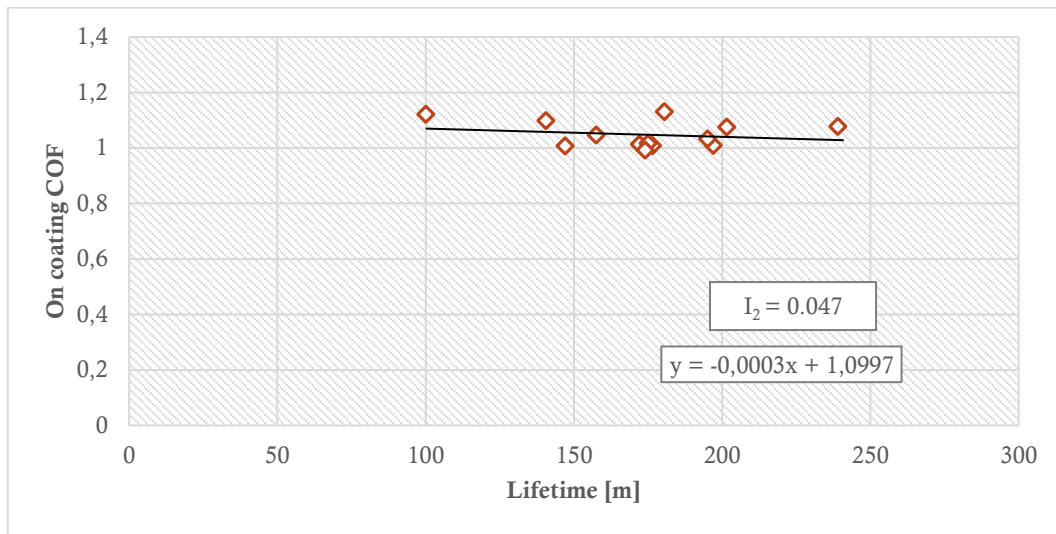


Figure 11.12. On-coating CoF versus coating lifetime

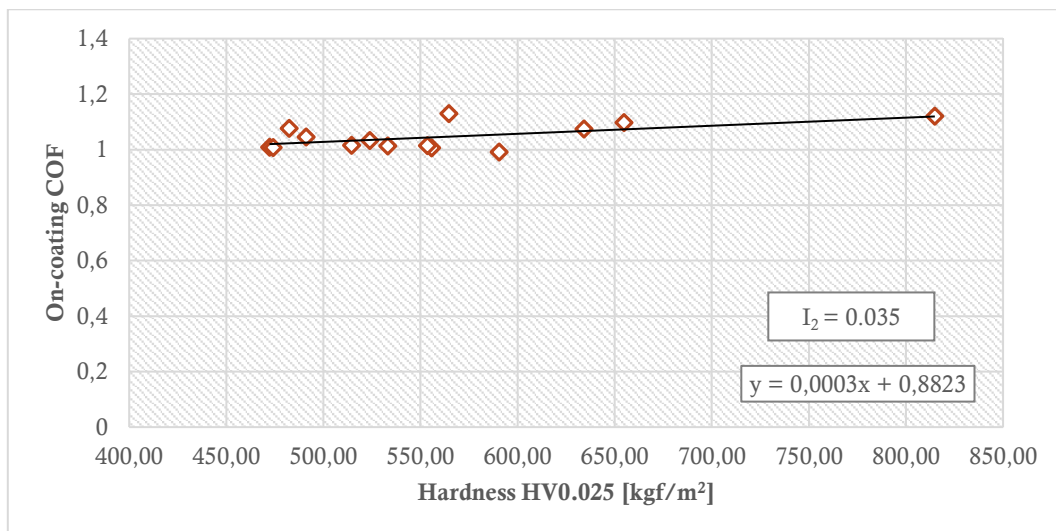


Figure 11.13. On-coating CoF versus coating hardness

11.3.2 Wear

Table 11.2 presents the outcome of the in terms of wear. The 14 repetitions are compared in terms of two quantities: the *wear volume* and the *specific wear rate*. Both these quantities are calculated according to the ISO 18535:2016 standard.

$$V_d = \frac{\pi R \cdot (S_1 + S_2 + S_3 + S_4)}{2} \quad (43)$$

Where: R is the track radius [m];
 S is the area of a single cross-section of the wear track [m²];
 V_d is the wear volume, i.e. the volume of material removed from the disc [m³].

$$W_s = \frac{V_d}{F_N \cdot s} \quad (44)$$

Where: W_s is the specific wear rate [m²/N];
 F_N is the normal load [N];
 s is the total duration of the test [m].

The wear volume is used to compare the last 6 tests only which ran the same test length equal to 350m and were therefore directly comparable. The specific wear rate is used to compare the results all together, since each wear volume relates back to the total tests duration (in meters).

Table 11.2

	Nominal lifetime [m]	$S_{average}$ [m ²]	V_d [m ³]	W_s [m ² /N]
Test 1	165	401.3	1.06E-11	2.35E-23
Test 2	118	482.0	1.27E-11	2.40E-23
Test 3	195	545.5	1.44E-11	3.09E-23
Test 4	192	335.8	8.86E-12	2.36E-23
Test 5	178	403.8	1.07E-11	2.66E-23
Test 6	250	565.3	1.49E-11	2.49E-23
Test 7	158	496.0	1.31E-11	2.81E-23
Test 8	100	344.8	9.09E-12	2.02E-23
Test 9	192	305.5	8.06E-12	2.30E-23
Test 10	174	305.8	8.07E-12	2.30E-23
Test 11	183	240.0	6.33E-12	1.81E-23
Test 12	166	303.3	8.00E-12	2.29E-23
Test 13	135	368.3	9.71E-12	2.78E-23
Test 14	162	336.0	8.86E-12	2.53E-23
Mean value	169.1	309.8	8.17E-12	2.44E-23
Standard deviation	35.2	38.9	1.02E-12	3.15E-24
Standard deviation [%]	20.8	12.5	12.5	12.9

The mean and standard deviation value of the wear scar volume was then calculated from the last 6 tests. ASTM G99 states that properly conducted tests should maintain a within-laboratory coefficient of variation equal to 20% or less for wear loss values. In this study, standard deviation settles at just 12,5%, being perfectly consistent with ASTM G99 guidelines.

Figure 11.14 to Figure 11.16 presents the results of the last six tests which ran for the same duration. In these diagrams actual wear volume is plotted against nominal lifetime and coating thickness and coating hardness, respectively. A decreasing trend appears in all the cases and. The correlation between lifetime and thickness is hard to define but undeniable, it is thus perfectly consistent that a similar behaviour arises. The index of quadratic deviation is rather high. In all the diagrams it exceeds the threshold of 0.1 above which the interpolation is considered not perfectly satisfying. Figure 11.16 presents the strangest result: no relationships seems to be there for hardness lower than 550 HV0.025; whereas above this value the experimental points scatters erratically. The typical large variability of hardness measurements may play here a fundamental role and thus the trend line has little meaning.

However, in Figure 11.14 and Figure 11.15 there is a point which deviates farther from the trend line, it is marked in green in the figures. It should be mentioned that this point represents always the 11th test and therefore it can be considered as an outlier. If this experimental point was ignored, the index I_2 would reduce drastically becoming the trend line much more representative.

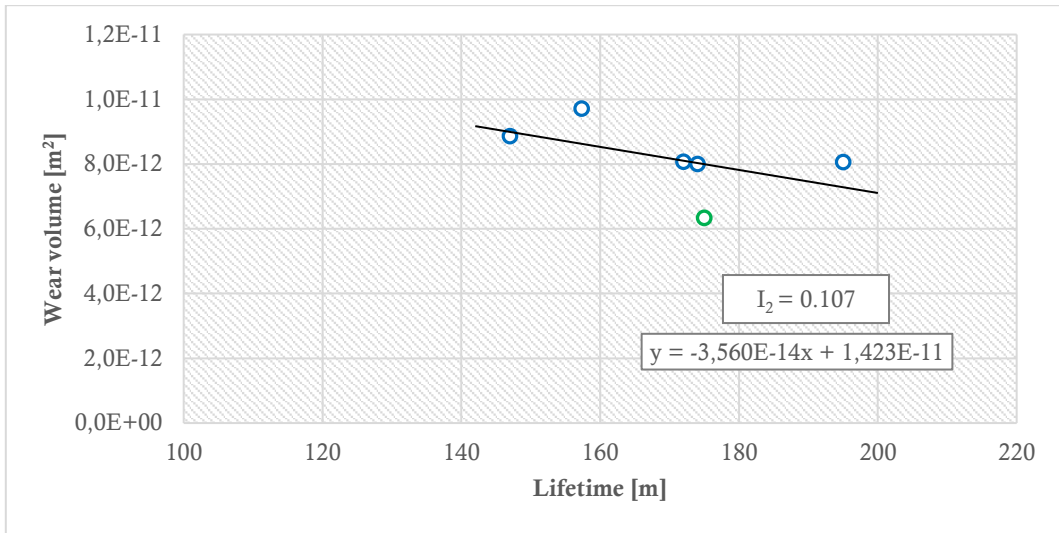


Figure 11.14. Wear volume versus coating lifetime (test under equal duration only)

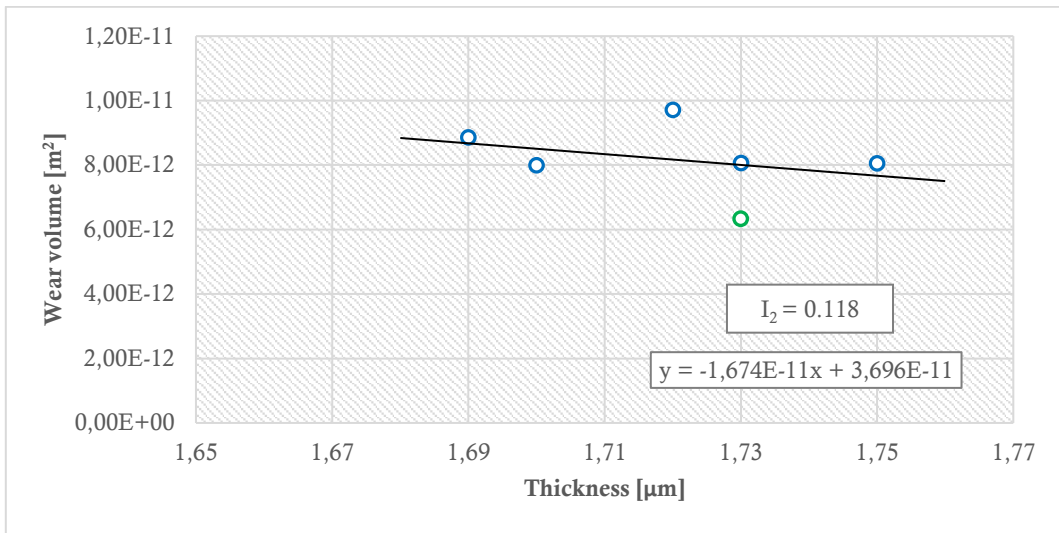


Figure 11.15. Wear volume versus coating thickness (test under equal duration only)

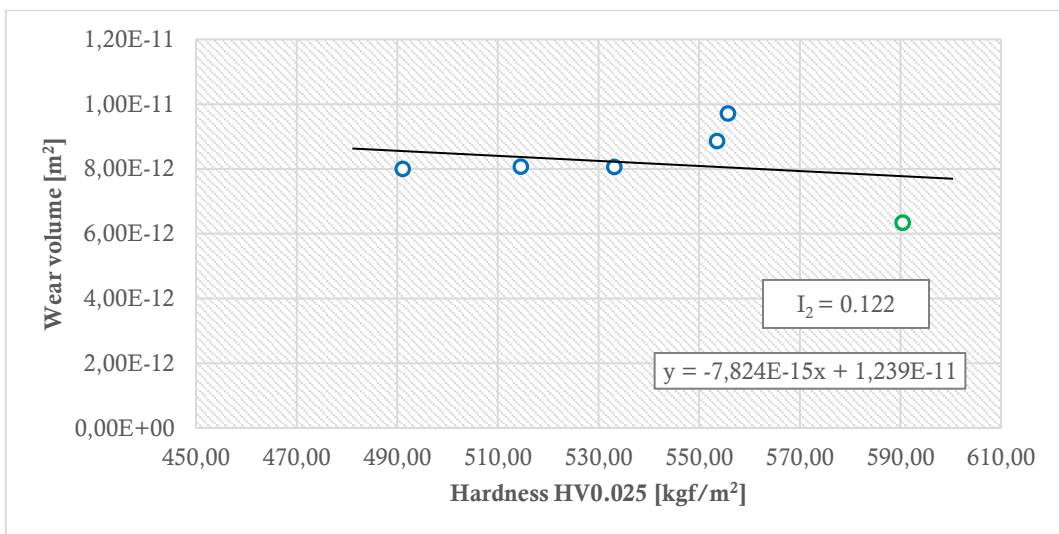


Figure 11.16. Wear volume versus coating hardness (test under equal duration only)

Since all the tests ran until the ball had penetrated the coating, in this study wear volume is a mixed quantity accounting for the removal of both the hard layer and the substrate. It is not possible indeed to calculate separately the removed volume before and after coating failure, unless the test is stopped and

resumed several times. The decrease in the value of wear volume is symptom that a thicker layer is however beneficial as it delays coating penetration.

As to the specific wear rate, Figure 11.17 to Figure 11.19 show that very weak correlations appear in the diagrams as the experimental points are very scattered. In these figures, the trends of the specific wear rate value against the three fundamental coating parameters are considered, i.e. nominal lifetime, thickness and hardness. A trend line is used to describe data, but many more tests are necessary to understand whether a linear correlation exists. The index of quadratic deviation is always much higher than 0.1, meaning that the representation is not satisfying.

Furthermore, the calculated interpolation line discloses a positive trend, meaning that the increase in coating thickness, hardness or lifetime would produce larger wear. Recalling the remarks presented in Sec. 8.4, it cannot be said, a priori, that such result is illogical. A hard layer has indeed a complex influence on the behaviour of the whole tribological system. It seems however that a contradiction is presented between these results and those of wear volume, shown in Figure 11.14 and Figure 11.15.

The conclusion of this author is that a specific wear rate of this kind, though widely used in tribology, may be not suited for coated systems. Pondering actual wear volume with load and sliding distance alone probably fails in providing a representative picture of the wear behaviour in presence of a coating-to-substrate transition.

In the view of the author, other coating properties like thickness, hardness and adhesion strength should be introduced to compare tests carried out under different testing conditions or, simply, on different samples. However, this goes beyond the scope of this dissertation.

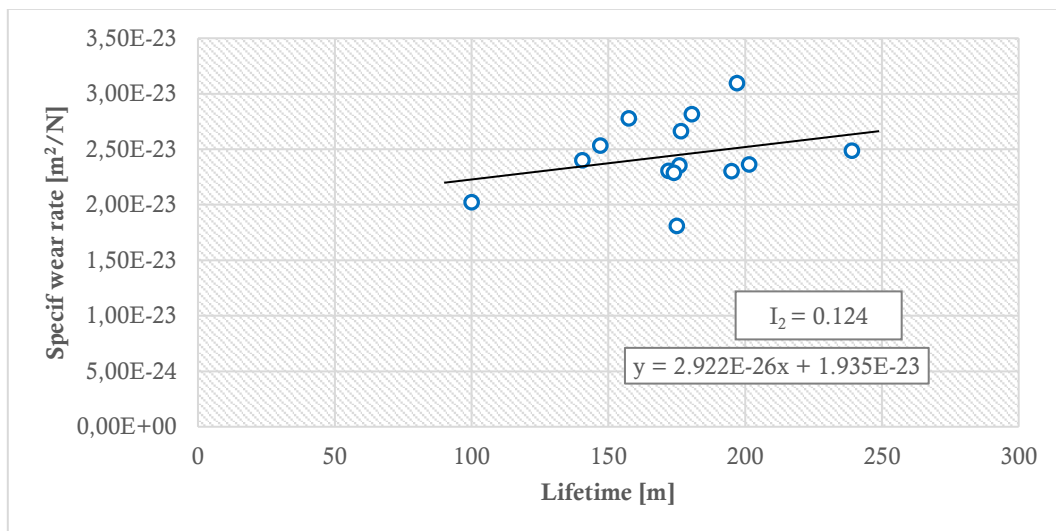


Figure 11.17. Specific wear rate versus nominal lifetime

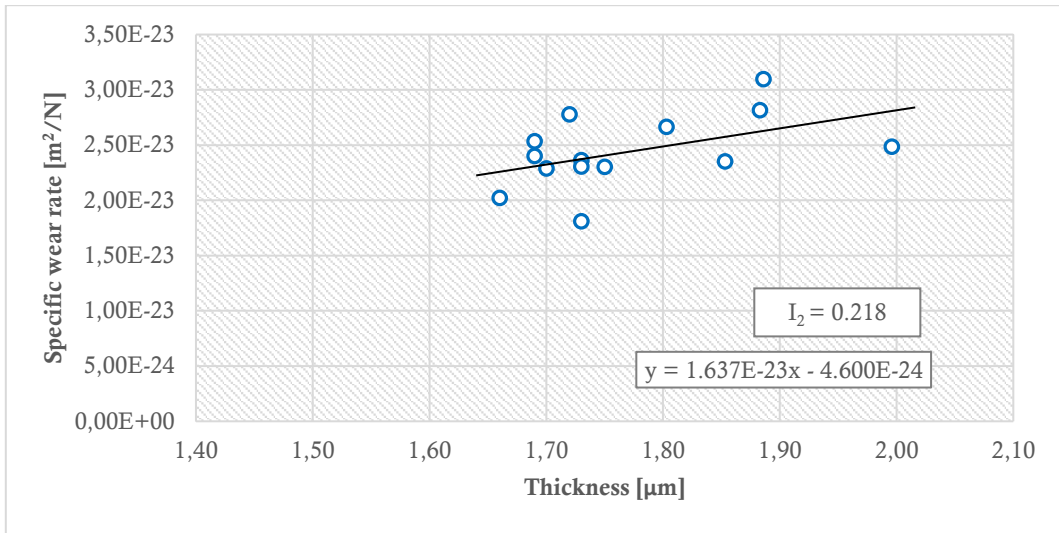


Figure 11.18. Specific wear rate versus coating thickness

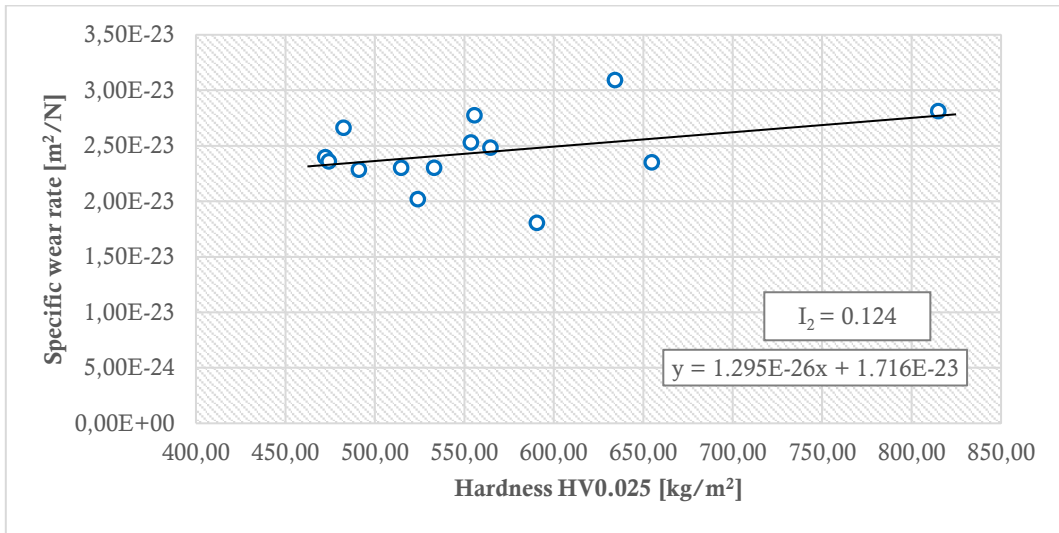


Figure 11.19. Specific wear rate versus coating hardness.

12 CONCLUSION

In the first part of this dissertation two industrial reference testing procedure for friction measurement were developed on three different Anton Paar tribometers. To this aim the friction properties of the EHL were exploited. Such procedures are intended to be used in industrial laboratories where testing machines requires regular examinations to assess their proper functioning. The result is a testing set-up easy to prepare and carry out, cheap and potentially fit for the application on any tribometer whatsoever.

Care was taken to improve some key features for industrial applications. A special lubricated point contact was produced with several pin-on-disc tribometers in conditions which were quite different from other research on lubricated contact mechanics in the scientific literature. No lubricant bath was used and only a little amount of lubricating oil was added and thrown away for each test, perfectly meeting the requirements for industrial applications.

Two types of oil were compared, a middle viscosity oil and a high viscosity oil. From the existing knowledge on this matter, it is known that the higher the pressure-viscosity coefficient of the lubricant, the better the supporting effect. The HVo may look, a priori, the best choice in terms of performance but the use of the still MVo has many advantages. Since perfect cleaning is of paramount importance, the degreasing procedure is particularly laborious even if small amounts of the HVo are used. Acetone and gasoline, which are normally aggressive enough to dissolve the MVo, usually fail and specific strong spray solvents must be used for the sake of saving time. Therefore, the MVo is still preferable for low load applications, for ease of applying and removing the lubricant, keeping the equipment clean and, consequently, lessening the environmental impact.

All the results presented and discussed in this paper have a sufficient degree of stability and repeatability This significant result was attained with no strict requirements in terms of speed, the most influencing parameter over the EHL regimes. Linear speed (i.e. the composite entrainment speed as well) was left free to change, providing that solid surfaces separation was at least ensured. And what is more, stability of results is obtained even though samples with imperfect repeatability were used.

The author concludes that such procedures do apply to the diagnostic verification of tribotester by letting users, at least, make a preliminary assessment on the proper functioning of the test rig. The author is also convinced that it may be an effective verification method for inter-laboratory cross studies, before which a common sample should be tested to make sure the instruments all give consistent results.

The author believes that further experimental verifications on many more pin-on-disc tribotesters of various manufacturers are necessary to consolidate this method and improve its reliability. From this perspective, there is great interest in launching a cross-instrument comparison study in the future using the same methodology presented in this paper.

Finally, the ultimate purpose is to propose this methodology becomes part of an international tribological standard, for example next releases of ASTM G99 and G133 standard. This will hopefully spread this message in the future for all tribologists to adopt this method worldwide.

As to the second part of this dissertation, a reference procedure for the tribological characterisation of coated systems was developed by means of an Anton Paar pin-on-disk tribometer.

No scientific standards exist at present dealing with tribological testing of hard coatings satisfactorily. ASTM G99 gives a too general method barely suited for bulk materials and, on the other hand, ISO 18535 is not concerned about what happens during the transition from coating to substrate and afterwards. Moreover, this latter standard was originally developed for DLC films. Despite it was extended to any kind of hard coatings, it may turn out inappropriate for softer ceramic layer.

As opposed to the ISO 18535:2016 approach, in this study the friction and wear behaviour was investigated during and after the coating wear-through. To this aim, a typical and widely used hard ceramic coating, a PVD TiN coating, was selected and an extensive investigation was implemented. A preliminary study on the tribological response of the given coating was performed in different testing conditions and with a number of materials as counterpart. One set of optimal parameters was eventually selected, and 14 repetitions of the same tests were carried out on 14 samples using a 10mm alumina ball.

The initial purpose was to achieve a characterisation procedure under conditions of moderate load and high speed, which are typical working conditions of coated components in industrial applications. This was however not possible as high speed intensify the dynamics of the test rig itself, resulting in unregular and unstable friction curves and inconsistent tribological behaviour. In the end, a low load and low speed condition was proven to be the best trade-off among representativeness of applications, ease of friction curves analysis and uniform coating failure during the test.

A graphical procedure for the analysis of friction curves was put forward. It is intended as a tool for the conventional identification of the curve sectors which are relevant for the experimental estimate of the CoF. Two values of the coefficient of friction for the system were dealt with: the *on-coating CoF* representing the behaviour before the coating failure and the *on-substrate CoF* after the coating wear-through. These values were collected from each test and analysed in order to find possible correlations with the coating properties. The amount of wear was also calculated resorting to stylus profilometry of wear tracks and accounted for through the specific wear rate (W_s) as ISO 18535 suggests. This parameter was found inadequate for coated systems anyhow, since it seems it does not take into account correctly the beneficial influence of coating thickness, hardness and other properties.

The procedure here proposed sets within the framework of a general method which is potentially suitable for any kind of thin hard coating, provided that a stable testing condition is identified in advance. The author wishes to recall here the remarks already made elsewhere about the testing parameters: the parameters used in this study were found convenient for TiN but may be unsuited for other coating materials.

This study opens up the way towards one viable systematic tribological characterisation of coated systems and the auto-determination coatings lifetime. Many more tests with many more types of coatings will be however necessary in the future to prove the reliability and generality of this method. Furthermore, the author recognises that the assessment procedure for friction curves is still too “subjective”, as a certain degree of freedom is left to the user interpretation and feeling, and this procedure still needs some improvements in the future. Some math algorithm should be developed to support the analyse of friction results and enhance scientific objectivity.

If the method will be shown to be effective, the ultimate purpose is to submit it to the ASTM G02 Committee to become part of next release of ASTM G99 as a general method for hard coatings.

APPENDIX

A.1 EHL – TEST IN HIGH HUMIDITY CONDITIONS

It is commonly known that humidity is a treacherous parameter in the field of friction tests as the moisture content does usually influence what happens at the interface. When speaking of “ambient state”, reference is usually made to a narrow and well-defined temperature range (about 15°C-25°C), whereas in fact very different and quickly changing moisture contents can be related to it.

Table 0.1. Results in wigh humidity conditions

Machine	Oil type	Number of samples	Total number of repetitions	Valid tests	MMV	St.DMV	MSt.DV	Laboratory
TRB ³	MVo (rotating)	1	21	20	0.0746	0.0007	0.0015	Anton Paar TriTec, Peseux (SW)
	MVo (linear)	1	25	25	0.0744	0.0004	0.0004	

In order to be sure that this procedure is not affected by humidity, some additional set of tests (see Table 0.1) have been carried out into an environment with 94-96 % humidity. No higher values of humidity were tested since it was imperative to avoid extensive condensation of water droplets on metallic surfaces.

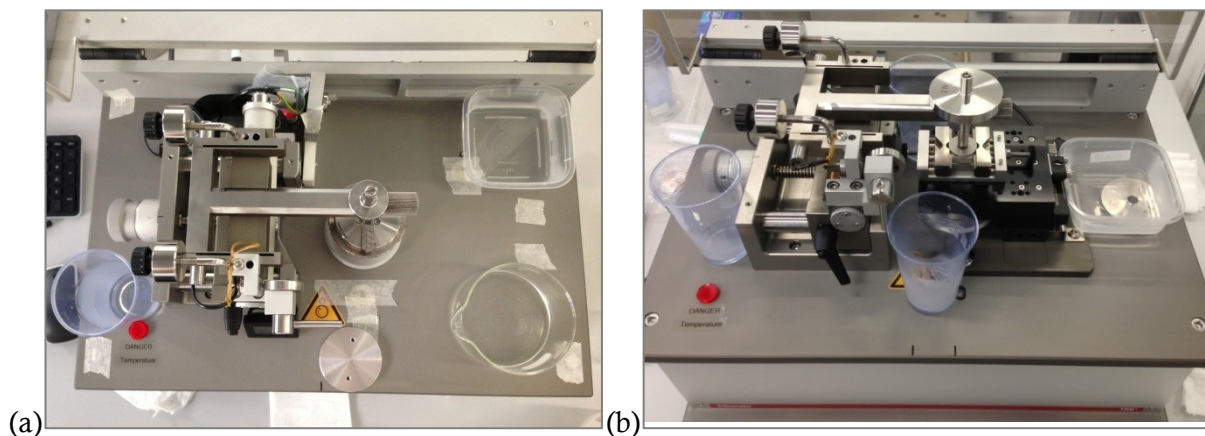


Figure 0.1. Test setup for the generation of a near-saturate moisture content into the measuring chamber (a) rotating tests; (b) linear reciprocating tests

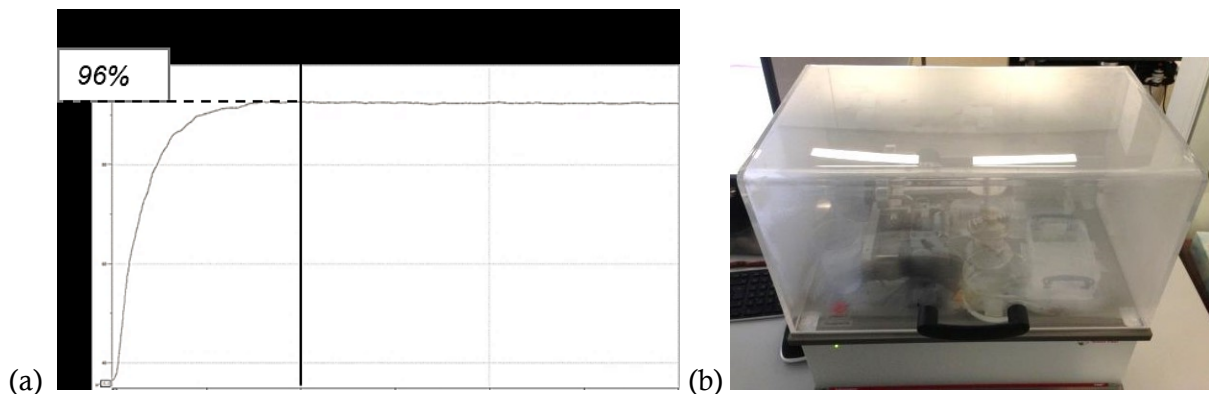


Figure 0.2. (a) Evolution of the moisture content into the test chamber, the black line represents the start condition of the test; (b) moisture content during a test run

The desired moisture content was achieved by introducing into the chamber of measure some flasks and jars filled with a little amount of boiling water (see Figure 0.1). The humidity sensor allowed to monitor the raising trend of humidity, waiting for each test to be started once the moisture content has stabilized (after about 5 minutes).

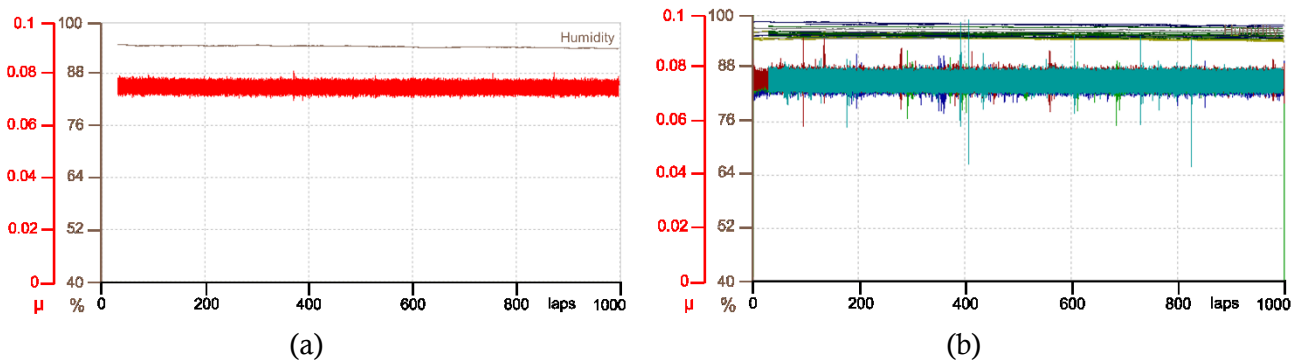


Figure 0.3. TRB³, MVo, 2N load, 100rpm, rotating test. (a) example of friction curve; (b) overview of all the tests in a high humidity environment

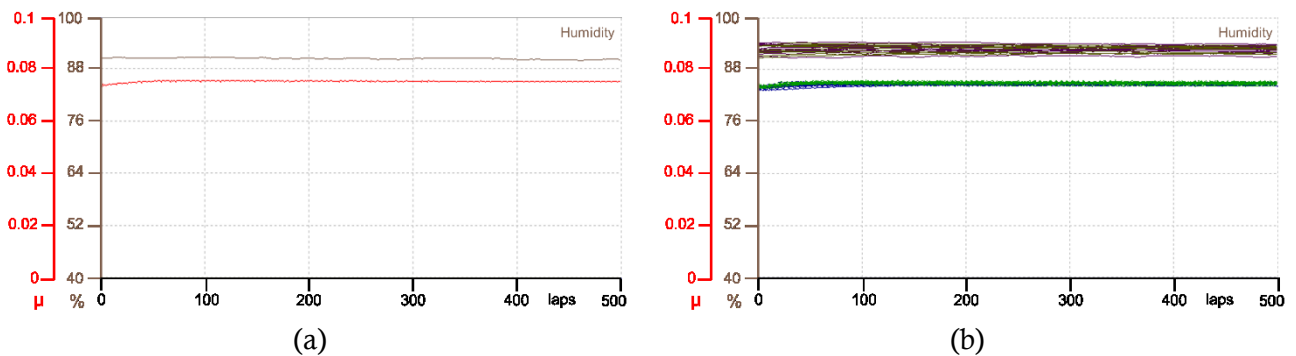


Figure 0.4. TRB³, MVo, 2N load, 100rpm, linear reciprocating. (a) example of friction curve; (b) overview of all the results in a high humidity environment

These additional results are perfectly consistent with the results in normal condition, evidence that (as expected) a small quantity of oil is enough to isolate the contact zone from the environment. The conclusion is that this procedure is valid regardless of the ambient humidity.

As visible in Figure 14, the very beginning part of some repetitions (both linear and rotating ones) were cut because after a wait of 5 minutes (to reach the desired moisture content) the oil was spread irregularly over the glass surface. A few laps were necessary in general to restore a uniform oil distribution of oil and the resultant transition zone for the coefficient of friction had to be deleted for reason of consistency with other tests at ambient conditions.

A.1 TiN – TABLE OF FILTER CURVES

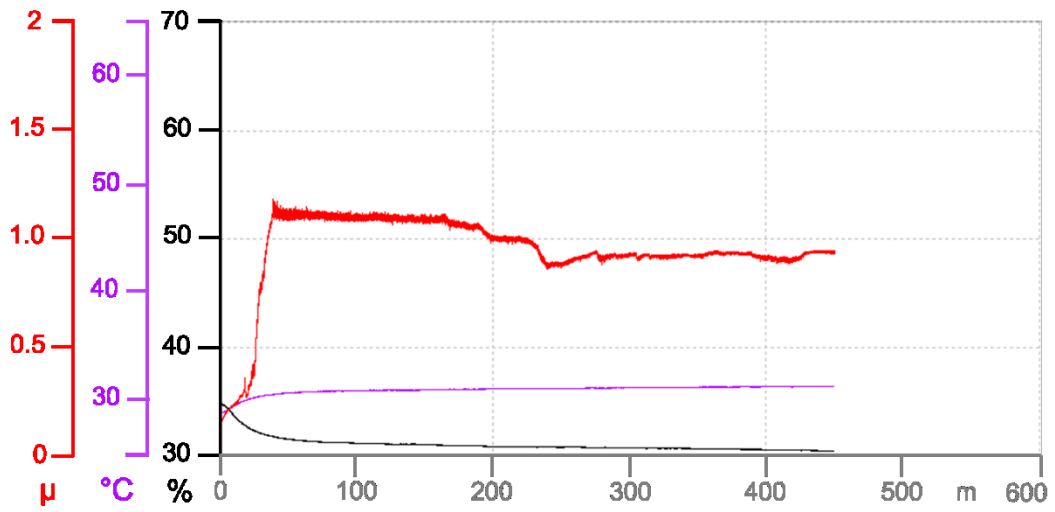
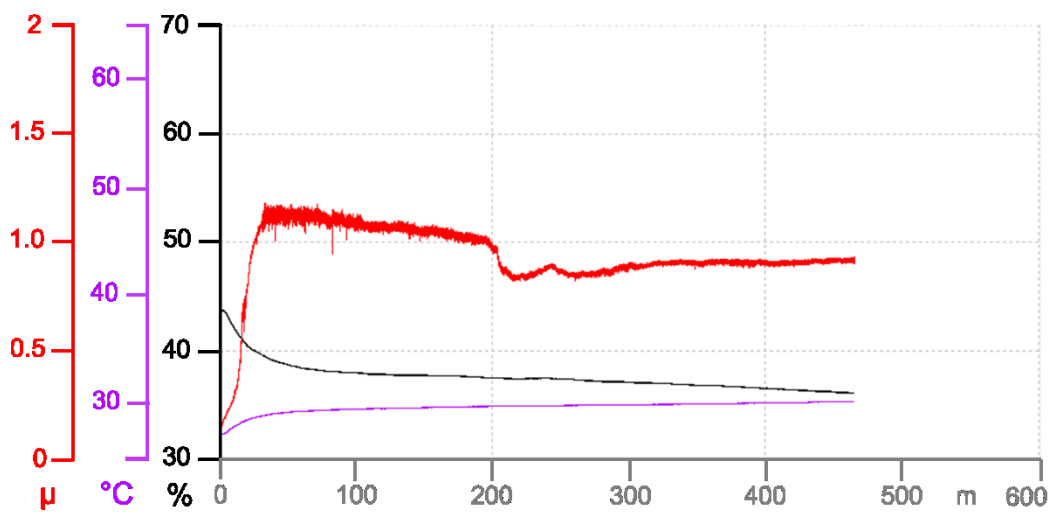
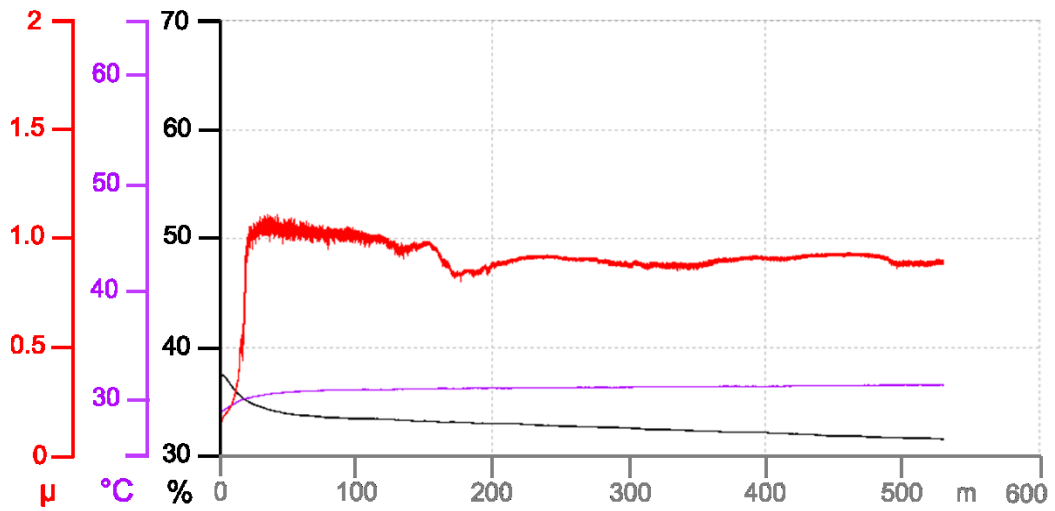
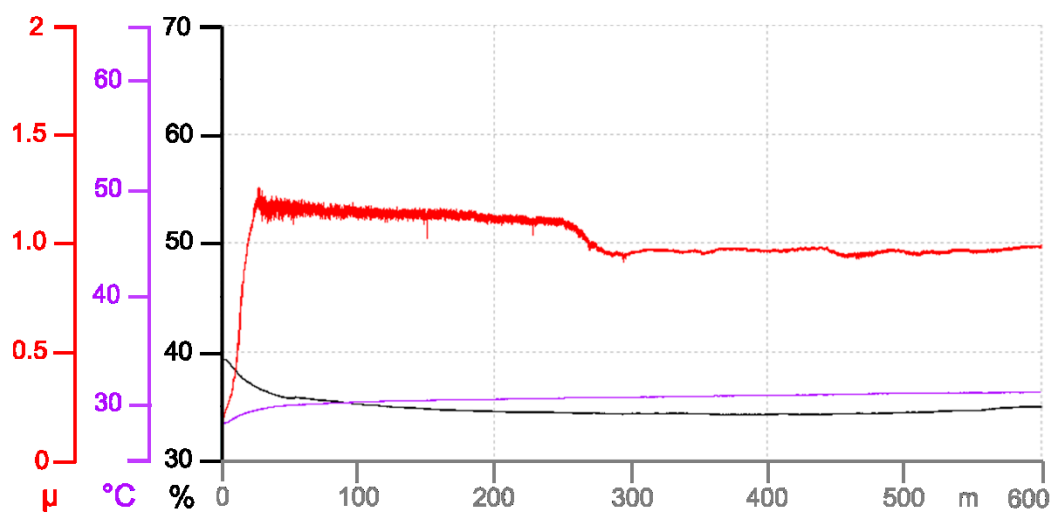
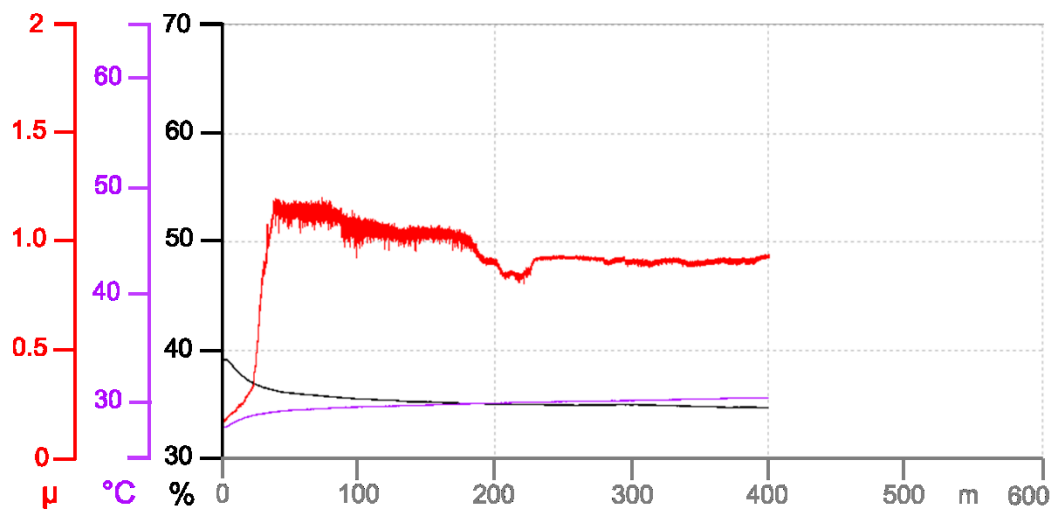
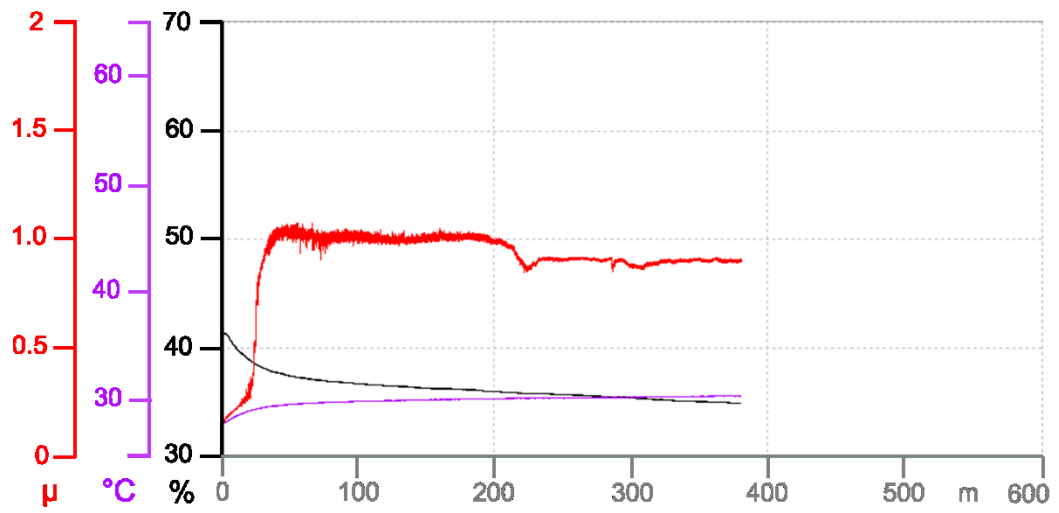
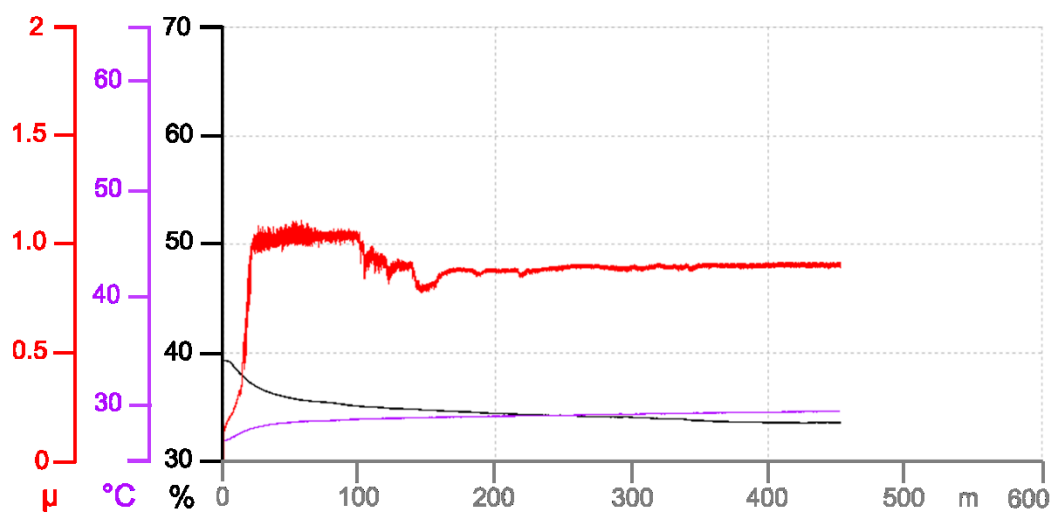
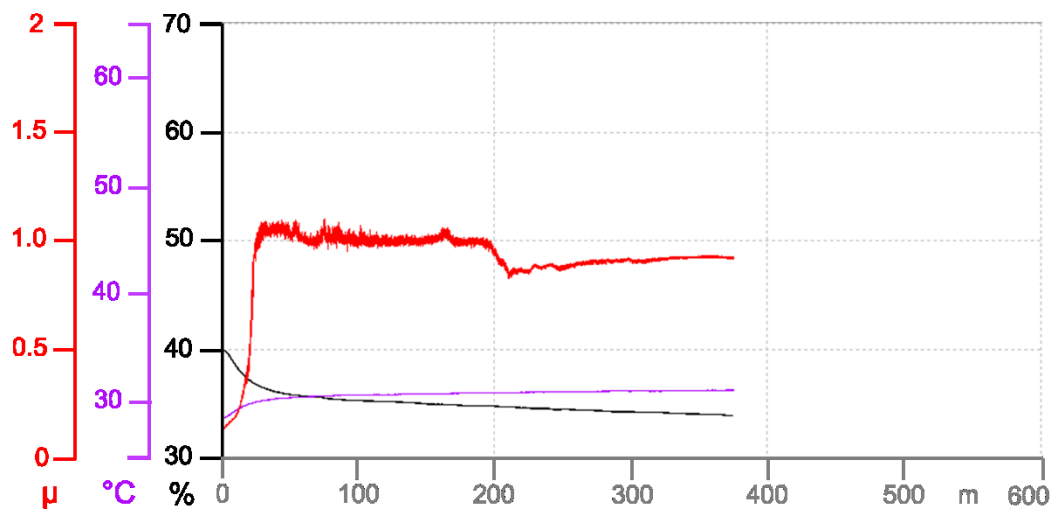
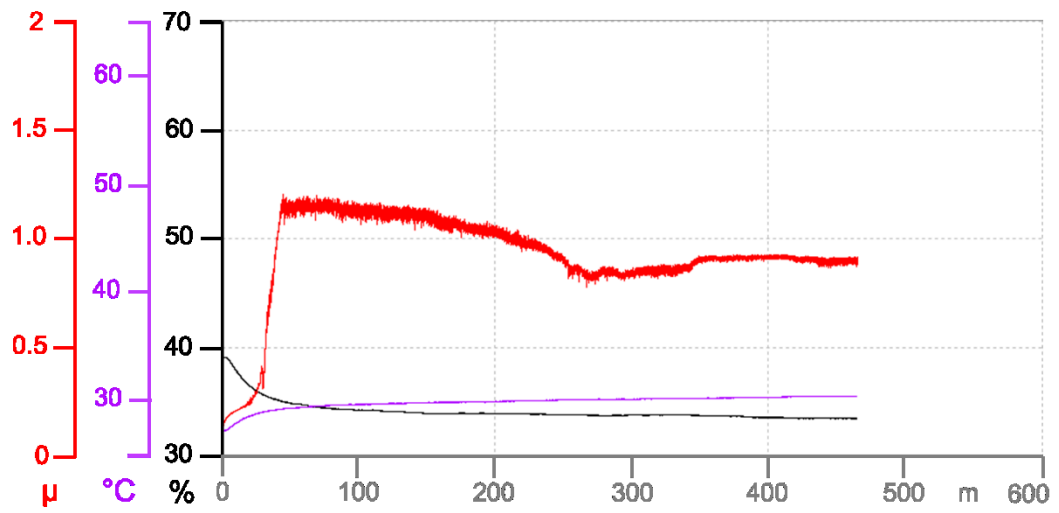
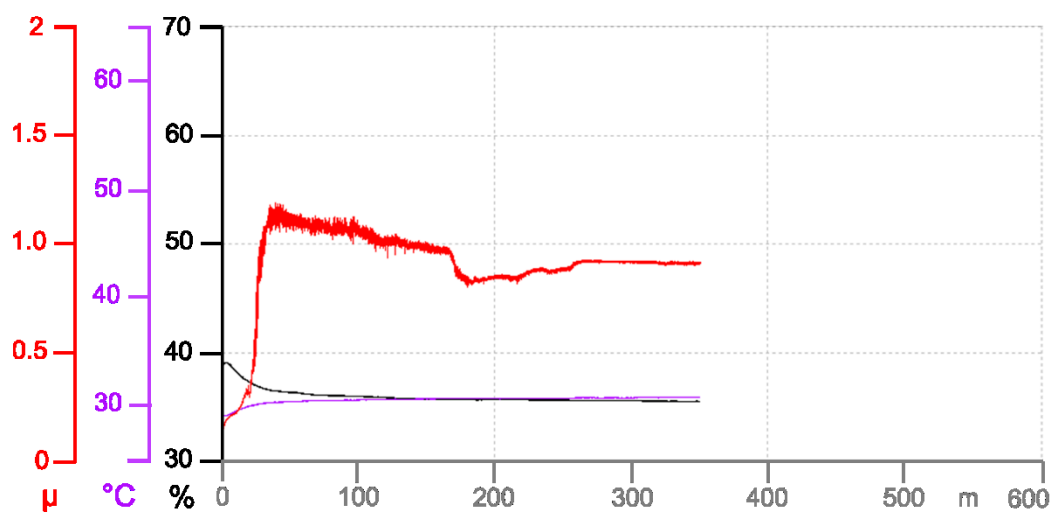
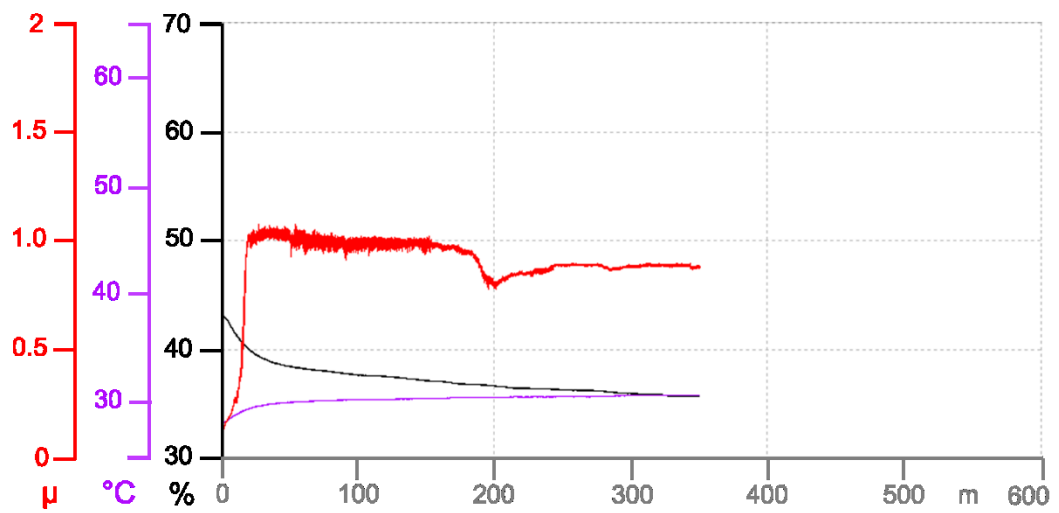
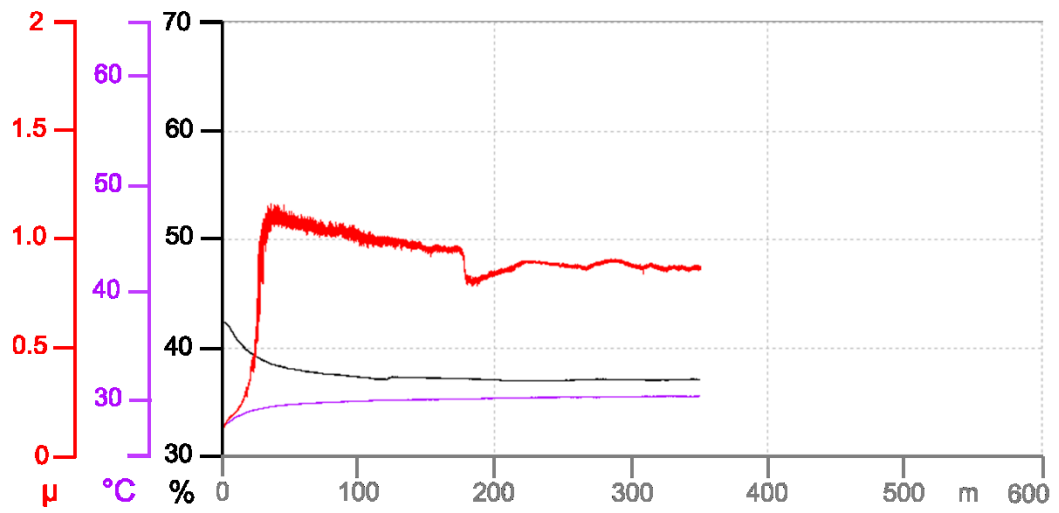


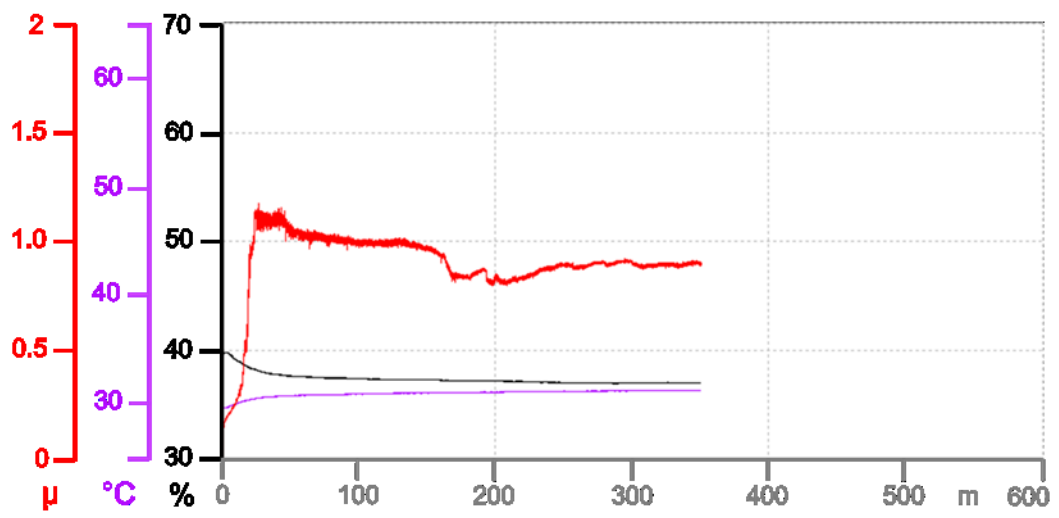
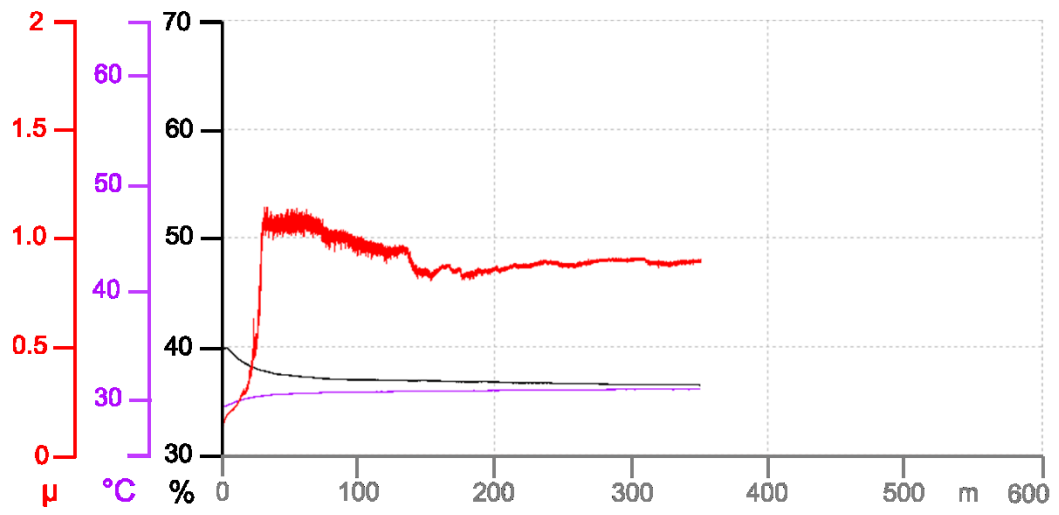
Figure 0.5 Test 1: filtered friction curve











13 BIBLIOGRAPHY

- [1] P. Blau, "Experimental Aspects of friction research on the macroscale," in *Fundamentals of Tribology and Bridging the Gap Between the Macro- and Micro/Nanoscale*, Springer-Science Dordrecht, 2000, pp. 261-278.
- [2] J. Blau, *Friction Science and Technology, from concepts to applications*, CRC Press, 2008.
- [3] *DIN 50322:1986-03, Wear: specification of the categories of the wear testing*, Deutsches Institut für Normung.
- [4] K. Holmberg and A. Matthews, *Coatings Tribology*, Amsterdam: Elsevier Science, 1994.
- [5] G. Stachowiak and A. Batchelor, *Experimental methods in tribology*, Elsevier Science, 2004.
- [6] J. Blau, "The use and misuse of the pin-on-disk wear test," in *STLE Annual Meeting*, Lake Buena Vista, 2014.
- [7] A. G99-05, *Standard Test Method for Wear Testing with a Pin-on-Disk Apparatus*, West Conshohocken, PA: ASTM International, 2005.
- [8] *ISO 18535:2016, Diamond-like carbon films - Determination of friction and wear characteristics of DLC films by ball-on-disc method*, ISO International.
- [9] (Ed.) and B. Bushan, *Modern tribology Handbook*, CRC Press, 2001.
- [10] D. Pirro and A. Wessol, *Lubrication fundamentals*, New York: Marcel Dekker, 2001.
- [11] Z. Pawlak, *Tribochemistry of lubricating oils*, Amsterdam: Elsevier, 2003.
- [12] B. Hamrock, S. Schmid and B. Jacobson, *Fundamental of Fluid film lubrication*, New York: Marcel Dekker, 2004.
- [13] G. Stachowiak and A. Batchelor, *Engineering Tribology*, Butterworth-Heinemann, 2013.
- [14] W. Johnston, "A Method to Calculate the Pressure-Viscosity Coefficient from Bulk Properties of Lubricants," *ASLE Transactions*, vol. 24, no. 2, pp. 232-238, 1981.
- [15] P. Huang and S. Wen, "Non-Newtonian effects of temperature and lubrication failure mechanism analysis," *Lubrication and Sealing*, vol. 2, pp. 14-16, 1996.
- [16] D. Dowson, D. Hopkins and G. Higginson, *Elasto-hydrodynamic lubrication*, Oxford: Pergamon Press, 1977.
- [17] O. Reynolds, "On the theory of lubrication and its application to Mr. Beauchamps tower's experiments, including an experimental determination of the viscosity of olive oil," *Philosophical Transactions of the Royal Society of London*, vol. 177, pp. 157-223, 1886.
- [18] S. Wen and P. Huang, *Principles of Tribology*, John Wiley & Sons, 2012.
- [19] A. C. Redlich, D. Bartel, H. Schorr and L. Deters, "A Deterministic EHL Model for Point Contacts in Mixed Lubrication Regime," in *Thinning Films and Tribological Interfaces*, Amsterdam, Elsevier Science, 2000, pp. 85-93.

- [20] R. Bayer, *Mechanical Wear fundamentals and testing*, New York: Marcel Dekker, 2004.
- [21] H. Czichos, *Tribology*, Elsevier Scientific, 1978.
- [22] B. Hamrock and D. Dowson, "Isothermal Elastohydrodynamic lubrication of point contacts - Part 1," *ASLE Journal of Lubrication Technology*, pp. 223-228, 1976.
- [23] S. Timoshenko and J. Goodier, *Theory of Elasticity*, New York: McGraw Hill, 1951.
- [24] A. Grubin and I. Venogradova, *Investigation of the Contact of Machine Components*, vol. 30, Central Scientific Research Institute for Technology and Mechanical Engineering (TsNIITMASH, 1949.
- [25] J. Archard and E. Cowking, "lastohydrodynamic Lubrication of Point Contacts," *Proceedings Instrument Mechanical Engineers*, vol. 180, pp. 47-56, 1965.
- [26] R. Chittenden, D. Dowson, J. Dunn and C. Taylor, "A theoretical analysis of the isothermal elastohydrodynamic lubrication of the concentrated contacts- Part I and II," *Proceedings of the Royal Society of London*, vol. 396, pp. 245-269, 1985.
- [27] Y. Chiu and J. Sibley, "Contact shape and non-Newtonian effects in elastohydrodynamic point contacts," *Lubrication Engineering*, vol. 28, pp. 48-60, 1972.
- [28] M. Kaneta, "For the establishment of a new EHL theory," in *Tribology Series*, vol. 36, Elsevier, 1999, pp. 25-36.
- [29] P. Yang and M. Kaneta, "Effects of thermal conductivity of contacting surfaces on point EHL contacts," *Journal of tribology*, vol. 125, pp. 731-739, 2003.
- [30] F. Guo and P. Wong, "Experimental observation of a dimple-wedge elastohydrodynamic lubricating film," *Tribology International*, vol. 37, pp. 119-127, 2004.
- [31] P. Yang, S. Qu, M. Kaneta and H. Nishikawa, "Formation of steady dimples in point TEHL contacts," *ASME Journal of Tribology*, vol. 123, pp. 42-49, 2001.
- [32] Z. Fu, P. Wong and F. Guo, "Effect of Interfacial Properties on EHL Under Pure Sliding Conditions," *Tribology Letters*, vol. 49, pp. 31-38, 2013.
- [33] P. Ehret, D. Dowson and C. Taylor, "On lubricant transport conditions in elastohydrodynamic conjunctions," *Proceedings of the Royal Society of London*, vol. 454, pp. 763-768, 1998.
- [34] M. Carli, K. Sharif, E. Ciulli, H. Evans and R. Snidle, "Thermal point contact EHL analysis of rolling/sliding contacts with experimental comparison showing anomalous film shapes," *Tribology International*, vol. 42, pp. 517-525, 2009.
- [35] P. Cann, E. Ioannides, B. Jacobsen and A. Lubrecht, "The lambda ratio – a critical re-examination," *Wear*, no. 175, pp. 177-188, 1994.
- [36] T. Conry and S. W. a. C. Cusano, "A Reynolds-Eyring Equation for Elastohydrodynamic Lubrication in Line Contacts," *ASME Journal of Tribology*, vol. 109, no. 4, pp. 648-658, 1993.
- [37] S. Günsel, S. Korcek, M. Smeeth and H. Spikes, "The Elastohydrodynamic Friction and Film Forming Properties of Lubricant Base Oils," *Tribology Transactions*, vol. 42, pp. 559-569, 1999.
- [38] P. Cann, E. Ioannides, B. Jacobsen and A. Lubrecht, "The lambda ratio – a critical re-

- examination,” *Wear*, vol. 175, pp. 177-188, 1994.
- [39] R. Kunz, “Thermal and traction behaviour in sliding elasto-hydrodynamic contacts,” Thesis work - Georgia Institute of Technology, Atlanta, 1964.
- [40] W. Wilson and S. Sheu, “Effect of Inlet Shear Heating Due to Sliding on Elasto-hydrodynamic Film Thickness,” *ASME Journal of Lubrication Technology*, vol. 105, pp. 187-188, 1983.
- [41] B. Hamrock and D. Dowson, “Isothermal Elasto-hydrodynamic Lubrication of Point Contacts,” *ASME Journal of Lubrication Technology*, vol. 99, no. 2, pp. 264-276, 1977.
- [42] G. Stachowiak and A. Batchelor, *Engineering Tribology*, Butterworth-Heinemann, 2014.
- [43] J. Wheeler, P. Vergne, N. Fillot and D. Philippon, “On the relevance of analytical film thickness EHD equations for isothermal point contacts: Qualitative or quantitative predictions?,” *Friction*, no. 4, pp. 369-379, 2016.
- [44] A. Petrousevitch, D. Kodnir and R. Salukvadze, “The Investigation of Oil Film Thickness in Lubricated Ball-Race Rolling Contact,” *Wear*, vol. 19, pp. 369-389, 1972.
- [45] H. Nishikawa, K. Handa and M. Kaneta, “Behavior of EHL films in reciprocating motion,” *JSME International Journal*, vol. 38, pp. 558-567, 1995.
- [46] G. Straffelini, *Friction and wear*, Springer, 2014.
- [47] K. Zum Gahr, *Microstructure and wear of materials*, Dordrecht: Elsevier, 1987.
- [48] E. Rabinowicz, *Friction and wear of materials*, John Wiley & Sons, 1995.
- [49] B. Bushan, *Introduction to Tribology*, New York: John Wiley & Sons, 2013.
- [50] F. De Maio, *Analisi sperimentale del comportamento ad usura di materiali compositi a matrice polimerica*, Tesi di dottorato di ricerca: Università degli Studi di Napoli "Federico II", 2007.
- [51] R. Bunshah, *Handbook of hard coatings*, Elsevier, 2000.
- [52] E. Bottarelli. [Online]. Available: http://www.quadernodiepidemiologia.it/epi-mobile/cause/coef_cor.htm. [Accessed March 2019].
- [53] P. Cuppari. [Online]. Available: <https://www.cuppari.it/matematica/schede/interpolazione.pdf>. [Accessed March 2019].
- [54] P. Shukla, V. Kumar, M. Curtis, C. Sondergeld and R. C.S., “Nanoindentation Studies on Shales,” in *47th US Rock Mechanics / Geomechanics Symposium*, San Francisco, CA, USA, 2013.
- [55] X. Zhang, Z. Li and J. Wang, “Friction prediction of rolling-sliding contact in mixed EHL,” *Measurement*, vol. 100, pp. 262-269, 2017.
- [56] X. Zhang, S. Kanapathipillai, T. Wu and Z. Peng, “Friction behavior and friction mechanisms of rolling-sliding contact in mixed EHL,” *Tribology International*, vol. 114, pp. 201-207, 2017.
- [57] Z. Fu, P. Wong and F. Guo, “Effect of Interfacial Properties on EHL Under Pure Sliding Conditions,” *Tribology Letters*, vol. 49, pp. 31-38, 2013.

